6-26-2015

Low Temperature Growth and Characterization of ZnO Nanostructures

Matthew Erdman

Matthew Erdman

Candidate

Electrical Engineering

Department

This thesis is approved, and it is acceptable in quality and form for publication:

Approved by the Thesis Committee:

Olga Lavrova , Chairperson

Ganesh Balakrishnan

Ying-Bing Jiang

LOW TEMPERATURE GROWTH AND CHARACTERIZATION OF ZNO NANOSTRUCTURES

by

MATTHEW ERDMAN

B.S. ELECTRICAL ENGINEERING

THESIS

Submitted in Partial Fulfillment of the
Requirements for the Degree of

Masters of Science

Electrical Engineering

The University of New Mexico
Albuquerque, New Mexico

May, 2015

Dedication

This work is dedicated to my beautiful partner Jenna that helped pushed me though the hardest parts of my long journey up to this point. May this be the first step in the rest or our long and wonderful journey.

Acknowledgments

I gratefully acknowledge the wonderful help I received by Sandia National Laboratory's Center for Integrated Nano Technology scientists and staff for the advice and patience while I learned many of these complicated procedures and equipment. I would also like to thank my committee as each and every one of you have helped me in ways unimaginable at some point along my journey.

Low Temperature Growth and Characterization of ZnO Nanostructures

BY

MATTHEW ERDMAN

B.S., Electrical Engineering, University of New Mexico, 2013
M.S., Electrical Engineering, University of New Mexico, 2015

A large factor in the decision of using solar systems over readily available fossil fuels and other energy production methods is the upfront cost of solar systems. Therefore a potentially low cost energy harvesting device has been proposed in the form of a hybrid organic-inorganic thermoelectric solar cell. The proposed device uses two different inorganic materials as the top and bottom contacts, and an organic material between the two contacts as a light absorber. The two contacts proposed are Zinc Oxide (ZnO) nanowires and Bismuth Telluride (BiTe) nanowires, and the organic light absorber is a semiconductor porphyrin. To further develop and design this device, the two contact materials need to be characterized and further developed. This manuscript focuses on the growth and characterization of the ZnO nanowires as the top contact.

Interestingly, during the development and characterization of the ZnO nanowires, another nanostructure was unexpectedly grown and was also characterized. The second structure was determined to be a two dimensional ZnO nanoplatelet. It was observed the two structures share the same crystal structure and both can be grown at atmospheric pressure in a low energy growth process. The characterization methods used to characterize the two ZnO structures were electron microscopy including Scanning Electron Microscopy (SEM), Transmission Electron

Microscopy (TEM), Scanning Transmission Electron Microscopy (STEM), diffraction pattern analysis via TEM, Energy Dispersive X-Ray Spectroscopy (EDS) via TEM, X-Ray Diffraction Analysis (XRD), absorption spectral analysis, and I-V curves via Contact Atomic Force Microscopy (CAFM).

Table of Contents

List of figures ..... **ix**

CHAPTER1 ..... **1**

Chapter 2 ..... **9**

SEEDING LAYER **9**

AQUEOUS GROWTH **14**

CHARACTERIZATION METHODS **18**

ELECTRON MICROSCOPY 18

SCANNING ELECTRON MICROSCOPE 20

TRANSMISSION ELECTRON MICROSCOPY 23

DIFFRACTION PATTERN ANALYSIS 25

SCANNING TRANSMISSION ELECTRON MICROSCOPY 28

X-RAY DIFFRACTION 30

ABSORPTION SPECTRAL ANALYSIS (UV-VIS) 32

CONTACT ATOMIC FORCE MICROSCOPY 32

CHAPTER 3 ..... **35**

SEM NANOWIRES, NON-DOPED AND DOPED **35**

SEM NANOPLATELETS NON-DOPED AND DOPED **45**

TEM **51**

NANOPROBE EXPERIMENT **53**

DIFFRACTION PATTERN ANALYSIS **57**

STEM **60**

EDS with TEM **63**

XRD **64**

UV-VIS **67**

CAFM **71**

Conclusion **83**

REFERENCES **84**

List of figures

Figure 1: Image and energy diagram of conceptual thermoelectric solar cell 2

Figure 2. The SEM images A and B above show high resolution image of the PVD grown AlZnO thin film 6

Figure 3. Image of nanoplatelets grown via the pseudo vapor growth approach 7

Figure 4: Sol-Gel images showing the non uniform growth of nanowires 10

Figure 5. This image of the seeding layer shows the small size of the seeds 13

Figure 6: These diagrams illustrate the submerged growth method and the pseudo vapor growth procedure. 17

Figure 7: In the above images, it can be seen how the diffracted beams can be used to create a diffraction patter. 26

Figure 8: The above image demonstrates the use of an objective aperture to specifically pick a diffraction point that will result in imaging of only that crystal plane. 27

Figure 9: Comparison of light field image to dark field image. 28

Figure 10: STEM image showing the contrast between the dark non-organic nanowire covered with an organic porphyrin. 30

Figure 11: Diagram of Bragg condition taken from the Britannica website 31

Figure 12: It can be seen that the spin coated samples are very rough and inconsistent 36

Figure 13: SEM image of thin film. 37

Figure 14. Side profile of the non-doped nanowires can be seen at different temperatures. 39

Figure 15: The aspect ratio of the nondoped nanowires can be approximated as a linear increase as the temperature of the growth is increased. 40
Figure 16: The data shows an increase in the diameter of the nanowires. 41
Figure 17: The increase of the length of the nondoped nanowires was approximated as being a linear increase of length to increase of temperature. 42
Figure 18. Side profiles of the doped nanowires grown at different temperatures. 43
Figure 19: The increase in doped nanowire length versus temperature was inconclusive. 44
Figure 20: Doped nanowire diameter versus temperature. 44
Figure 21: Aspect ratio of doped nanowires versus temperature. 45
Figure 22. SEM image of the nanoplatelets grown via the pseudo vapor deposition 46
Figure 23. The nanoplatelete growth time did not have as much of an affect on the growth characteristics as it did for the nanowires. 47
Figure 24: The images show a one to one ratio growth of aqueous Zn Nitrate to HMA at a very low molar concentration of 0.0005M. 48
Figure 25: The images show a one to one ratio growth of aqueous Zn Nitrate to HMA at a very low molar concentration of 0.0005M. 49
Figure 26: The images show a one to one ratio growth of aqueous Zn Nitrate to HMA at a very low molar concentration of 0.0005M. 49
Figure 27: The images show a one to one ratio growth of aqueous Zn Nitrate to HMA at a very low molar concentration of 0.0005M. 50

Figure 28. SEM of non-doped nanoplatelets and doped nanoplatelets. 51

Figure 29. TEM images of nanowires and nanoplatelets with A and B being images of nanowires and C and D being images of nanoplatelets. 53

Figure 30: Images of nanoprobe TEM experiment. 55

Figure 31: Images of increasing voltages during the nanoprobe experiment. 56

Figure 32. TEM images of the nanowires and nanoplatelets with corresponding diffraction patterns from those samples. 58

Figure 33: Analysis of gathered diffraction patterns of the ZnO nanostructures. 59

Figure 34: Analysis of gathered diffraction pattern of the ZnO nanoplatelets. 60

Figure 35. STEM images of porphyrin coated nanowires. 62

Figure 36: EDS of doped ZnO nanowire and corresponding TEM image. 63

Figure 37: EDS of porphyrin coated BiTe nanowire. 64

Figure 38: The above XRD data in order from top to bottom is from the grown Al doped ZnO thin film, ZnO nanowire, and ZnO nanoplatelets 65

Figure 39: Acquired XRD from known ZnO nanostructures. 66

Figure 40: Corrected transmissivity of non-doped ZnO nanowires. 69

Figure 41: Corrected transmissivity of doped ZnO nanowires. 69

Figure 42: Transmissivity vs aspect ratio plot to show of nondoped nanowires. 70

Figure 43: Transmissivity vs aspect ratio plot to show of nondoped nanowires. 71

Image 44: Conductivity data collected for nondoped ZnO nanowire grown within solution at 50°C. 73

Figure 45: Conductivity data collected for nondoped ZnO nanowire grown within solution at 60°C. 73

Figure 46: Conductivity data collected for nondoped ZnO nanowire grown within solution at 70°C. 74
Figure 47: Conductivity data collected for nondoped ZnO nanowire grown within solution at 75°C. 74
Figure 48: Conductivity data collected for nondoped ZnO nanowire grown within solution at 80°C. 75
Figure 49: Conductivity data collected for doped ZnO nanowire grown within solution at 60°C. 75
Figure 50: Conductivity data collected for doped ZnO nanowire grown within solution at 70°C. 76
Figure 51: Conductivity data collected for doped ZnO nanowire grown within solution at 75°C. 76
Figure 52: Conductivity data collected for doped ZnO nanowire grown within solution at 80°C. 77
Figure 53: Curve fit of Ideal Diode equation for nondoped nanowires grown 60° C. 77
Figure 54: Curve fit of Ideal Diode equation for doped nanowires grown at 70° C. 78
Figure 55: Conductivity data collected for nondoped ZnO nanoplatelet grown in the pseudo vapor. 79
Figure 56: Conductivity data for curve one collected for doped ZnO nanoplatelet grown via the pseudo vapor method. 80

Figure 57: Conductivity data for curve two collected for doped ZnO nanoplatelet grown via the pseudo vapor method. 80

Figure 58: Nondoped nanoplatelet CAFM image collected during the collection of the conductivity data. 81

Figure 59: Doped nanoplatelet CAFM image collected during the collection of the conductivity data. 82

CHAPTER1

Since the discovery of the photoelectric affect, solar power has been seen as a potential solution to humans ever increasing energy usage. One of the limiting factors of photovoltaic devices are their higher upfront costs when compared to standard energy producing technologies. When solar technologies introduce nano sized materials, the added benefit and potentially lower costs are very promising. By using a radial junction in the form of a core shell structure, where a semiconductor nanowire is surround by a light sensitive, conductive organic porphyrin, light absorption can be physically separated from the charge carrier collection for added benefit. Nanostructured materials can therefore induce light trapping in the nanowire ensemble, hence improving absorption with respect to conventional planar layers. Furthermore, charge carrier collection can be more efficient owing to the much smaller collection distance and to the better crystalline quality of nanowires presenting a lower density of defects.

By combining two different energy harvesting techniques, a potential to increase the efficiency of a solar device can be increased and is the idea behind a hybrid thermoelectric solar device. Such a device can allow for light energy to be absorbed via a photosensitive material, and heat energy absorption via two different conductive materials interacting with each other via thermoelectric properties. By combining these two ideas physically, a device has the potential to increase the overall efficiency of a device that only acts on one property alone [1, 2, 3, 4, 5, 6]. As seen in Figure 1, a device that has a photoconductive organic material

between two different types of non-organic conductive nanowires has the potential to combine the photoconductive properties of the organic material, and the thermo-electronic properties of the two different non-organic materials interact with one another in a hot anode, cold anode fashion. The materials being used in this proposed set up are a conductive Zinc-Tin porphyrin CBI structure as the photoconductive organic material, and Zinc Oxide (ZnO) and Bismuth Telluride (BiTe) nanowires as the hot anode and cold anode respectively [1, 2, 3].

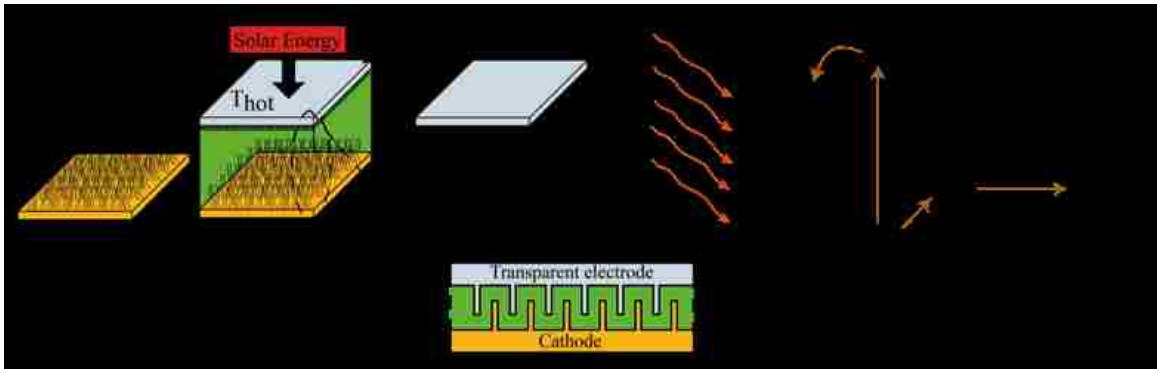

Figure 1: Image and energy diagram of conceptual thermoelectric solar cell. Shown in A of Figure 1 is the purposed physical design of the hybrid thermoelectric solar device. The image shows ZnO nanowires as being used as the top contact. The energy diagram shows the organic CBI structure acting as the active region of the device and the ZnO nanowires acting as the electron collector and the bottom contact as the hole collector. This diagram does not note that the hole collector is a layer of BiTe nanowires. In the figure 1, B represents the energy diagram of the system and the ideal paths of the electron and hole pairs [2, 3].

This manuscript will focus on the development and characterization of the ZnO nanowires, therefore no further discussion of the organic CBI structure will be taken. For further information on the organic CBI material, see the following references, [1, 5, 7, 8, 9, 10]. Also, a note must be taken that during the development of the ZnO nanowires, a second nanostructure was found in the form of a two dimensional nanoplatelet. Further details on the nanoplatelets will be discussed in

Chapter 2.

Zinc Oxide (ZnO) is a wide bandgap semiconductor typically found with a range of bandgaps between 3.3eV-3.4eV and is intrinsically n-type [10, 11]. ZnO typically has a stable Wurtzite, or hexagonal, crystal structure, but can be grown to have a cubic structure as well. The cubic crystal growth is much less favorable and is a higher energy growth when compared to the Wurtzite growth [10, 11, 12, 13, 14, 15]. This is why the most common nanocrystal growth for ZnO is the Wurtzite crystal structure. ZnO has attracted intensive research due to its favorable properties, low growth cost, and versatile applications in transparent electronics, ultraviolet (UV) and blue light emitters, piezoelectric devices, chemical and gas sensors, and spin electronics [16, 17, 18, 19, 20, 21]. It has also been shown that invisible thin film transistors (TFTs) using ZnO as an active channel have achieved higher field effect mobility than comparable amorphous Silicon TFTs [22, 23, 24]. The favorable physical properties of ZnO and desire to make devices smaller has played a large effect to focus on synthesizing, characterizing, and device development using ZnO nanostructures.

The crystal morphology and optoelectronic characteristics of ZnO nanostructures are very dependent upon the fabrication method which have widely variable temperatures and pressures ranging from under boiling temperatures at atmospheric pressure to over 675°C at pressures of an ultra high vacuum [11, 14, 15, 24]. Out of the different nanostructures that can be made using ZnO, two of the most widely studied ZnO nanostructures are wurtzite ZnO nanowires, nanobelts, and other nanostructures. Nanowires are characterized as having one dimension, or

growth restricted to primarily in the C crystal surface direction; while nanobelts are characterized as having two dimensions of restricted growth with one of those restrictions as a weak restriction. The result of the nanobelt restrictions is a two dimensional structure.

ZnO nanowires, or nanorods, can be grown with a variety of techniques with ranging diameters from under 50 nanometers (nm) to over 200 nm with lengths that can exceed 10 micrometers (μm) [14, 26, 30]. Very common growth techniques used in research and industry are to epitaxially grow ZnO nanostructures using metal-organic chemical vapor deposition (MOCVD), pulsed laser deposition (PLD), and vapor-liquid-solid (VLS) [14, 26, 30]. These techniques allow for very controlled doping and growth of ZnO nanostructures by maintaining a very controlled and stable environment of high vacuum and high temperatures exceeding 650°C. Even though these techniques allow for highly controlled growth conditions, in order to make ZnO nanostructures a more viable option for electronic and optoelectronic devices a less energy intensive growth process should be used.

An aqueous chemical growth processes can be used to grow highly crystalline doped and non-doped ZnO nanostructures. The non-doped method consists of an aqueous solution of equal molar concentrations of Zinc Nitrate Hexahydrate (will be referred as Zn Nitrate here on) and Hexamethylenetetramine (HMA). Typically the temperature of the aqueous solution is raised to above 70° C, with most techniques raising the temperature to 90° C at time frames of one to several hours [15, 27, 29, 26, 28, 31]. To dope the grown nanostructures, different dopants have been used including Aluminum Nitrate Nonahydrate (will be referred as Al Nitrate here on) at

percentages of 1%-3% [32, 33]. The following study of ZnO nanostructures Al Nitrate was used as the dopant due to its simplicity to incorporate into the developed ZnO nanowire growth processes used.

The growth method and post processing of ZnO nanostructures has a great impact on its optoelectronic characteristics. Depending on growth conditions and post processing, the oxygen vacancies on the surface of ZnO and other metal-oxides such as SnO and TiO2 can greatly affect the conductivity and transparency of the grown metal-oxide nanostructures. Surface absorption and vacancies of O2 can significantly affect the conductivity of the material. This not only can affect the conductivity of the structures through regular photogeneration, but this can allow for ZnO structures be used as gas sensors. This is due to how the oxygen on the surface reacts to the environment, either creating excess vacancies or filling vacancies [34, 35].

Although ZnO nanowires grow relatively easily in a wurtzite structure, their alignment during growth is not trivial in an aqueous growth processes. The use of a seeding layer is crucial for obtaining ordered and aligned arrays of nanowires with vertical orientation in the C crystal plane. Grain size, uniformity, compactness, and degree of crystallographic orientation of the seeding layer are fundamental for the nanowires morphology and orientation relative to the substrate. The first seeding layer used, was a Sol-Gel spin coat applied layer synthesized using a solution of Zinc Acetate and Ethanolamine [15]. This approach is the most cost effective approach for growth of ZnO nanowires, but the process itself needed time to be perfected. It was decided early on that it would be most beneficial to use a more controlled

seeding to develop a highly uniform layer of ZnO nanowires for testing purposes. This seeding layer to be used to create a highly uniform layer of nanowires was decided to be a 2% Aluminum doped ZnO thin film (ZnO/Al2O3). This thin film was grown via Physical Vapor Deposition (PVD) using a Kurt J. Lesker PVD75 machine. This deposition technique for thin film growth created a uniform layer of Aluminum doped ZnO for the ZnO nanowires to grow on.

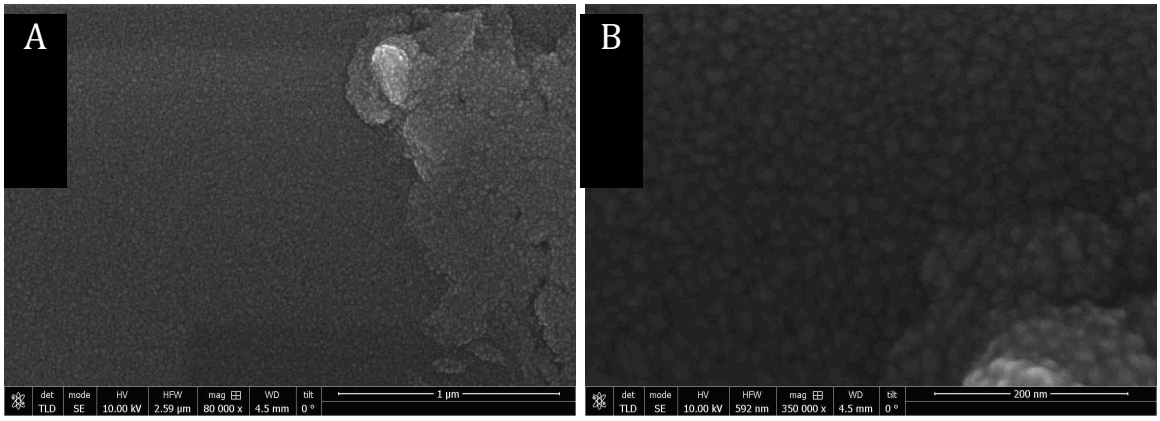

Figure 2. The SEM images A and B above show high resolution image of the PVD grown AlZnO thin film. The large imperfections seen in the image are not common and were included in the image only to help in focusing purposes.

While studying the growth of the ZnO nanowires in an aqueous solution, different growth procedures were attempted in the assumption that different methods had a higher probability to reduce or eliminate the defects due to contaminations within the solution therefore creating a higher uniformity in the nanowire crystal. A pseudo vapor growth was attempted by suspending the growth substrate above the heated aqueous solution so that vapor would condense on the substrate instead of fully submerging the substrate in the aqueous solution. The outcome of this experiment did not limit the contaminants while the nanostructures grew, but synthesized a different crystallization of the ZnO. What was determined to be nanoplatelets that were grown, which are ZnO nanostructures that have two

dimensions similar to nanobelts. It was later discovered that these structures grew because of the limited reactants in the vapor solution and the lower temperature of the substrate. This was confirmed by a growth experiment that showed the nanoplatelets also grow within the solution if the reactant concentration and the aqueous solution temperature are lowered enough.

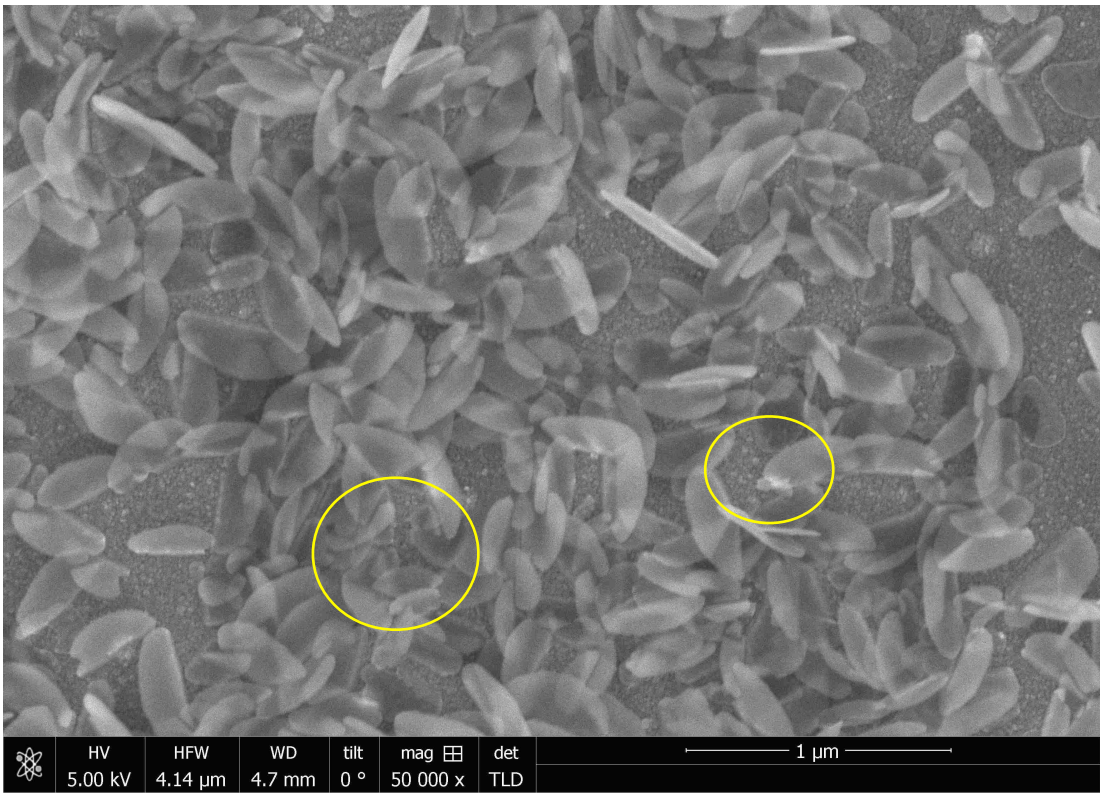

Figure 3. Image of nanoplatelets grown via the pseudo vapor growth approach. The yellow circles indicate areas were one or more nanoplatelets have interwoven.

The characterization methods used on the nanowires and nanoplatelets were Scanning Electron Microscopy (SEM), Transmission Electron Microscopy (TEM), Scanning Transmission Electron Microscopy (STEM), diffraction pattern analysis via TEM, Energy Dispersive X-Ray Spectroscopy (EDS) analysis via TEM and SEM, X-Ray Diffraction (XRD), absorption spectral analysis, and Contact Atomic Force Microscopy (CAFM). All of the characterization methods were used in specific ways

to characterize the nanowires and the nanoplatelets. Regular TEM imaging, STEM imaging, and SEM imaging were used for basic analysis to confirm the growth of the nanowires and nanoplatelets. These imaging techniques were crucial because regular AFM imaging is limited, especially when imaging the nanoplatelets. Also using STEM imaging, an image with a large contrast between organic and inorganic material can be taken allowing for high quality images of porphyrin coated nanowires. EDS allowed for confirmation of composition of the nanowires and nanoplatelets, while diffraction pattern analysis via TEM and XRD were used to confirm crystallinity of the two nanostructures. Absorption spectral analysis allowed for a study of the percentage of transmissivity of the nanowires based on the temperature of growth and doping. Lastly the conductivity was measured for both doped and undoped nanowires and nanoplatelets using the CAFM

Chapter 2

A very simplistic approach was taken in developing a growth procedure for the ZnO nanowires, which allowed for some abstract experimentation leading to an unexpected nanostructure growth. The two growth procedures taken were, 1) to fully submerge a sample with a seeding layer within a heated aqueous solution, and 2) to suspend a sample with a seeding layer outside of a heated aqueous solution within the vapor produced by the heated solution. The latter growth procedure lead to an unexpected growth of a two dimensional ZnO crystal structure. This unexpected growth of a two dimensional structure, instead of the predicted one dimensional nanowire growth lead to further testing of the new two dimensional structure. When confirming the structure with literature, it was found to be termed a nanoplatelet [36, 37, 38, 39]. The structure was to confirm crystallinity and other pertinent characteristics of nanostructures being used for optoelectronic devices. As it will be shown through the data, these new two dimensional structures did have the same crystalline characteristics of the known one dimensional ZnO nanowires.

There are many characterization methods to fully characterize nanostructures, with certain ones being more relevant for specific technologies. It was decided that the three most relevant characterization methods were

SEEDING LAYER

The original seeding layer used to grow the ZnO nanowires was a conductive Sol-Gel spin coated film. First the glass substrates were cleaned by spraying the glass with isopropyl alcohol then dried and heated for 10 minutes at a temperature of no less than 200°C. This was the cleaning technique used for all glass substrates

used to grow a seeding layer on. The Sol-Gel spin coating solution was made by making a solution of 0.1g of Zinc Acetate, 0.5 mL of Ethanolamine, and 12.5 mL of deionized water [15]. This solution was mixed together for no less than 15 minutes to stabilize the Sol-Gel solution. The Sol-Gel was then used as the solution to spin coat the glass substrates. The spin coat method used was to place a drop of the solution on the glass substrate on the spin coater. The spin coater was then set to run at a speed of 2000 RPM for 30 seconds. The sample was then pre-baked for 20 minutes at 120°C. This process was repeated another two more times for a total of three layers spin coated on the sample. The spin coated sample was then annealed at 350°C for one hour [15]. This spin coated seeding layer was marginally successful, with its main fault being that it did not create a highly uniform layer for the nanowires to grow on. Only about three growths were conducted using this seeding layer, and the only characterization performed on these samples was SEM imaging.

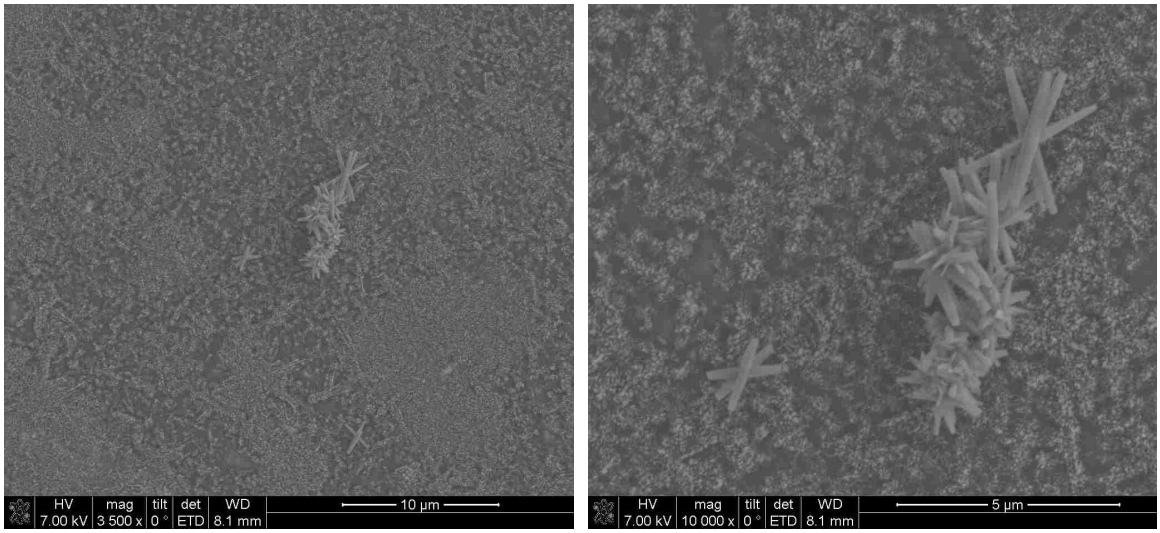

Figure 4: Sol-Gel images showing the non uniform growth of nanowires. As can be seen in the images, the nanowires did not grow at a highly uniform mater.

The intent in using the spin coated seeding layer was to implement a very cost effective seeding layer for the nanowires. As stated with the minimal tests

performed with the spin coated seeding layer, this procedure was quickly abandoned for a more uniform thin film seeding layer. The original objective in using a more uniform seeding layer was to develop a highly repeatable growth and doping procedure for the nanowires and to return to the spin coating seeding layer once the nanowire growth was developed. Once the secondary nanoplatelet structure was observed additional time was spent on characterizing of the nanoplatelets, therefore no other testing was performed on optimizing the spin coating seeding layer and is left for future development.

As stated previously, a uniform thin film replaced the spin coated seeding layer quickly during the testing of the nanostructure growth. This thin film was an Aluminum doped Zinc Oxide thin film. The doping concentration of the thin film was 3% atomic concentration Aluminum to Zinc. The thin film was applied using Physical Vapor Depositon (PVD) to sputter the thin film onto a glass slide. The machine used for this was a Kurt J. Lesker PVD 75 (Lesker 75). The method of sputtering films onto samples is a very common and versatile method used in electronics manufacturing [40, 41, 42, 43, 44, 45]. Even though sputtering is a fairly crude method to deposit materials on a sample, it is very effective.

The basic mechanics that allow for deposition of materials in a sputtering system are a physical bombardment of ions onto a target, essentially hitting loose atoms off the target to be deposited onto another surface. The chamber of the PVD is brought down to a high quality vacuum (6 mTorr), then Argon gas is introduced into the chamber. The target material to be deposited is heated to become more malleable and its holder is biased with a negative voltage. The stage holding the

samples is then biased at a positive bias, and since the chamber is at a high quality vacuum, the Argon gas ionizes into Ar+ at the sample holder [45]. Argon is used because even though it is ionized, it is still a very inert gas and will not react with the target, only bombard it. Some PVD recipes call for a certain percentage of oxygen to flow into the chamber to bombard the sample, but this was not the case for the thin film recipe used here. Since the depositing material holder is biased at a negative voltage, the positively charged Argon ions become attracted to the target holder and physically bombard the target material. This physical bombardment dislocates the target material allowing for it to float within the chamber and deposit on all of the surfaces in the chamber. This act of having loose AlZnO material freely floating within the chamber will essentially allow for the deposition of AlZnO over all the surface of the chamber. Even with the fact of effectively coating the entire chamber with the target material, this is a very effective and controlled method of depositing thin films [45].

The recipe used for the typical thin film growth was first to bring the chamber to a vacuum of 6 mTorr. The target is then slowly heated using a total power of 150 watts. Argon is introduced into the chamber forming plasma due to ionization of the Argon. The ionized Argon then starts to physical bombardment of the target material due to the negative bias of the deposition target. This is maintained for 10 minutes and results in an average thin film growth of 45 nanometers [45].

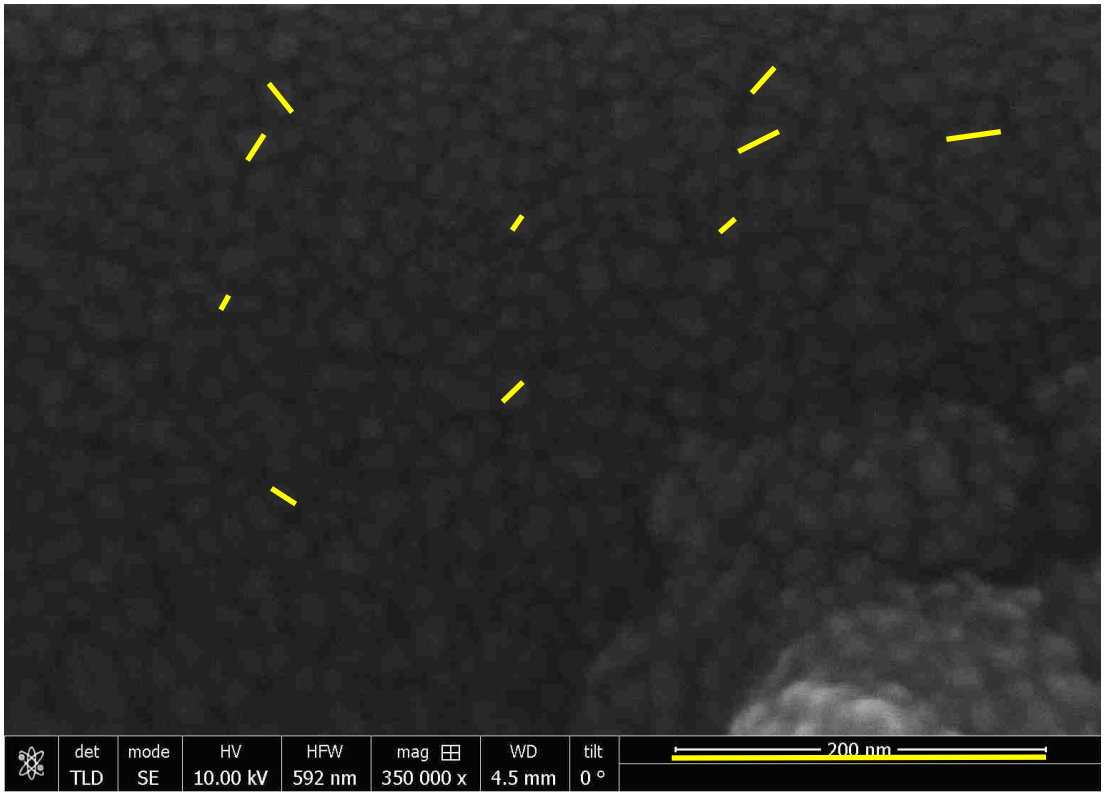

Figure 5. This image of the seeding layer shows the small size of the seeds 11nm, 15nm, 15nm, 9nm, 16nm, 24nm, 28nm, 18nm, and 19nm therefore the average diameter of 17nm.

As seen in Figure 5, the thin film appears to be slightly bumpy. PVD thin films are not the ideal way to deposit films, and this slightly rough surface will always be present, but vary between materials. Even though the surface looks imperfect, this rougher surface is what in fact makes it such a good substrate for the nanowire growth. These slight imperfections in the film are seeds for the nanowires. The average size of the seeds are approximately 17nm, which approaches the average diameter of the nanowires confirming the favorable growth conditions for the nanowires. Other films were used such as Gold and layered Gold Tellurium grown using electron beam deposition. These other films had no significant outcomes due to no favorable seeds being formed on the films' surfaces therefore will not be further discussed.

AQUEOUS GROWTH

A low energy, aqueous based growth was used to grow the Zinc Oxide nanowires and later the Zinc Oxide nanoplatelets. The growth consisted of a substrate with a seeding layer immersed in an aqueous solution with a one-to-one molar ratio of Zinc Nitrate Hexahydrate (referred to as Zn Nitrate here on) Zn(NO3)2 and Hexamethylenetetramine (HMA) C6H12N4 [15, 27, 29 26, 28, 31] The one-to-one molar ratio of Zn Nitrate and HMA was always kept during growth, but the molar value of the solution was changed during testing from 0.01M down to 0.005M. For instance the typical growth solution for the nanowire growth was a 0.01M:0.01M solution of Zn Nitrate to HMA. Therefore using these molar values and a total of 200mL of deionized water, the total measured amount of Zn Nitrate used for each growth was 0.59498g and the total measure amount of HMA used was 0.28038g with a +-5% error in measurement. The chemical reaction to form the ZnO nanostructures follows [27]

$$HMA + 6H_2O \leftrightarrow 4NH_3 + 6HCHO \quad (1)$$

$$NH_3 + H_2O \leftrightarrow NH_4^+ + OH^- \quad (2)$$

$$Zn^{2+} + 4NH_3 \leftrightarrow Zn[Zn(NH_3)_4]^{2+} \quad (3)$$

$$Zn^{2+} + 2OH^- \leftrightarrow Zn(OH)_2 \quad (4)$$

$$Zn(OH)_2 \leftrightarrow ZnO + H_2O \quad (5)$$

From these chemical equations it is easy to see that the Zn Nitrate Hexahydrate provides the Zinc to the solution in the form of Zn^{2+} with OH^- (Hydroxide) providing the Oxygen molecules to form the ZnO crystals. It has been suggested that

the HMA disassociates into Hydroxide by means of disassociating into NH_3 (Ammonia) allowing for the reduction reaction of NH_4^+ (Ammonium) and OH- (Hydroxide) to form. The reaction of the Zn^{2+} ions with the OH^- then forms the ZnO structure leaving a by product of $Zn[Zn(NH_3)_4]^{2+}$ [27, 29]. It should be noted that the formation of NH_3 and NH_4^+ is a natural reaction in water ecosystems due to decomposing organisms and is typically called Total Ammonia Nitrogen (TAN). With these considerations, there are three byproducts in the reaction : formaldehyde, Ammonia, and Ammonium [46].

For all growth processes, the Zn Nitrate and HMA were measured out separately in clean glass beakers. Half of the total deionized water to be used for the specific molar concentration was poured into each beaker, then the Zn Nitrate and HMA were added to the two different beakers and the individual solutions were stirred until the chemicals were fully dissolved in the solution, typically 10 minutes for each solution. Once each of the solutions were formed, they were poured into a single beaker, covered with parafilm to reduce loss of liquid via evaporation, and heated to the desired temperature. Depending on the procedure, the sample was then either submerged into the aqueous solution or suspended within the condensing vapor formed in the beaker due to the heat of the solution for the entire amount of growth time. Therefore the samples were not added to the solution until it was at the specified temperature and the solution was kept at a constant temperature during the entire growth process using a hot plate with a temperature probe.

The initial growth procedure was a fully submerged technique in which the

substrate with a deposited seeding layer was submerged fully in the solution for a variety of times from one hour to four hours and a variety of temperatures from 50°C to 90°C. It will be seen in the results chapter that a time of two hours submerged was determined optimal. It was also determined that the optimal temperature ranges from 60°C to 75°C depending on the metric used to determine optimal growth, either nanowire length or transparency. After the growth, the sample was taken out of the aqueous solution and thoroughly rinsed with deionized water. The sample was then fully dried with pressurized nitrogen gas. A second method was developed in which the sample was placed above the aqueous solution within the vapor formed due to the evaporation and condensation of the liquid. Unlike the submerged method, it was determined that the sample should allow for crystal growth for a longer timeframe of at least 16 and up to 48 hours. The optimal time determined for this method was 16.5 to 18 hours. This pseudo-vapor growth method was initially tested to determine if this technique would restrict the contaminants that could be present in the solution. Instead of restricting contaminants, the lowered temperature and concentration of the Zn Nitrate and HMA reactants during the growth produced a second crystalline structure, a nanoplatelet, which is a two dimensional nanostructure versus the one dimensional nanowire. It was shown that the lowered temperature and molarity of the reactants had a major role in the structure that grew during the growth. This was shown by growing the nanoplatelet structures within the aqueous solution at a lower molarity concentration and temperature than what was required for nanowire growth. A set of experiments was done that lowered the Zn Nitrate and HMA molarities down to

0.0005M and lowering the temperatures down at 5°C steps from 70° C down to 60°C.

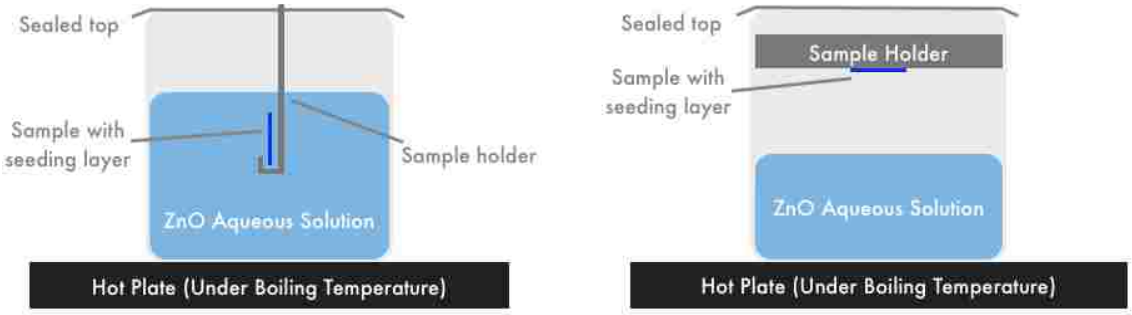

Figure 6: These diagrams illustrate the submerged growth method and the pseudo vapor growth procedure.

Since the final product desired was a transparent conductive oxide, the nanowire and nanoplatelet had a dopant introduced once the growth procedure was determined. The dopant for the nanowires, and later the nanoplatelets was Aluminum Nitrate Nonahydrate (referred to as Al Nitrate here on) Al(NO3)3. This dopant was chosen since it was easily applied to the developed growth procedures for the nanowires and nanoplatelets [32, 33]. It is suggested that the Al Nitrate reacts the same way the Zn Nitrate in the aqueous solution, therefore the Al will dissociate into the solution into Aluminum ions and Ammonia in the same fashion as Zn Nitrate [32, 33]. See reaction equation 3 [27]. Therefore by adding Al Nitrate to the solution, the reactions will allow for the formation of doped material since the Aluminum will be added to the chemical structure of the ZnO nanostructures [27, 32, 33]. It was determined that 3% Aluminum to Zinc would be an ideal doping to test, and therefore to create a solution of 300mL, 0.89247g of Zn Nitrate was prepped into a clean beaker, 0.42057g of HMA was prepped into another beaker, and lastly 0.02677g of Al Nitrate was prepped in a third clean beaker. The same as

before, the tolerances of measurement was +- 5% of the desired weight. In the same manner that the non-doped was prepped, 125mL of deionized water was added to the beakers with Zn Nitrate and HMA, and the remaining 50mL was added to beaker containing the Al Nitrate. All solutions were stirred until the reactant was fully dissolved, then all three solutions were added into a single beaker. This was then heated to the desired temperature for testing with a piece of parafilm over the top of the beaker to minimize the loss of water or reactants. Once the temperature stabilized, the sample was added, the beaker was sealed with parafilm again and the experiment started [27, 32, 33].

CHARACTERIZATION METHODS

Numerous characterizations methods were used to characterize both the doped and non-doped nanowires and nanoplatelets. These characterization methods included Scanning Electron Microscopy (SEM), Transmission Electron Microscopy (TEM), Scanning Transmission Electron Microscopy (STEM), diffraction pattern analysis via TEM, Energy Dispersive X-Ray Spectroscopy (EDS) via TEM, X-Ray Diffraction Analysis (XRD), absorption spectral analysis, and Contact Atomic Force Microscopy (CAFM).

ELECTRON MICROSCOPY

The basic physical phenomenon that dictates how regular microscopes function, also dictate how electron microscopes function. The only difference of the electron microscopes is instead of using visible light for viewing, electron beams are used. It should be noted that since it is an electron beam being used to image the

sample, the sample needs to be put in a vacuum to be imaged. This is to minimize any interaction with the electron beam with possible particles that would be in the air if not at vacuum. If there are any molecules floating within the electron microscope chamber, the electrons would interact with them and essentially cause noise within the system, making it much harder to image the sample.

In the same way that glass lenses bend optical light to magnify an image, magnetic lenses are used to bend electron beams to magnify anything being imaged by an electron microscope. As stated before, since electron microscopes are still microscopes, but they use electron beams as their light source, they are still limited by the Rayleigh Criterion. The Rayleigh Criterion states that a microscope's resolution is limited by the wavelength of the imaging light. The Rayleigh Criterion applied to an electron microscope states that the resolution of the microscope is,

$$R = \lambda/\mu \sin(\beta)$$

with lamda being the wavelength of the electrons leaving the electron source, μ is the refractive index of the viewing medium, and beta is the semi-angle of collection of the magnetic lens [47, 48]. Using the DeBroglie wavelength for an electron, the electrons wavelength can be written as,

$$\lambda = h/p$$

where h is Plank's constant and p is the momentum of the electron [47, 48]. Therefore using the source of electrons as an electrostatic potential drop, the electron wavelength is described as,

$$\lambda = h/\sqrt{2m_0 eU(1 + eU/2m_0 c^2)}$$

with m0 as the rest mass of the electron, eU is the potential of the electron source,

and c the speed light and the speed of an electron wave in a vacuum [47, 48]. As the equations dictating the resolution of the electron microscope state, the only variable that can change the wavelength of the electron beam is the electrostatic potential of the electron source since the rest of the variables are constants. Therefore the voltage of the electron source is what can change the resolution of the microscope, and with higher electron potential, the higher the resolution of the microscope. These equations can be applied to both Scanning Electron Microscopy (SEM), and Transmission Electron Microscopy (TEM), since both of the microscopes have electron sources that have variable electrostatic potentials. Even though the potential of the TEM is variable, it should be noted that it is typically kept at the same potential.

SCANNING ELECTRON MICROSCOPE

Scanning Electron Microscopy (SEM) is as it sounds, an electron microscope that scans the surface of a sample to construct a picture. Typical microscopes simply shine light through a sample, and the diffused light through the sample will give the user an image of the sample via contrast between different materials. Unlike regular microscopes, the SEM has to scan the electron beam source over the sample to create an image. By scanning the surface of the sample, the software can pin point the path the electron beam took using a detector that is between the beam path and the sample. This means that SEMs do not have a typical beam path that a regular microscope has [47, 48, 49].

Typical light microscopes have their light sources and image in a linear path. Therefore if the light path down the middle of all the lenses is drawn, it will be a

straight line from the light source to the detector, much like the human eye. This is of course for a simple microscope that most students used in high school chemistry and biology classes. SEMs on the other hand have a slightly different physical layout than regular light microscopes since the electrons used to image the samples are deflected at the surface of the sample due to the electrons having a large interaction with the atoms at the surface of the sample. Electrons are deflected back once they interact with the sample, therefore the images created by an SEM are created with primary and secondary backscattered electrons that are collected with an electron detector through different detectors. The SEM is able to calculate the energy of the backscattered electrons during its scanning and a reconstructed image can be made from that information. This recreation of the path as well as the imperfect magnetic lenses also allow SEMs to have a larger amount of depth perception than do regular light microscopes. This can help in determining how well nanostructures are being formed. Along with backscattering, other types of scattering present during the image capture of an SEM are Auger electron emission and emitted X-rays [49, .

Auger emission is a complicated processes that happens when an electron relaxes from a higher energy electron state to a lower state and couples with another electron in the outermost electron shell transferring its energy to that outer shell electron, therefore ejecting the outermost electron from the atom. This action is a byproduct of an incoming electron from the SEM electron source ejecting an electron in an atom through direct collision. If an electron from the SEM electron source ejects another electron during the imaging process, a vacancy where that ejected electron was will be filled by an outer shell electron. As already stated,

Auger emission will occur if another electron in the atom couples with an outer shell electron, giving its energy to the outer shell electron. If this transfer of energy is enough, this outer shell electron will be emitted from the atom. This emitted electron is called an Auger electron, and can be an effective means of electron imaging, but is not typically used as an imaging source for an SEM [44, 50].

X-ray emission is another byproduct of the fact that electron vacancies are created from the bombardment of the sample atoms with the imaging electrons. As mentioned, the bombardment of electrons can create vacancies within the electron shells. The remaining electrons within the atom can then move to lower energy shells and have to release their extra energy due to conservation of energy. Instead of coupling with another electron and emitting an Auger electron, another case exists when the extra energy is released in the form of a characteristic X-ray. These characteristic X-rays have very specific energies dependent on the element that released them and are also dependent on what electron shell transition took place. Therefore detecting the energy of these X-rays can be used as a characterization technique to determine what a sample is comprised of. This technique is called Energy Dispersive X-Ray Spectroscopy (EDS) and is also available to characterize materials using TEM [51]. Due to the availability of the SEM with available EDS equipment, EDS was usually only used while imaging with the TEM.

As stated in the resolution equations of an electron microscope, the resolution depends on the electron potential. Regular SEM imaging takes place between 2kV to 30kV, with the best resolution obtained with the largest potential as dictated by the resolution equations given in the Electron Microscopy Section. Even though the

microscope gains higher resolution when a higher potential is used, the typical potential used during imaging the thin film and nanostructures was 2kV to 5kV. The main reason for this is due to the substrate the seeding layer was grown on for the sample was glass. If a much higher voltage of 30kV was used, there is a higher probability that electrons will have enough energy to pass farther into the sample and the charge can accumulate on the glass substrate. This build up of charges will eventually start to interact with the incoming electrons used for imaging. This complex interaction with the charges will start to make the SEM image useless because the detector can not discern what electrons were accumulated for some time on the charged sample and the backscattered electrons [47, 48, 49, 50, 51] Even though lowering the voltage does not simply mean no charging will occur, this drastically helped when imaging these samples. Another electron microscopy imaging technique is TEM and as it will be noted, TEM uses a much higher voltage than even 30kV allowing for a higher resolution than the SEM. It will show that there are little to no charging worries since the sample preparation is drastically different for TEM than for SEM.

TRANSMISSION ELECTRON MICROSCOPY

Transmission Electron Microscopy (TEM), uses the same fundamental principles as SEM, but uses different electron paths for imaging and a much higher voltage potential of 100kV, which plays a large role in the importance of TEM. First, since the potential is substantially higher in TEM than in SEM, the maximum resolution is much higher and can reach 0.01nm for TEM [47, 48] Second, instead of using the backscattered electrons, TEM uses electrons that have been transmitted

through the sample. Since the electrons interact with the atoms within the material, this slight deflection can be seen and used to make an image onto a phosphorous screen or CCD camera that is in line with the electron source and sample. This makes TEM imaging fundamentally the same as SEM since both microscopes are using electron deflection, just different types of deflection for imaging. Since the TEM requires the electrons to fully pass through the material to image it, the preparation of the samples is drastically different for TEM than for SEM. Since the electrons need to fully pass through the sample in TEM, the sample needs to be thin enough to allow electron transmission. Since the nanowires are on the nanoscale already, the technique to prep the nanowire TEM samples was to simply and physically dislocate the nanowires onto a TEM grid. Therefore using a blade, the nanowires were physically scratched into ethanol, then sonicated for at least 5 minutes, then deposited onto a lacy carbon TEM grid. The TEM grid was then heated to evaporate any remaining ethanol or other liquids or solvents. The preparation for the nanoplatelets was not as simple and required a specialized holding structure. The nanoplatelets needed to be attached to a Silicon (Si) wedge sample holder. The Si wedge is a piece of monocrystalline Si that has been etched into a wedge, allowing for a uniform platform to hold samples to be imaged. The size of the wedge used was approximately 1μ wide at its thinnest point. This wedge then had the AlZnO thin film deposited on it, and the nanoplatelets were grown directly onto this sample holder via the pseudo vapor deposition. The submerged nanoplatelets growth was never tested on this sample holder, therefore all of the TEM image characterization was done on the pseudo vapor grown structures.

Since the environment of the TEM is very controlled, specialized TEM holders can be used to gain more knowledge of a sample. This idea was employed in an attempt to further characterize the ZnO nanowires with an experiment designed to try and characterize the piezoelectric characteristics of the nanowires. Since ZnO is a wurtzite zinc-blend material, the physical displacement of the crystal will result in slightly polarizing the crystal locally, causing the lattice to react to this shift in charge. This reaction can be both a physical movement, or an electrical discharge. This idea can be translated in either applying a physical force on the material and reading its electrical response, or applying an electrical bias to the material and reading its physical response. Since the TEM has a high enough resolution, the physical displacement of the crystal lattice can be seen if a TEM holder can apply an electrical bias to a sample. This idea was translated to an experiment that physically applied a probe to the ZnO nanowire and applied force and a voltage on the nanowire within the TEM. During this experiment, the structure was expected to physically swell and rect to the external forces applied to it. Unfortunately there was no outcome with the experiment. Since this experiment had a timely set up, and required a well-trained technician to do the imaging, this experiment was only attempted once.

DIFFRACTION PATTERN ANALYSIS

A fundamental attribute to TEM is diffraction pattern analysis, and can be viewed as one of its most unique features. This feature comes to fruition due to the scattering of the electrons interacting with the atoms within the sample. When the electron beam travels down the microscope in a parallel path and interacts with the

atoms, the beam will be deflected. If the material is a repeating crystalline material the electron waves will interact with a specific plane of atoms and be scattered at the same angle for each atom in that plane. Since these scattering events happen for every atom within a crystalline plane within a sample, they will be focused by the magnetic lenses in the TEM just like all the other waves. This creates a pattern of dots at the back focal plane within the microscope, and can be observed when the focal plane is shifted from the Gaussian image plane to the back focal plane. As one could imagine, these diffraction patterns will be very characteristic to a given crystalline structure and can even be characteristic to partially crystalline structure.

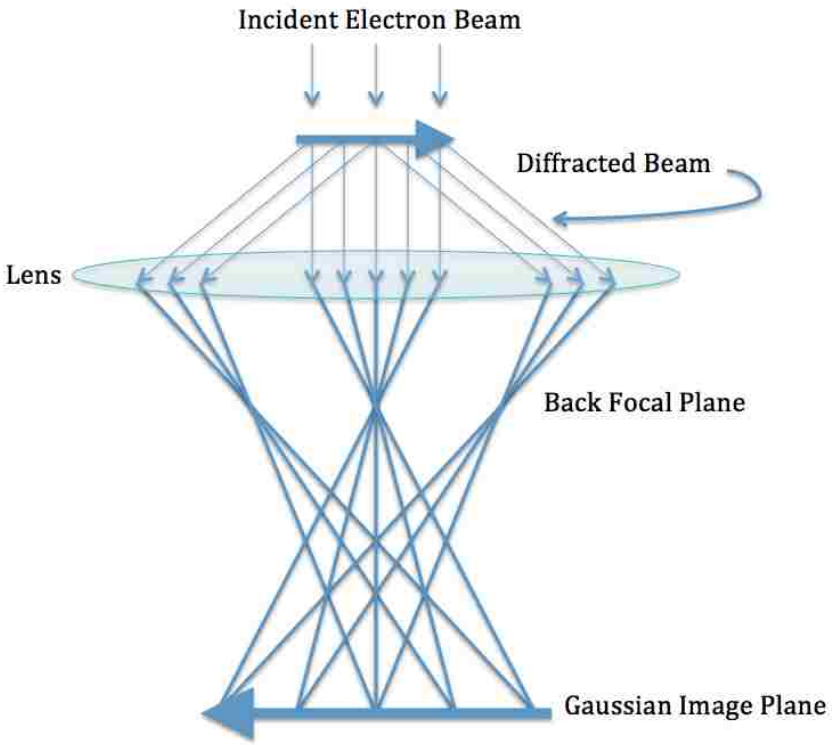

Figure 7: In the above images, it can be seen how the diffracted beams can be used to create a diffraction patter. [47, 48]

As seen in Figure 7, the diffracted beam will then spread out once it has travelled beyond the back focal plane to create a Gaussian image in the Gaussian image plane.

In this example, the diffracted beam, along with the non-diffracted beam converge to create the Gaussian image. This is when the objective aperture is introduced; it can allow for the user to specify which crystalline plane will be allowed through to form the Gaussian image.

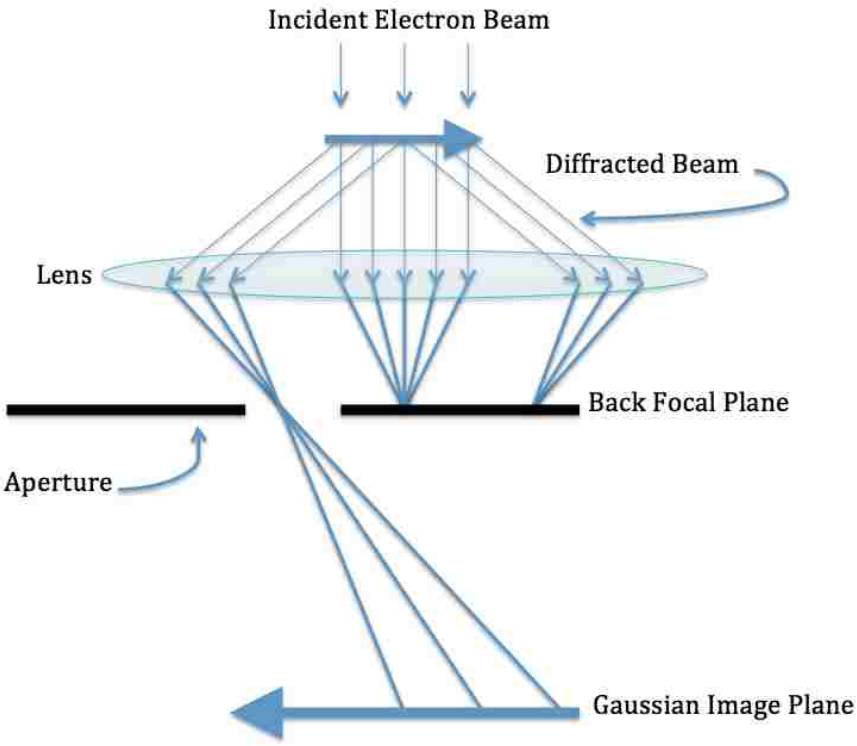

Figure 8: The above image demonstrates the use of an objective aperture to specifically pick a diffraction point that will result in imaging of only that crystal plane. This can be used to highlight defects if they tend to reside in a specific crystal plane [47, 48].

For instance, in Figure 8, if the left diffraction point was allowed through by the objective aperture, and no other diffraction points were, then only the back half of the arrow would be illuminated in the Gaussian image plane. If a sample is highly crystalline, this can help illuminate defects that are only present in specific crystal planes. This type of imaging is called dark field imaging since it is using the lower concentration of scattered electrons to form the image instead of the higher

concentration of the less affected electrons that have little to no scattering through the material. The analogy of the image being 'dark' is made simply because there are far less highly diffracted electrons to form the dark field image, where the bright field had a much higher concentration. Unfortunately, since the nanowires, and nanoplatelets have a large amount of defects, compared to monocrystalline materials, this technique of isolating crystal planes and imaging the dark field had little added benefit. This can be seen in Figure 9 with a side by side comparison of a bright field and dark field image taken using regular TEM and the isolation technique using the diffraction pattern and objective aperture.

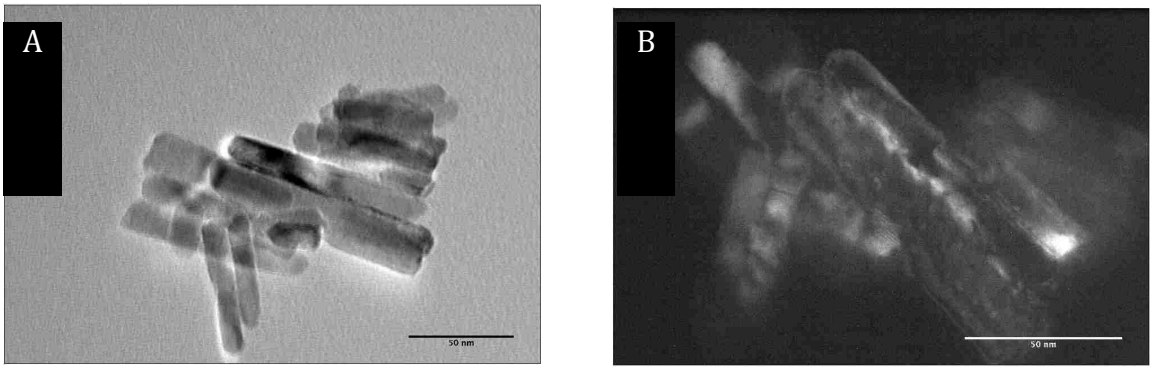

Figure 9: Comparison of light field image to dark field image. As it can be seen when comparing A with B, there was little benefit from isolating the dark field from the light field wen performing diffraction pattern analysis.

SCANNING TRANSMISSION ELECTRON MICROSCOPY

Scanning Transmission Electron Microscopy (STEM) is an extension to regular TEM imaging. As indicated by the name, unlike regular TEM imaging that relies only on a single stationary beam from the electron source as it passes through the sample, STEM employs a scanned beam across the surface of the sample. This scanning motion constructs an image from the scanning motion in a similar manner that SEM images are constructed. The difference in STEM and SEM, is in STEM the

detected electrons during the scanning are not backscattered electrons, but scattered electrons that take the same path as the electrons used in diffraction patterns. This technique has an advantage in being able to collect bright field images and dark field images simultaneously, as well as having much higher contrast between two different material types than in regular TEM imaging. Since the image was being scanned in the same manner as the SEM, a direct link of the scan location and the received diffracted image location on the detector can allow for a diffracted dark field image to be easily created along with the bright field image. The simultaneous bright field and dark field imaging was a secondary outcome to what the STEM's intended use was for this research, which was to image with a higher contrast between different materials than regular TEM imaging. Therefore when imaging any inorganic nanowire with an organic porphyrin coating on it, the high contrast between the inorganic nanowires and the organic porphyrin allowed for positive distinction that the porphyrin was coating the nanowire in the way it was intended. This contrast can be seen in the following image.

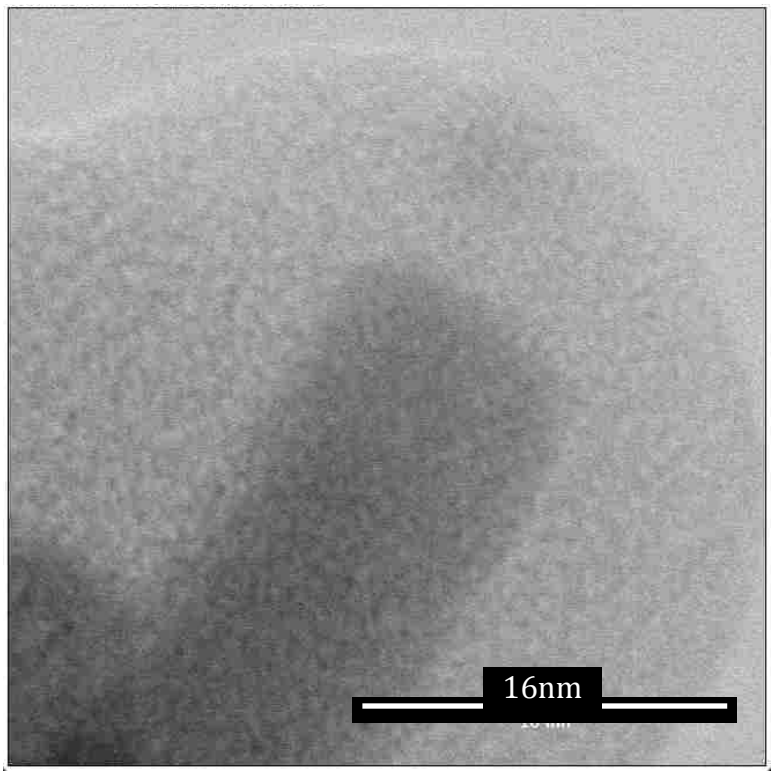

Figure 10: STEM image showing the contrast between the dark non-organic nanowire covered with an organic porphyrin.

This imaging allowed a positive confirmation that the porphyrin was uniformly coating the nanowires. This method was employed to determine if the porphyrin was coating both ZnO nanowires and BiTe nanowires and will be further detailed in Chapter 3.

X-RAY DIFFRACTION

Further analysis of the crystalline structure was done using X-Ray Diffraction (XRD). The mechanics of XRD are similar to diffraction pattern analysis in that they both work on the principle of a wave interacting with the atoms within an atom and being diffracted in another direction during contact. The main difference in XRD and TEM diffraction pattern analysis is that XRD of course uses an X-ray beam instead of

an electron beam, as well as the sample is systematically being rotated to cycle through all angles of possible deflection. This is different than the interaction of electrons with a crystal lattice since the electrons will deflect in all possible directions without needing to approach the surface at different angles [52].

The deflection of X-rays in XRD only occur when there is constructive interference between a crystal plane and the X-ray that are dictated by the Bragg equation,

$$n\lambda = 2dsin(\theta)$$

This condition only occurs when the deflection at all the crystal planes is at the same angle.

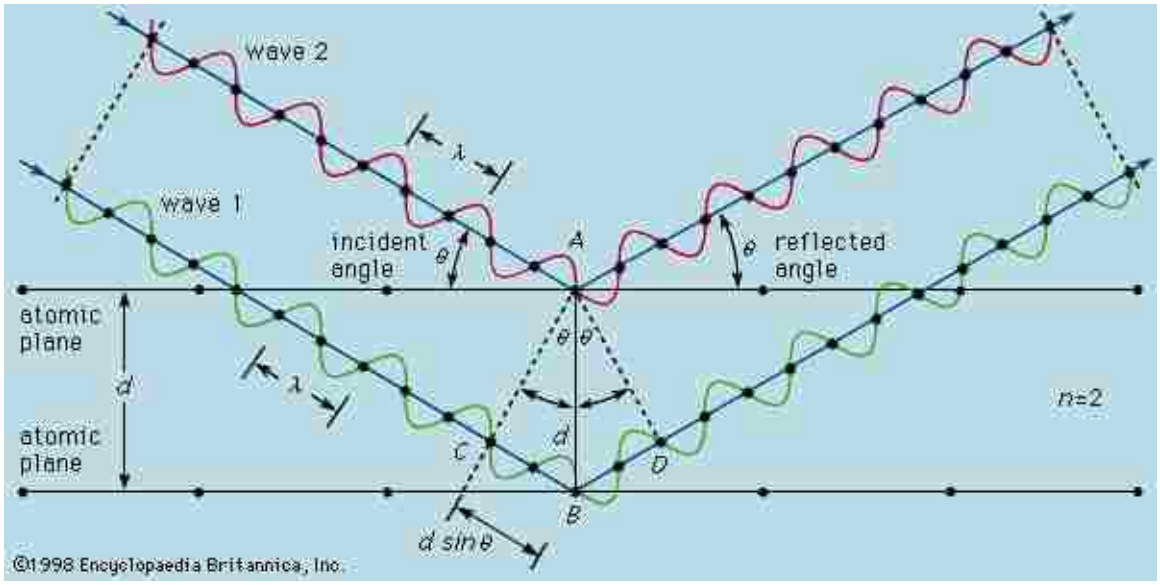

Figure 11: Diagram of Bragg condition taken from the Britannica website[53].

The Bragg condition therefore states there will only be diffraction when the sample is imaged at an angle that has constructive interference. It will be shown later on that both the nanowires and nanoplatelets were analyzed using XRD to determine if they have similar crystal lattices.

ABSORPTION SPECTRAL ANALYSIS (UV-VIS)

The absorption spectral analysis was characterized for the ZnO nanowires at different growth characteristics to determine how the transmissivity of the structures were effected by the growth characteristics. The experiment to determine the absorption spectral analysis was done using a Varian Cary 6000i spectrophotometer. This tool uses specialized optics to shine monochromatic light at incrementing wavelengths from 300nm to 1000nm with a precision down to the nm for most of the range.

This device then uses an InGaAs detector to detect what wavelengths have been deflected by the sample, and by what percentage. Therefore the system is calibrated to cancel out the background noise of the system, then the sample is placed in the beam path of the machine and the measurement is taken. The machine will then detect how much light was deflected by the sample.

CONTACT ATOMIC FORCE MICROSCOPY

Atomic Force Microscopy (AFM) and Conductive Atomic Force Microscopy (CAFM) is another form of microscopy used to image nanoscale samples other than electron microscopy. As it would be implied, AFM and CAFM use atomic forces as their means of imaging. This is done by having a cantilever with a very fine tipped needle attached to it either coming in direct contact with a sample in contact mode, or is vibrated just above the sample in tapping mode. This cantilever is then moved over the sample to capture an image of the samples surface. The deflection of the cantilever as the atomic forces push it is detected by using a laser that is shinned on the top of the cantilever and deflected back onto a detector. The detector will be

able to detect if the cantilever has moved since the path of the laser will change if the cantilever has moved. This movement of the laser on the detector can use simple vector calculations to determine how high or low the sample is at that given point of contact with the cantilever and the sample. This is done continuously over the sample and a three dimensional, topographic image is constructed. The same mechanism is used for both the contact mode AFM that comes in direct contact with the sample, as well as non-contact tapping mode which has the cantilever oscillate above the surface. As viewed below, as the cantilever oscillates above the sample, the force the sample has on the cantilever will still physically push up the cantilever which will then be detected by the detector [54].

With the oscillation of the cantilever usually in the kilohertz range, the precision of the system will be in the nanometer range as long as the point of the contact is fine enough. With the machine used to gather data, the tips were on the order of 30nm^2 area which will allow for imaging on the nm scale. As the system images the sample, the tips will inherently start to begin to dull down or will have a defect or dust attached to the tip. Therefore the tips do need to be changed regularly.

A great quality of the AFM system is its ability to determine the roughness of a sample and to build a topographic view of the imaged sample. This type of analysis for electron microscopy is lacking since this would need to be calculated by hand using electron microscopy. The other ability of the AFM system is its ability to make conductivity tests.

CAFM uses the fact that the tip of the microscope is in contact with the surface of the sample, a voltage can be applied to the tip, and if the sample and the tip are conductive, the conductivity of the sample can be measured. By using conductive AFM tips, the conductivity of the nanowire and nanoplatelet samples were measured. The system automatically takes out the resistance of the system during measurements, therefore the conductivity of just the sample was easily obtained. Since the conductivity of the entire sample was collected during this measurement, the conductivity of not only the nanostructure was collected, but also the thin film. Therefore when the measurement was made, the resistance of the nanostructure with the thin film needed to be considered. The conductivity data was collected for the doped and the non-doped ZnO nanowires and nanoplatelets.

CHAPTER 3

To try and capture the analysis of the data for the nanowires and nanoplatelets in the most concise manner, this chapter is broken up into the different analysis techniques for the nanowires, then nanoplatelets. It will be stated if the analysis is for non-doped or doped structures, as not all analysis techniques were used for both non-doped and doped nanostructures. This was either due to a conscious decision or due to the lack of time and availability of machines and will be stated for clarity.

SEM NANOWIRES, NON-DOPED AND DOPED

The first analysis technique used after all nanostructure growths was imaging using Scanning Electron Microscopy (SEM). This was the easiest technique to confirm the growth of the nanostructures and became an indispensable tool very early on in the development of the nanostructure growth due to its ease of use, even though there were several un-teachable skills that could only be obtained through practice.

The first set of data that will be presented are images of the seeding layers. The first seeding layer used was a Sol-Gel conductive spin coated layer on glass.

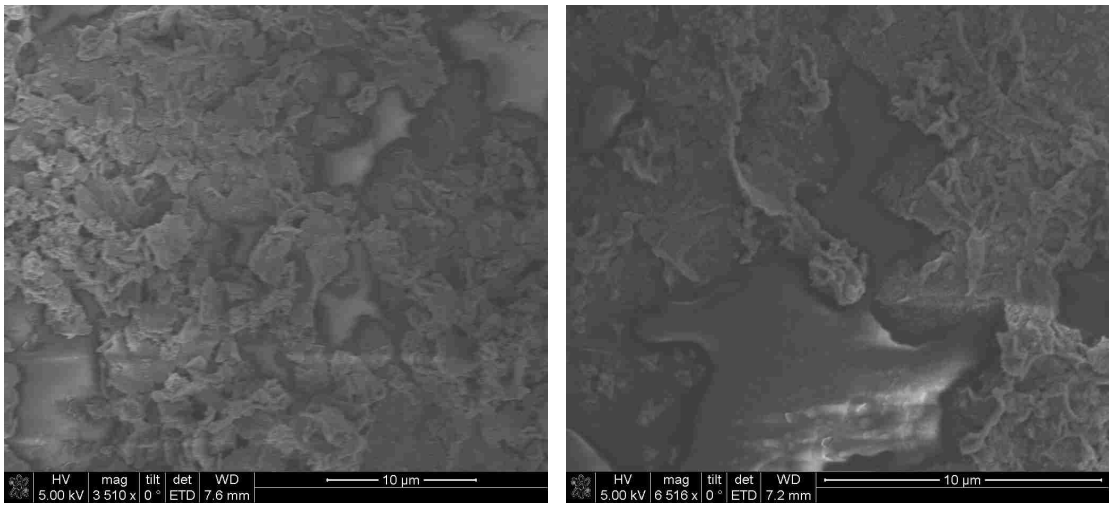

Figure 12: It can be seen that the spin coated samples are very rough and inconsistent. It can also be seen with the charging that it does not coat the glass surface consistently.

As seen in Figure 12 the seeding layer was not uniform, as these imperfections where large and spanned the entire sample. These imperfections can be mitigated by researching the spin coating method, but it was decided to use a highly uniform seeding layer that already had a developed process associated with it. This process was to grow a thin film of Aluminum doped Zinc Oxide. The process had already been developed at Sandia National Laboratories Center for Integrated Nano Technologies and all the equipment and materials were available.

The second used seeding layer of AlZnO thin film was grown via Physical Vapor Deposition (PVD) using a Kurt J. Lesker PVD75 machine using a 99.999% pure ZnO target with a doping concentration of 2% Al. This thin film was the seeding layer that replaced the Sol-Gel seeding layer very early in the research due to its highly uniform growth and repeatability that required no extra development time. The only added time using this new thin film was the learning required to use the highly automated Kurt J. Lesker PVD75 machine.

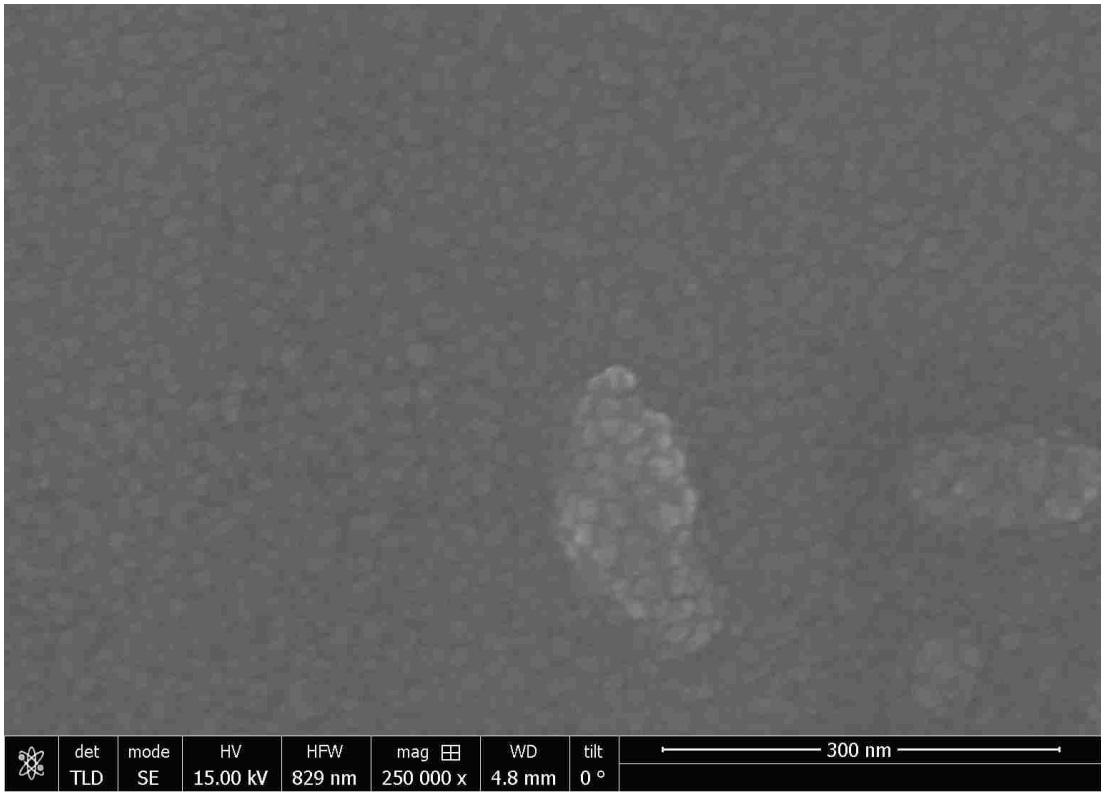

Figure 13: SEM image of thin film. The imperfection in the film was used for focusing purpose and is a rare occurrence in the film.

In the images of the AlZnO thin film, the average size of the seeds are 15-20nm. This is a very important note since the average diameter of the nanowires grown on this substrate is 25nm-35nm depending on the growth parameters. This shows that the nanowires use one to three seeds to start the growth depending on the growth parameters since the size is within error or measurment and standard deviation of the seeding layer size. Therefore the seeding layer has a limiting factor on the size of the diameter of the nanowires. The thin film thickness average was measured as 45nm. This can be seen in the side profile images to follow of the non-doped and doped nanowires.

Following is a set of images of non-doped and doped nanowires that have been grown at varying temperatures. The doped nanowires were doped at 3%

concentration of Aluminum to Zinc. As stated in the synthesis section of the aqueous solution, the Aluminum Nitrate Nonahydrate (Al Nitrate) and the Zinc Nitrate Hexahydrate (Zn Nitrate) are suggested to disassociate the same way, therefore it can be suggested ideally that every Aluminum atom introduced will replace a Zinc atom in the crystal structure [32, 33]. Future testing will have to confirm this ideology.

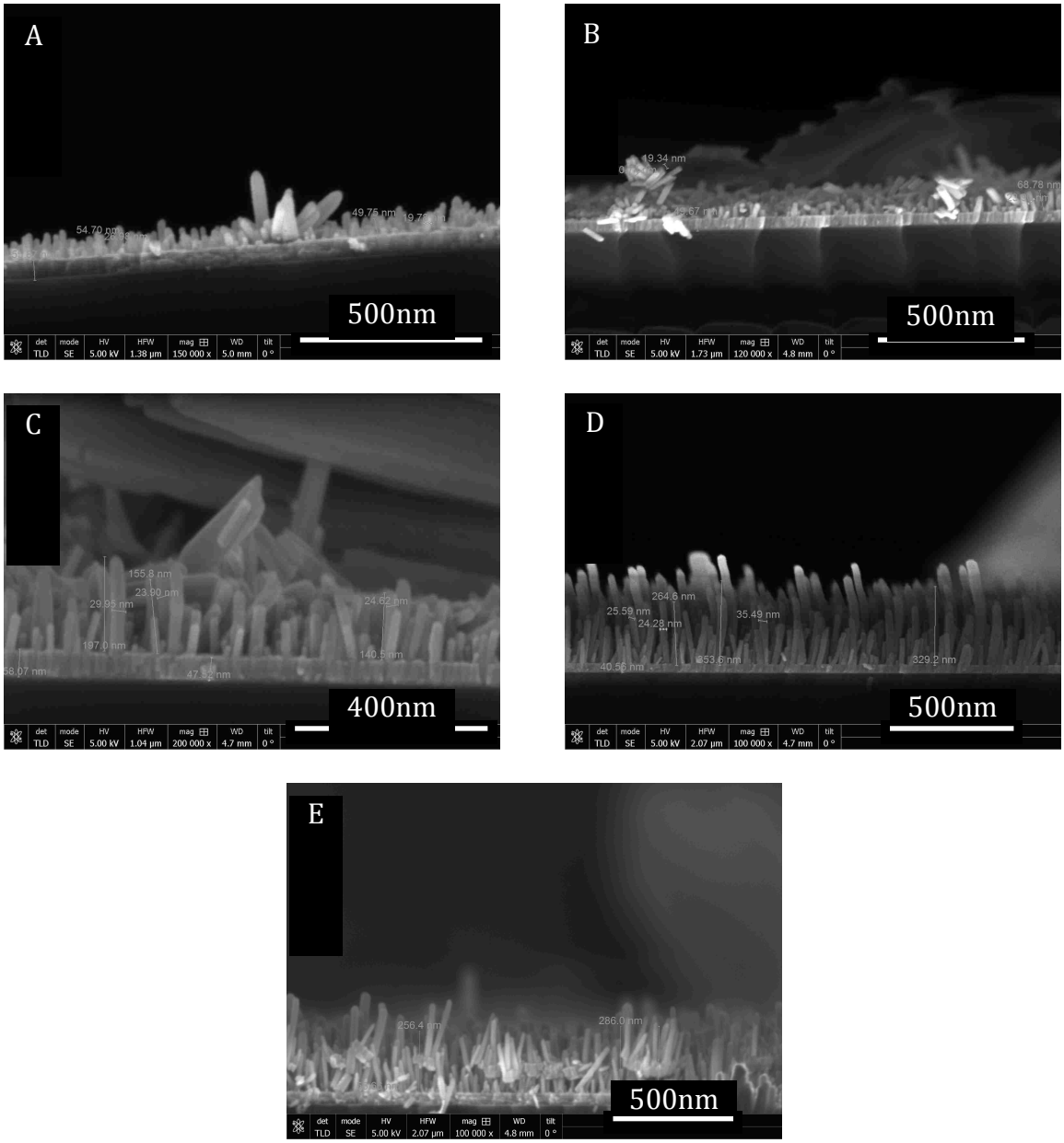

Figure 14. Side profile of the non-doped nanowires can be seen at different temperatures. Temperatures of 50°C, 60°C, 70°C, 80°, and 90°C correspond to Figures labeled A, B, C, D, and E.

These images show that as the growth temperature was increased for the 0.01M:0.01M, Zn Nitrate to HMA solution growths, the lengths of the nanowires increased, but the diameters stayed relatively the same. Therefore the aspect ratio also increased as the temperature increased. As the temperature of the growth

increased, the increase in length was expected and it can be approximated that the lengths increase linearly as the growth temperature is increased.

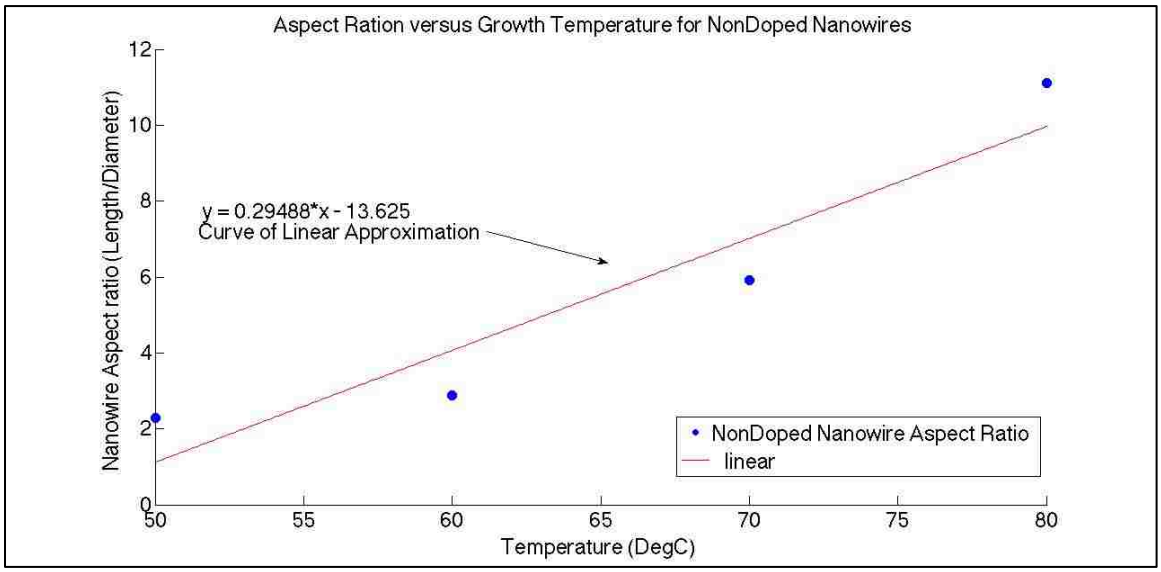

Figure 15: The aspect ratio of the nondoped nanowires can be approximated as a linear increase as the temperature of the growth is increased. The approximation states that for every increase of one degree of the growth solution, an increase of approximately 0.294 in the aspect ratio is achieved.

Seen in Figure 15, the average aspect ratio increases is a linear approximation. For every increase in one degree Celsius of the solution, approximately a 0.294 increase is seen in the aspect ratio. The data for the average diameter and length show an increasing behavior as the temperature of the growth solution increased.

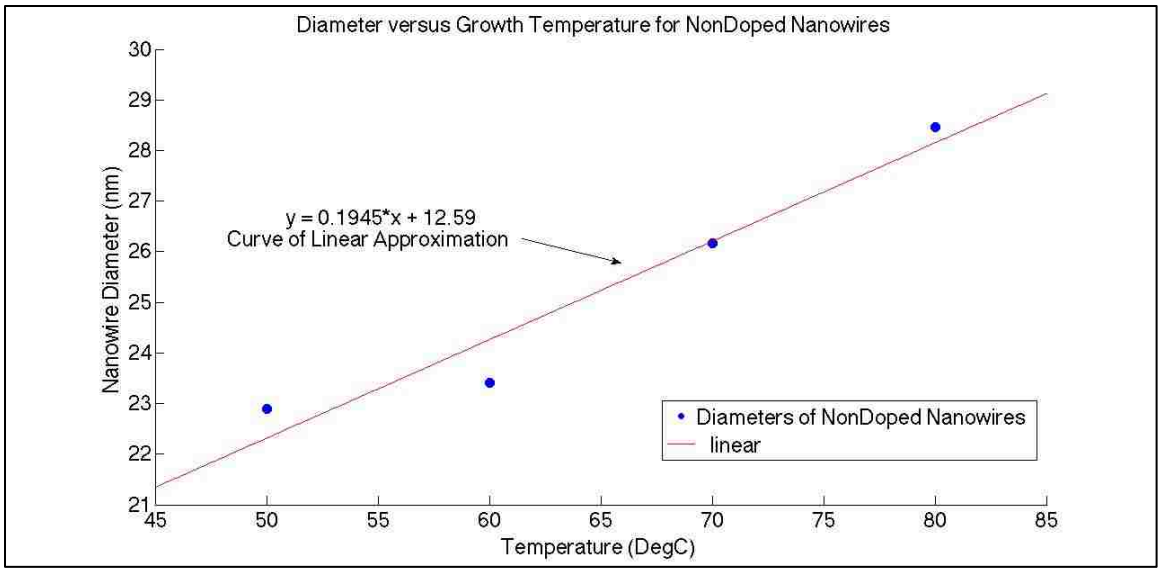

Figure 16: The data shows an increase in the diameter of the nanowires.

It was unexpected to see an increase in the diameter of the nanowires as the temperature increased. It was more expected to see a constant diameter with the increase in temperature. The increase in the diameter is very small and the average diameter may indeed be a constant if more testing is conducted, but the given data suggests that the diameter is still limited by the seed size. This data suggests that the nanowires possible use multiple seeds to grow from, and with a higher energy, this becomes more probable that at lower energies. More extensive testing of growth temperatures and analysis of the nanowire diameters would need to be conducted to confirm this suggestion.

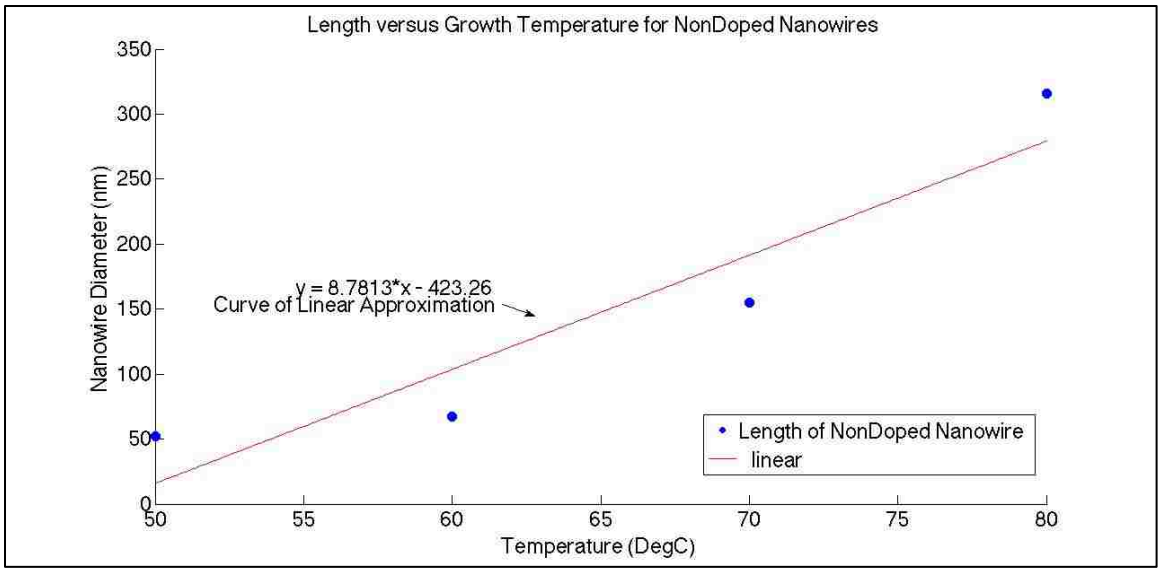

Figure 17: The increase of the length of the nondoped nanowires was approximated as being a linear increase of length to increase of temperature.

The same conclusion of a clear increase in nanowire aspect ratio with increase of solution temperature cannot definitively be said for the doped nanowires. Due to only having three data points for averages of the doped nanowire aspect ratio, the linear approximation was skewed. With further experimentation of the nanowire length and the dependence on length when compared to the dopant, a more definitive conclusion can be made.

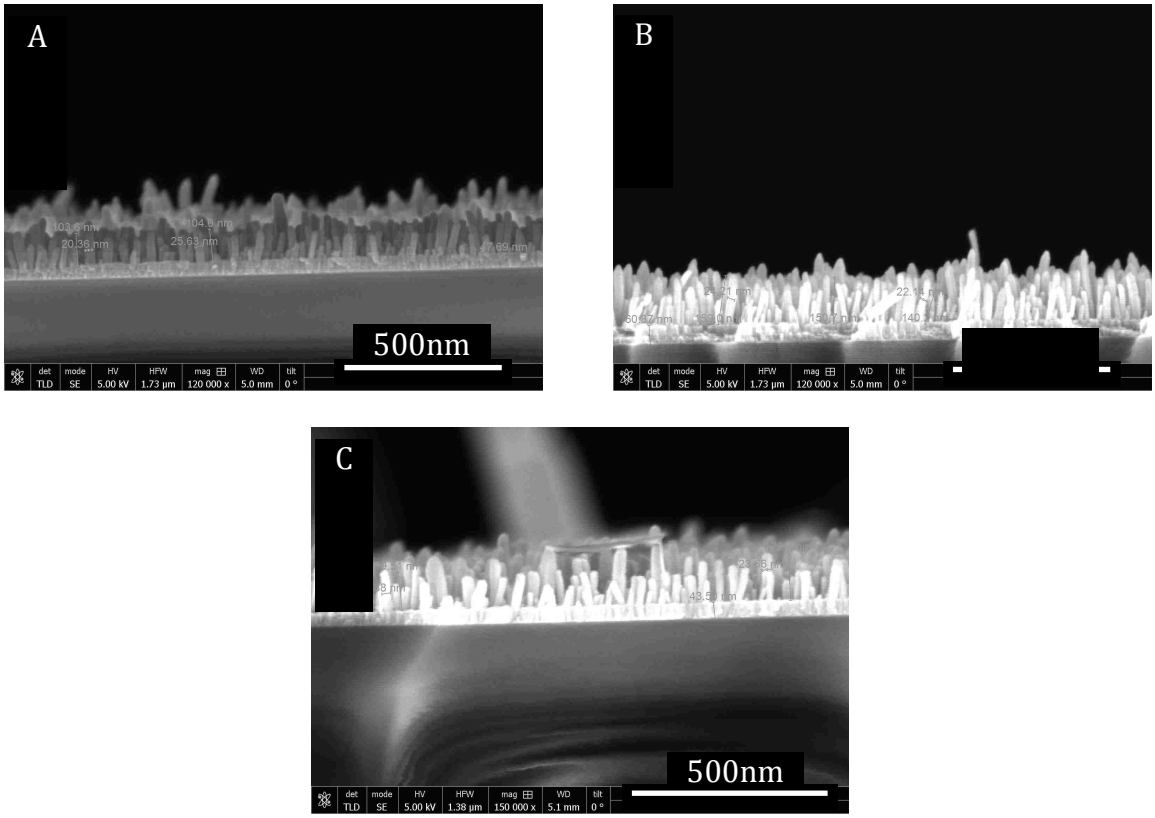

Figure 18. Side profiles of the doped nanowires grown at different temperatures. Temperatures of 60°C, 70°C, and 80° correspond to images labeled A, B, and C.

It can be seen in the images that the length of the nanowires is much more stable in the doped nanowires. The average of the 80°C doped nanowire growth actually went down substantially when compared to the length of the 70°C growth. This may be contributed to the particular area that the length was measured at that had something hindering the growth of the nanowires such as the location with respect the edge of the sample. No special treatment was taken to ensure the general location of the samples were being used, the sample was simply measured where the sample happened to break cleanly.

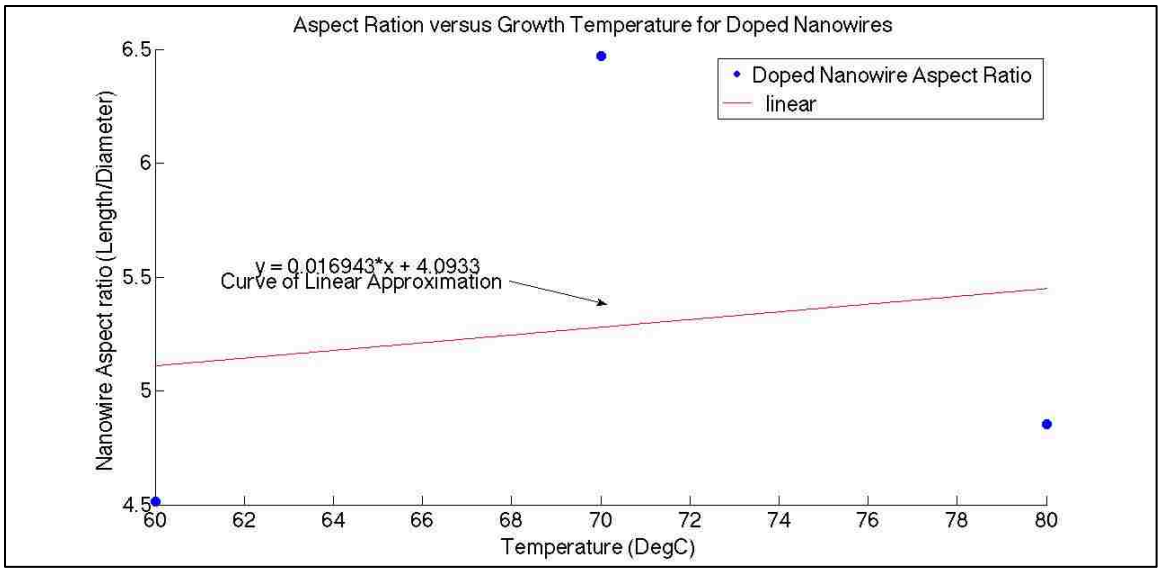

Figure 19: The increase in doped nanowire length versus temperature was inconclusive.

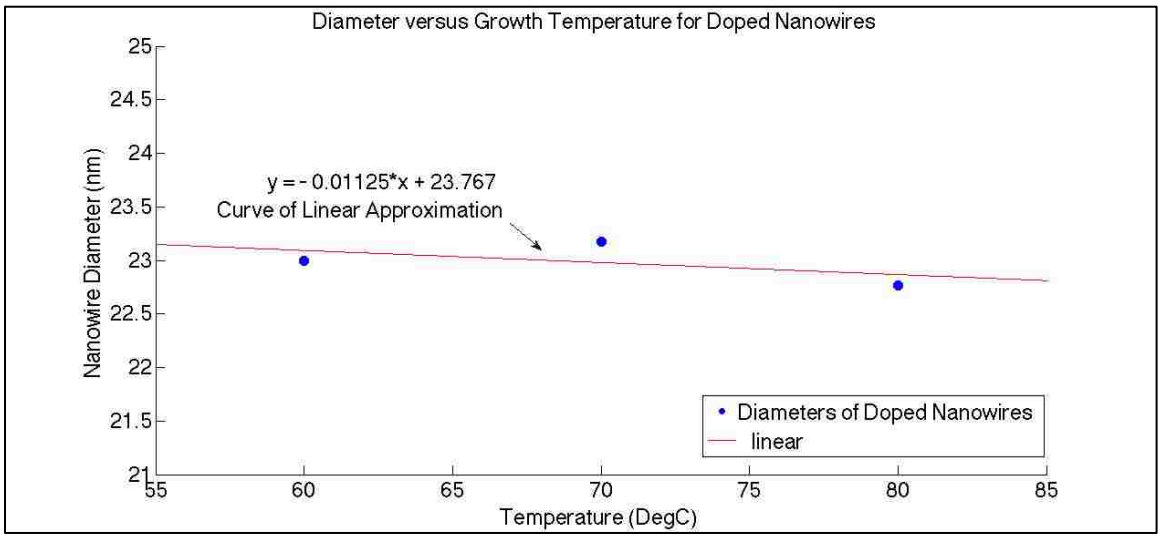

Figure 20: Doped nanowire diameter versus temperature. With a linear decrease in the diameter of the doped nanowires, it can be suggested that the diameter can be approximates as being constant and the downward trend is due to error in the measurement.

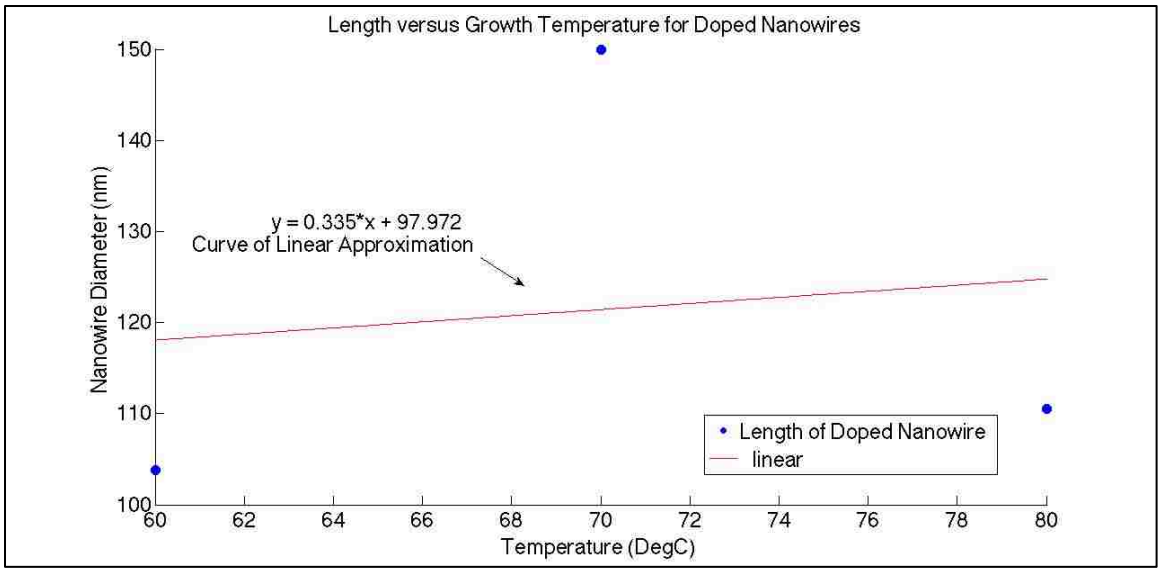

Figure 21: Aspect ratio of doped nanowires versus temperature. As it can also be seen with the aspect ratio versus temperature graph for the doped nanowires, the outcome is inconclusive.

It was not determined why the doping caused such a change in the length grown of the nanowires and to fully understand the reaction of the Al Nitrate with the Zn Nitrate and HMA further studies will need to take place.

SEM NANOPLATELETS NON-DOPED AND DOPED

The nanoplatelets were imaged for both their pseudo-vapor and submerged growths. The nanoplatelets were doped only for their vapor growth, since this growth procedure was much more developed than the submerged growth technique. The nanoplatelets form in high concentrations when grown in the pseudo-vapor growth technique and are uniform in size. This can be seen in the following images.

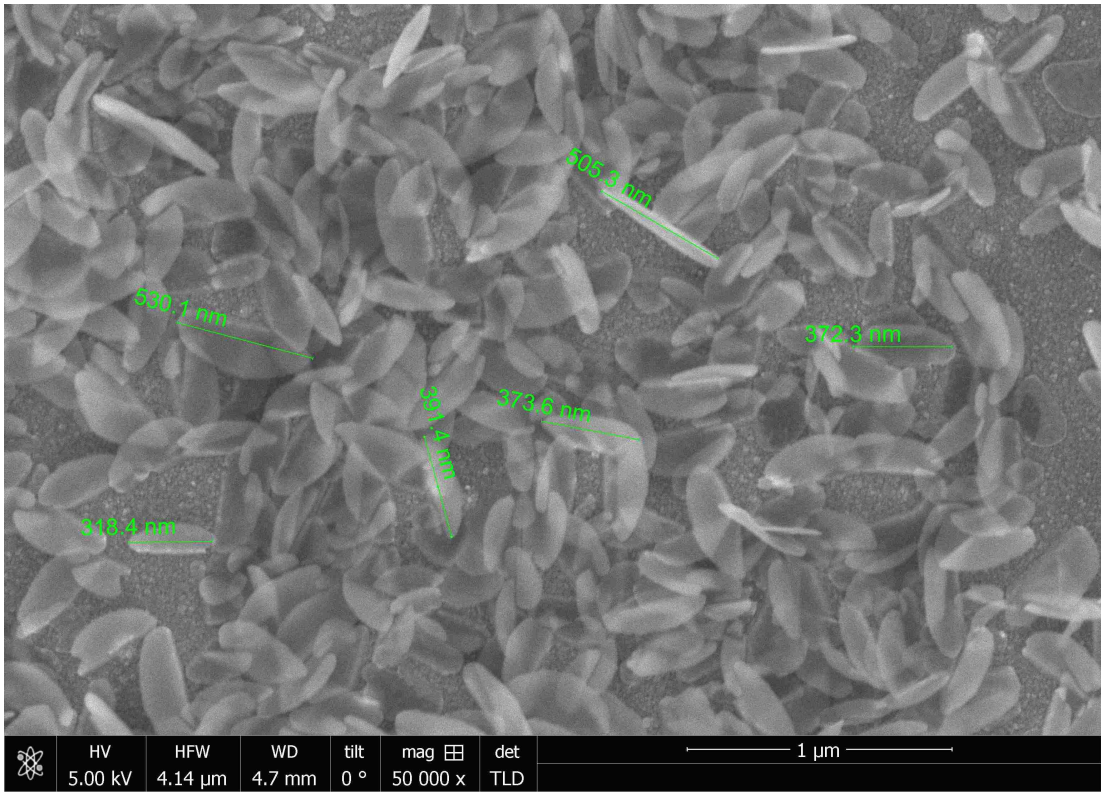

Figure 22. SEM image of the nanoplatelets grown via the pseudo vapor deposition. As it can be seen in the image, the diameter of the nanoplatelets is approximately 400nm.

As seen in the SEM images, the nanoplatelets grow in clusters and can intertwine with one another. The average size of the nanowires is 500nm in diameter and less than 20nm in thickness. From performing several growths at different lengths in time, it appears that the nanowires are self-limiting in size since the average size stays near the same.

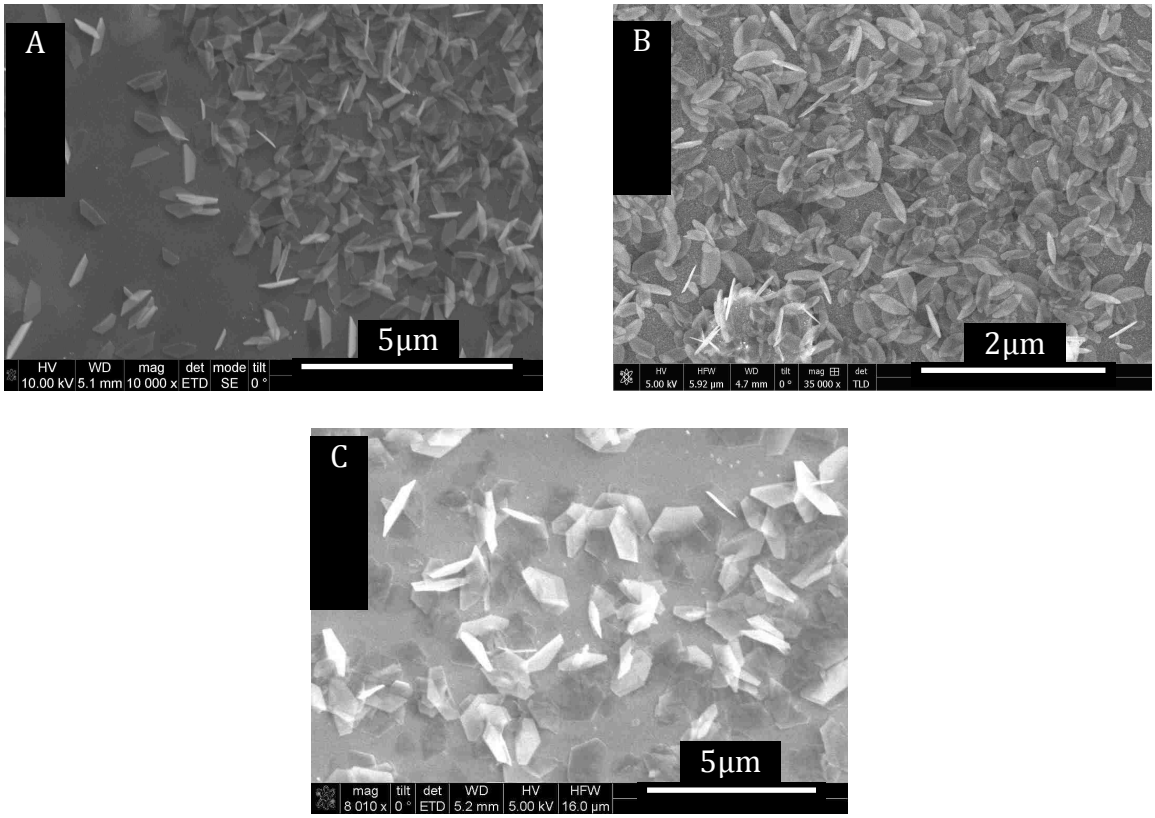

Figure 23. The nanoplatelet growth time did not have as much of an affect on the growth characteristics as it did for the nanowires. As it can be seen in the above images, the size of the nanoplatelets did not change when the growth time was changed. The growth times for the above images were 16 hours, 18 hours, and 24 hours respectively for images A, B, and C.

Once the nanoplatelet growth was observed, it was attempted to grow them in a more controlled environment other than in the very dynamic pseudo vapor growth. Since the substrates temperature was being effected not only by the air temperature outside of the beaker as well as the temperature of the condensing vapor, the temperature could not be assumed to be stable. The temperature of the substrate was measure at approximately 63°C when the solution was kept at 75°C during the pseudo vapor growth. It can not be assumed that the supply of the reactants is constantly being resupplied, because the only convection of the system was the natural convection of the vapor condensing on the sample and dripping from the

sample. This is a self-limiting processes, but could not be controlled in any form with the set up used.

It was decided that the key factors that were changed by taking the substrate out of the solution and placing the substrate in the vapor during growth was the temperature and the molarity concentration. This conclusion lead to several tests of lowering the temperature and the molarity of the aqueous solution, and placing the substrate back in the solution to see how the growth of the nanostructures were effected. It was decided to grow at equal parts of Zn Nitrate to HMA each at a molarity of 0.0005M, this was decided simply by having a repeatable processes that required less than 400mL of water for processing. This limit was set to keep the process as simple as possible during testing. The outcomes of the experimentation lead to completely interwoven nanoplatelets, as well as individual nanoplatelet growth. This showed that at the very least, the temperature and the molarity of reactants have a crucial role in the growth of the ZnO nanostructures.

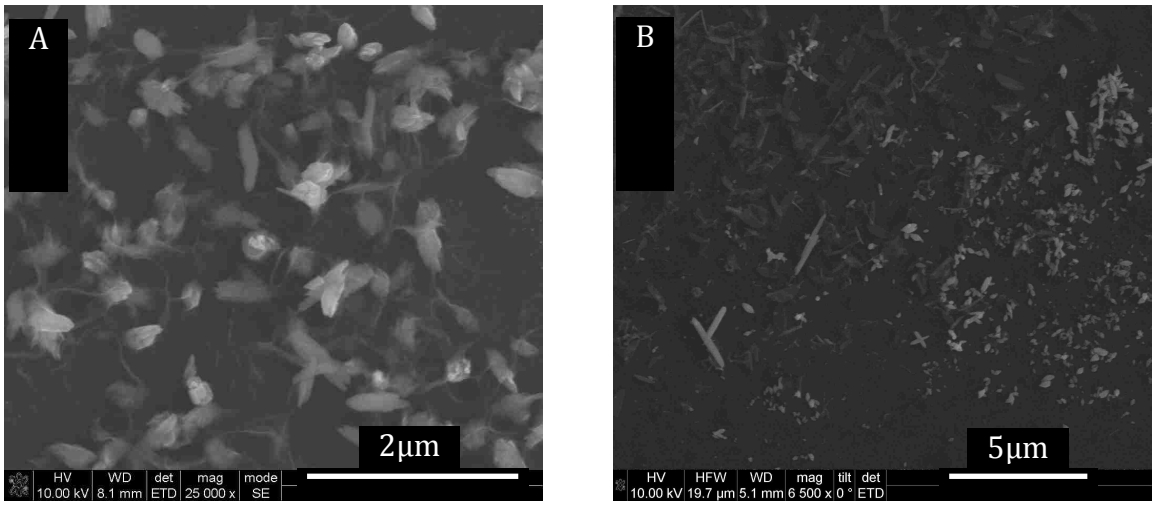

Figure 24: The images show a one to one ratio growth of aqueous Zn Nitrate to HMA at a very low molar concentration of 0.0005M. Image A is at a temperature of 70°C and image B is at 65°C. Both growths were for two hours.

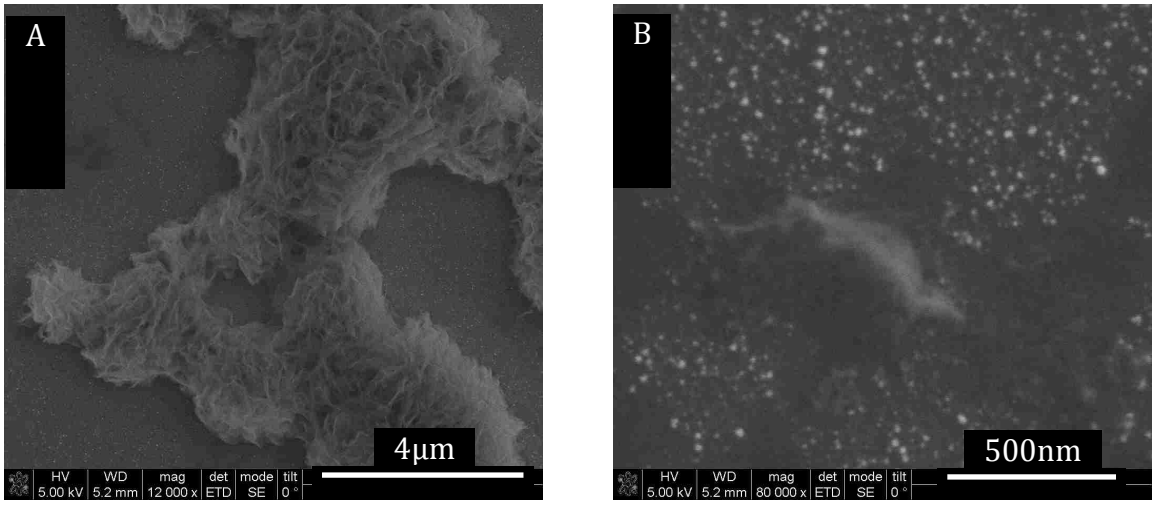

Figure 25: The images show a one to one ratio growth of aqueous Zn Nitrate to HMA at a very low molar concentration of 0.0005M. Both image A and B were grown at a temperature of 62.5°C for two hours.

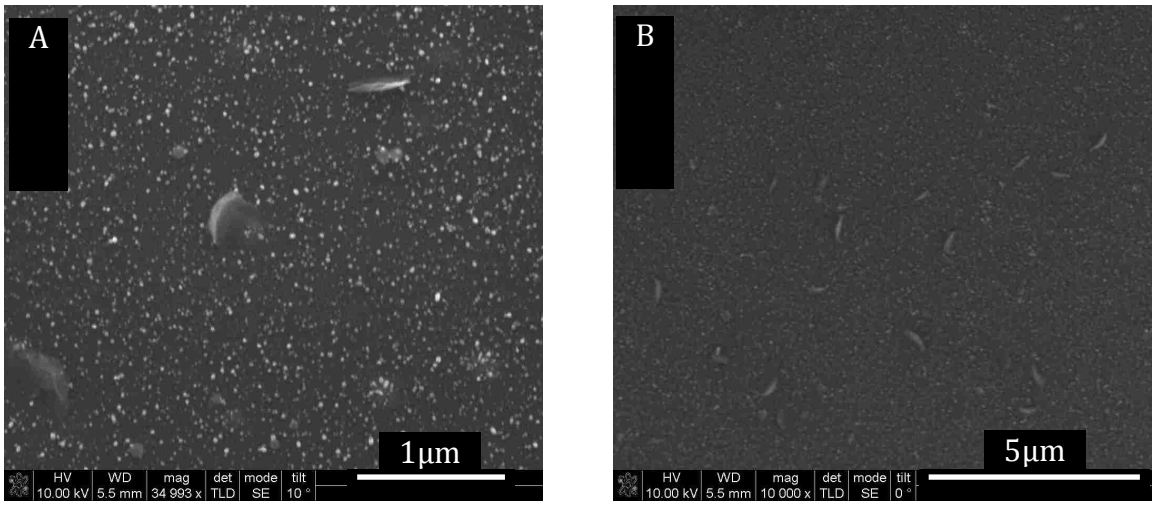

Figure 26: The images show a one to one ratio growth of aqueous Zn Nitrate to HMA at a very low molar concentration of 0.0005M. Both image A and B were grown at a temperature of 60°C for two hours.

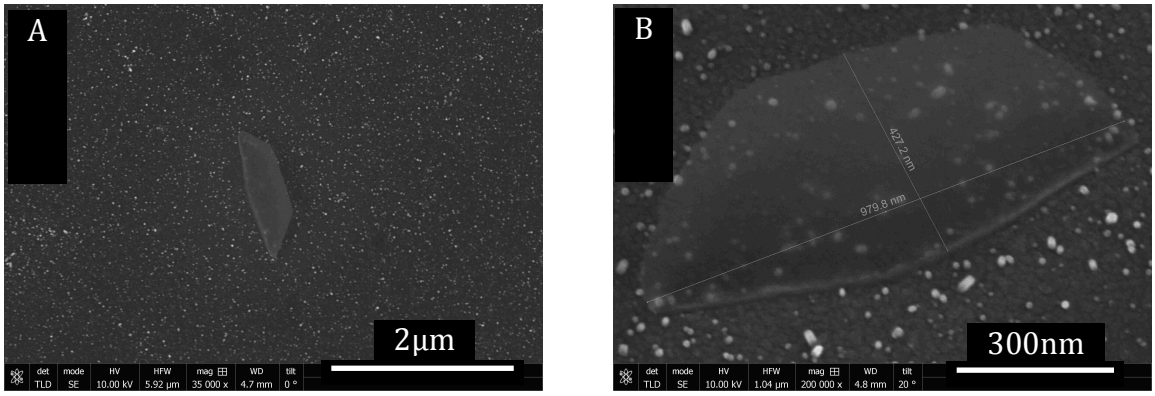

Figure 27: The images show a one to one ratio growth of aqueous Zn Nitrate to HMA at a very low molar concentration of 0.0005M. Both image A and B were grown at a temperature of 50°C for four hours.

It was shown that by limiting the temperature of the solution and the molarity, that the growth of nanoplatelets is produced in the same fashion as in the aqueous solution as they would when grown in the vapor of the solution, proving temperature and molarity has a role in the synthesis of the ZnO nanostructures.

Since it was shown that the nanowires could be doped to some extent of success, it was attempted to dope the nanoplatelets. Since the pseudo vapor growth was the more studied growth procedure, it was determined to attempt doping the nanoplatelets for this growth procedure. In the same manner that the nanowire solution had Al Nitrate introduced to the aqueous solution, it was added to the solution during the nanoplatelet growth. The resulting growth was nanoplatelets that appeared under the SEM as being very similar to the nanoplatelets grown without the dopant. It was noted that the density was approximately half or less than without the dopant present. To fully understand why this happens, a further study would need to be taken.

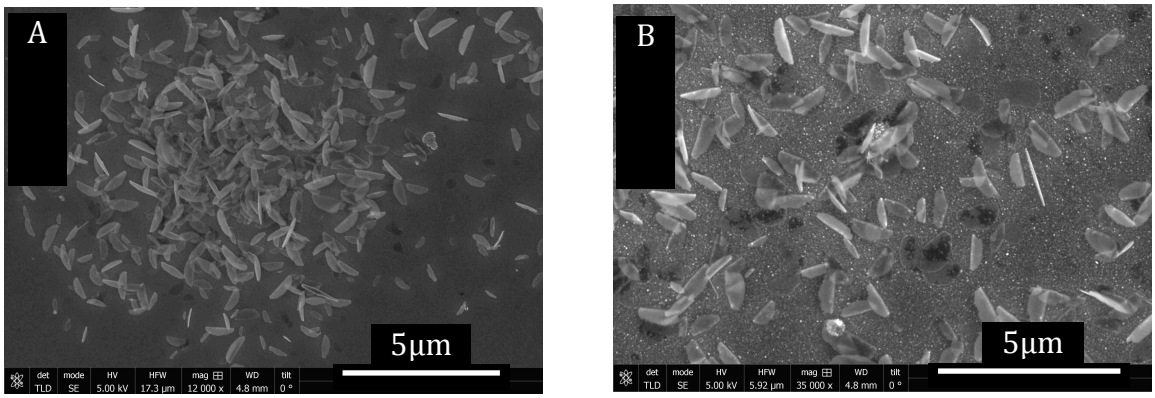

Figure 28. SEM of non-doped nanoplatelets and doped nanoplatelets. As can be seen in the above images with A being non-doped nanoplatelets and B being doped nanoplatelets, the general size of the nanoplatelets did not change when the Al dopant was introduced during the growth. The density did slightly decrease as it did with nanowires.

Further information will be discussed on the doped nanowires and nanoplatelets in the CAFM section.

TEM

Transmission Electron Microscopy (TEM) is an invaluable tool when characterizing nanostructures. The ability to image sub-nano meter lengths can allow a person to study the defects in a crystal growth processes or confirm if a growth is crystalline at all. Regular TEM imaging was used for the characterization of primarily the non-doped nanowires and nanoplatelets. The main reason for the limited use of the TEM is the enormous learning curve associated with the tool. After over two years of limited use with the machine and taking a class dedicated to the physics associated with the machine, there is still some troubles associated with skill on the machine that will only be resolved with future hours on the machine.

TEM sample preparation for the nanowires and the nanoplatelets was drastically different, and had drastically different preparation times associated with them. The sample preparation for the nanowires was a simple processes and usually

took less than 30 minutes, were the preparation of the nanoplatelet sample took over 16 hours to prep (See Chapter 2, Seeding Layer and Chapter 2 Aqueous Growth sections for full details on the preparation techniques). This drastic difference in preparation time affected the outcome of the amount of data collected for the nanoplatelets when compared to the nanowires. Especially since it was not guarantied to acquire usable data from any TEM sample no mater the preparation technique. None the less, some compelling information was collected on the grown nanoplatelets and a comparison could be drawn about the different crystal structures of the nanowires and nanoplatelets.

Following are images taken of the non-doped nanowires and non-doped nanoplatelets.

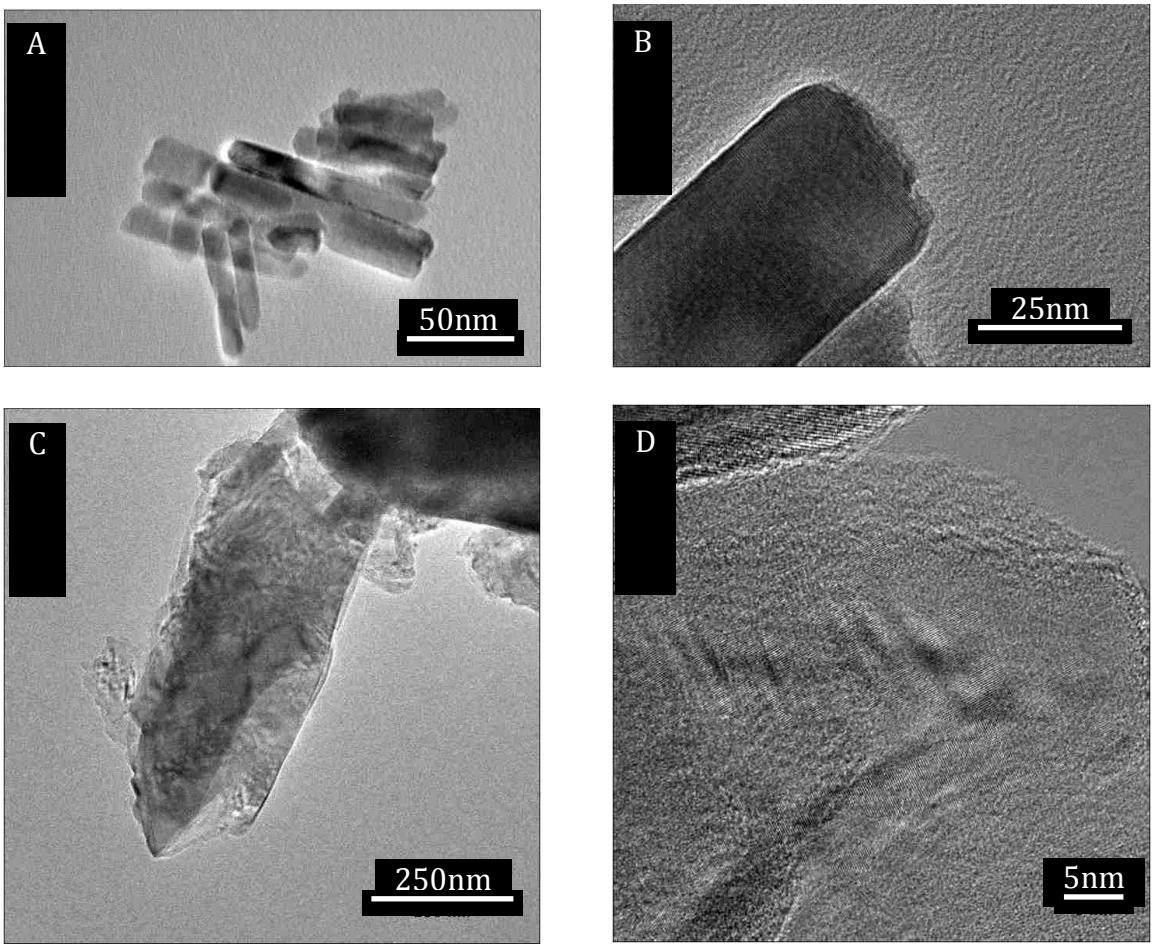

Figure 29. TEM images of nanowires and nanoplatelets with A and B being images of nanowires and C and D being images of nanoplatelets.

As can be seen in the TEM images of the nanowires and nanoplatelets, there is some visible lattice fringing occurring, giving an initial indication that the structures are crystalline. Even though this confirms that there is at least some order of crystallinity occurring between the two different crystal structures, further analysis needed to be conducted to gain further information on the crystals and their crystal orientations.

NANOPROBE EXPERIMENT

Before further analysis of the nanowire and nanoplatelet crystal structure is

discussed, an experiment that was conducted using simple TEM imaging and a specialized sample holder will be presented. An experiment using a nanoprobe was conducted with CINT scientist Dr. Katherine Jungjohann. Dr. Jungjohann used an in situ holder to apply an electrical bias and physical force on a ZnO nanowire and imaged the response of the nanostructure. This experiment was unsuccessful in it's attempt to record the a piezoelectric response from the nanowire which was the overall outcome of the experiment. It was able to show that the applied electrical bias did affect the nanowires in some fashion. This was observed with the change in the contrast of the nanowires while a bias was applied to the nanowires during the experiment. It was suspected, but not confirmed that the cause of the change in the contrast was due to the interaction of the electrical current and the defects within the nanowires. It was intended to attempt the experiment again to gain further knowledge and confirm this, but was not fulfilled.

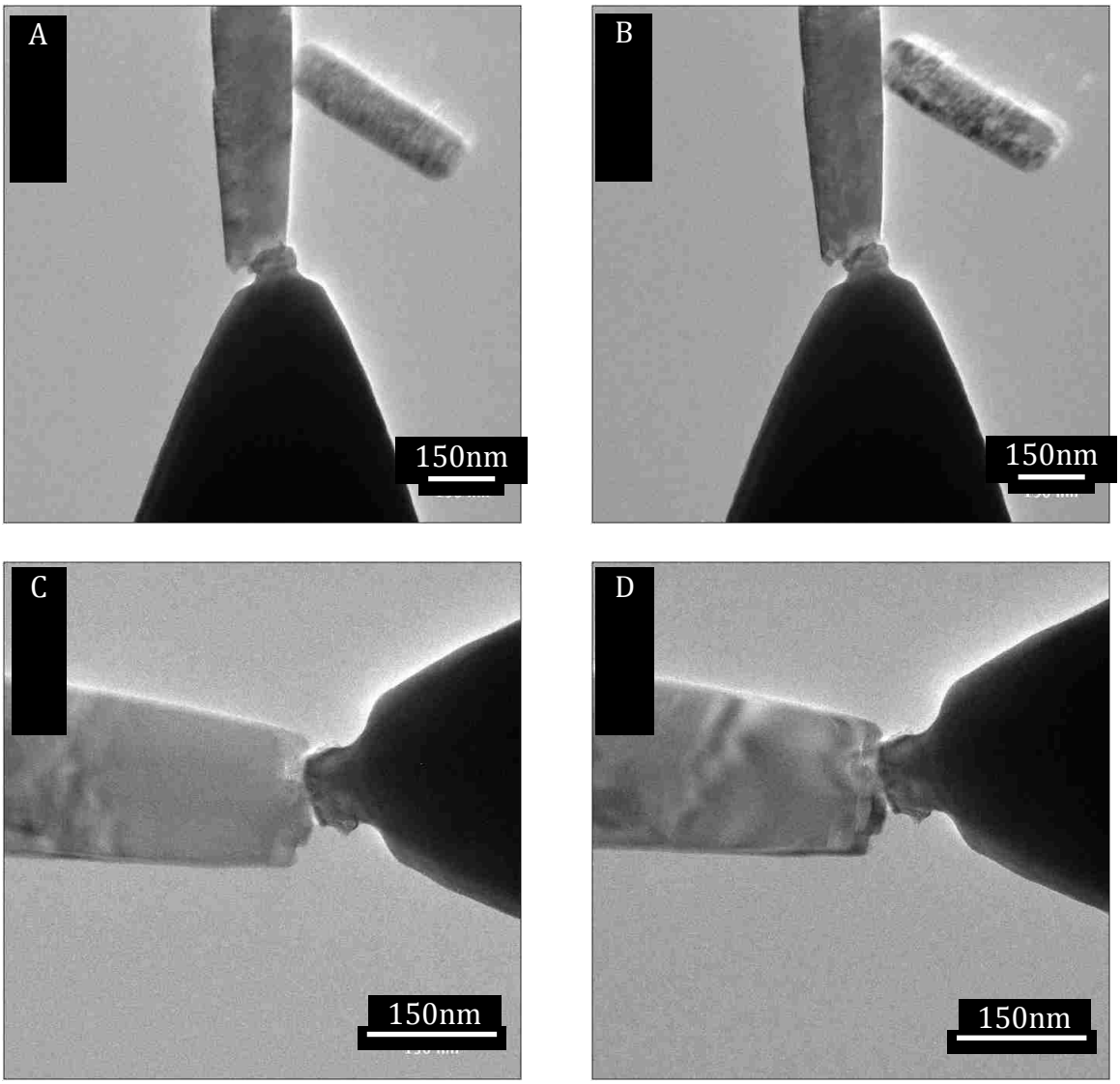

Figure 30: Images of nanoprobe TEM experiment. The left column (A and C) have no voltage applied to the nanowire, and the right column has a 5V bias applied to the nanowire. As it can be seen when comparing A and B as well as comparing C and D there was no distinguishable change in the size of the nanowires as expected when a voltage was applied. There was a distinguishable change in the contrast in the nanowire implying the applied bias was affecting the wire.

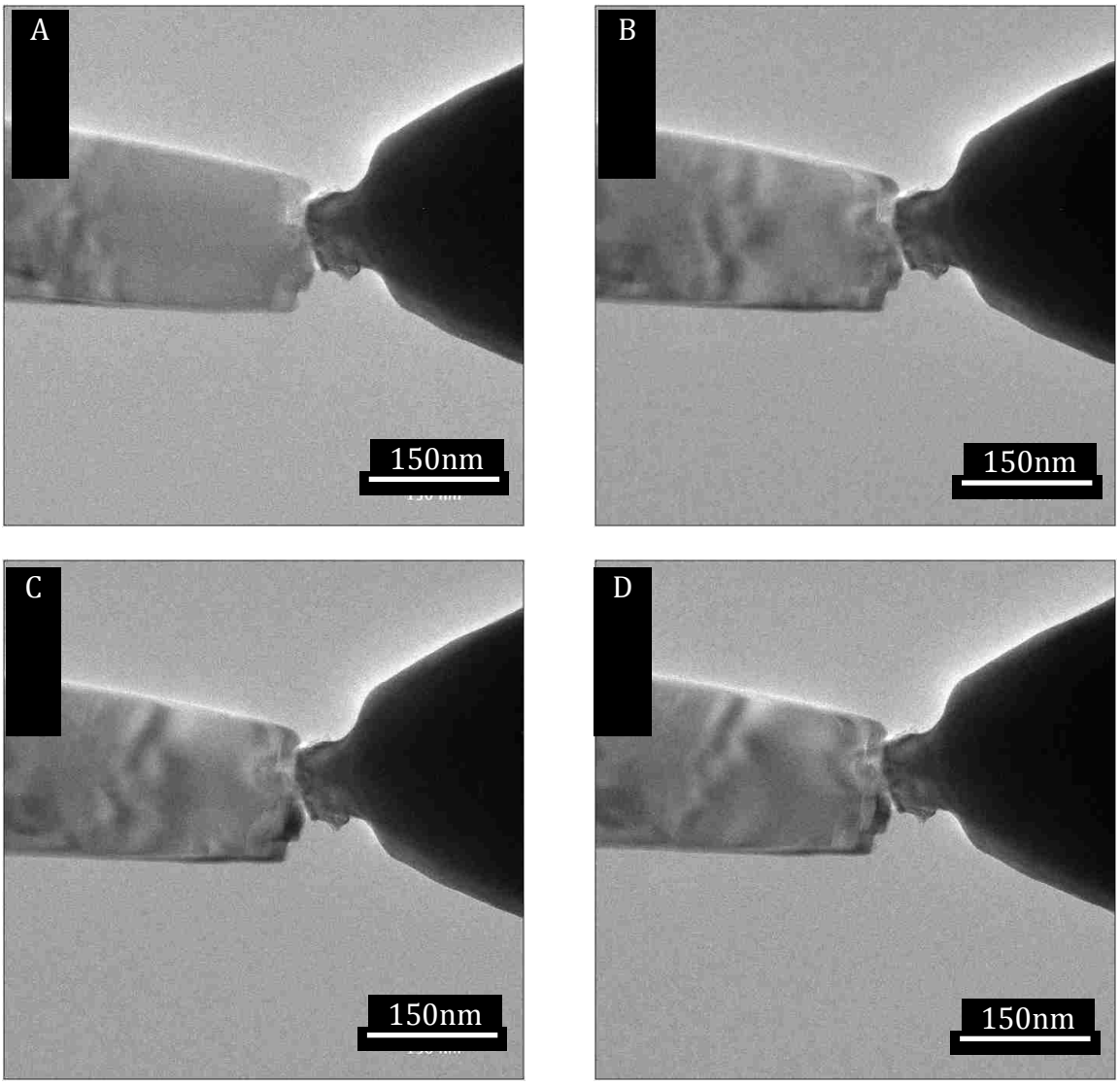

Figure 31: Images of increasing voltages during the nanoprobe experiment. The voltages were increase from 1V to 5V. The voltages corresponding to A, B, C, and D are 0V, 1V, 2.5V, and 5V respectively.

The nanoprobe in situ experiment was never tested on the nanoplatelets due to time and availability of Dr. Jungjohann as well as failing to further test the nanoplatelets. If further characterization of the nanowires and nanoplatelets would ever be sought, this experiment would be a prime candidate to gain a substantial amount of information. This experiment could be used to confirm the thought that the electrical bias further propagated the defects as well as being able to confirm

piezoelectric characteristics of the nanostructures.

DIFFRACTION PATTERN ANALYSIS

By far one of the most useful analysis tools available from the TEM is its ability to image diffraction patterns of the crystal. The interaction with the electron waves with the material being imaged diffracts the electrons, and this diffraction can be imaged by imaging the back focal plane of the image.

Since the nanowires and the nanoplatelets are not always perfect crystals, it was not trivial to obtain a diffraction pattern image for either of the nanowires or the nanoplatelets. Since the most trivial way to obtain an informative diffraction pattern of a crystal is to have the incident electron beam normal to one of the crystal planes, a lot of manipulation of the nanostructure is necessary to obtain a high quality diffraction pattern. Following are several of the obtained diffraction patterns for the non-doped nanowires and non-doped nanoplatelets.

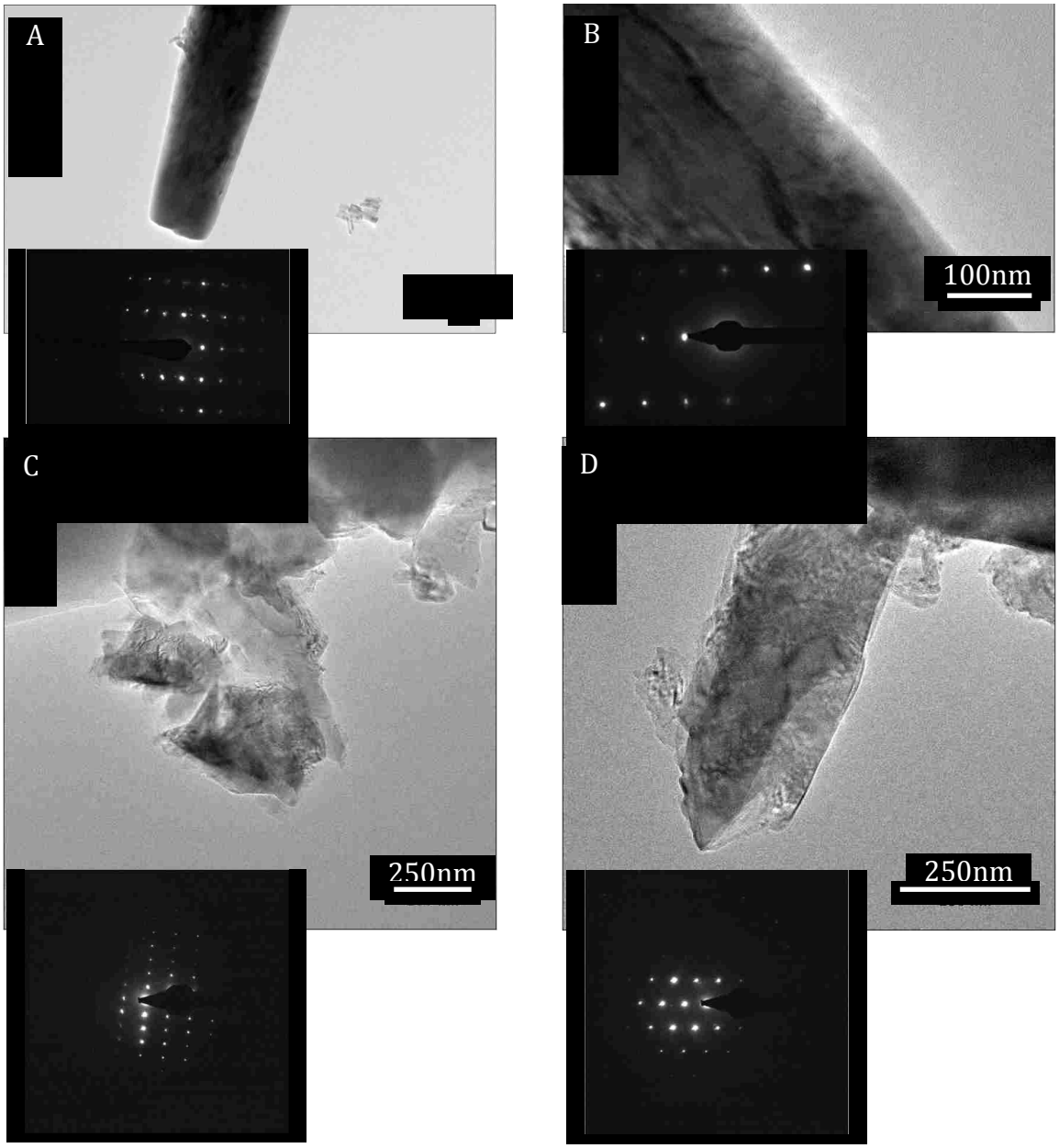

Figure 32. TEM images of the nanowires and nanoplatelets with corresponding diffraction patterns from those samples. Image A is of a non-doped ZnO nanowires, B is of a doped nanowire, and images C and D are of ZnO nanoplatelets.

These diffraction patterns show that the structures have a highly uniform crystalline structure, and when compared to previously published diffraction patterns of ZnO Wurtzite structures, it can be seen that these structures too have a Wurtzite crystal structure.

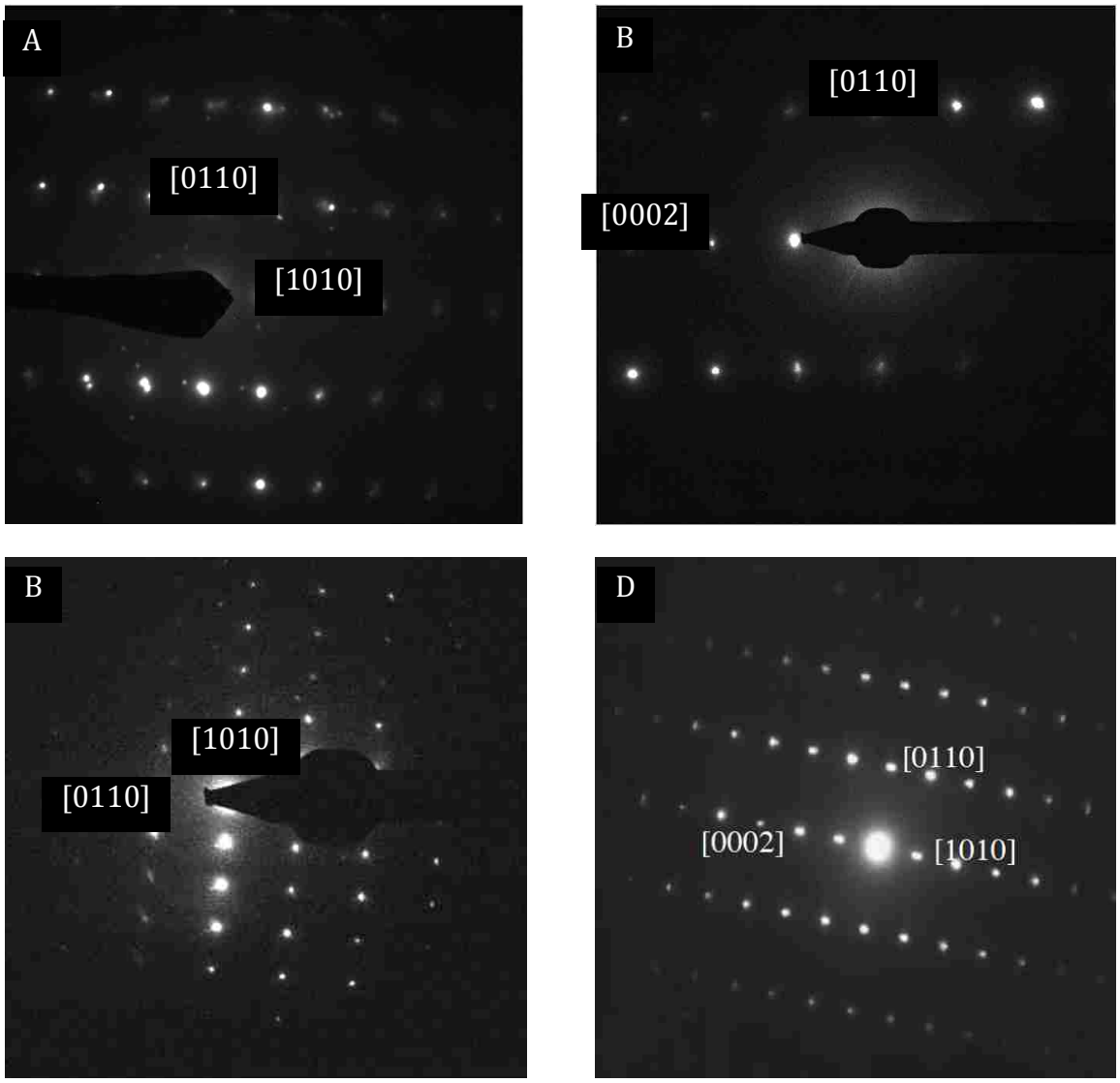

Figure 33: Analysis of gathered diffraction patterns of the ZnO nanostructures. In the above images, A is the diffraction patter obtained from the ZnO nanowire corresponding to Image 22 A, B is of the diffraction patter of the doped ZnO nanowire in Image 22 B, C is the diffraction pattern obtained from the ZnO nanoplatelet corresponding to Image 22 C, andDC is from a known highly crystalline ZnO nanowire grown via MOCVD at a temperature of 600°C [55].

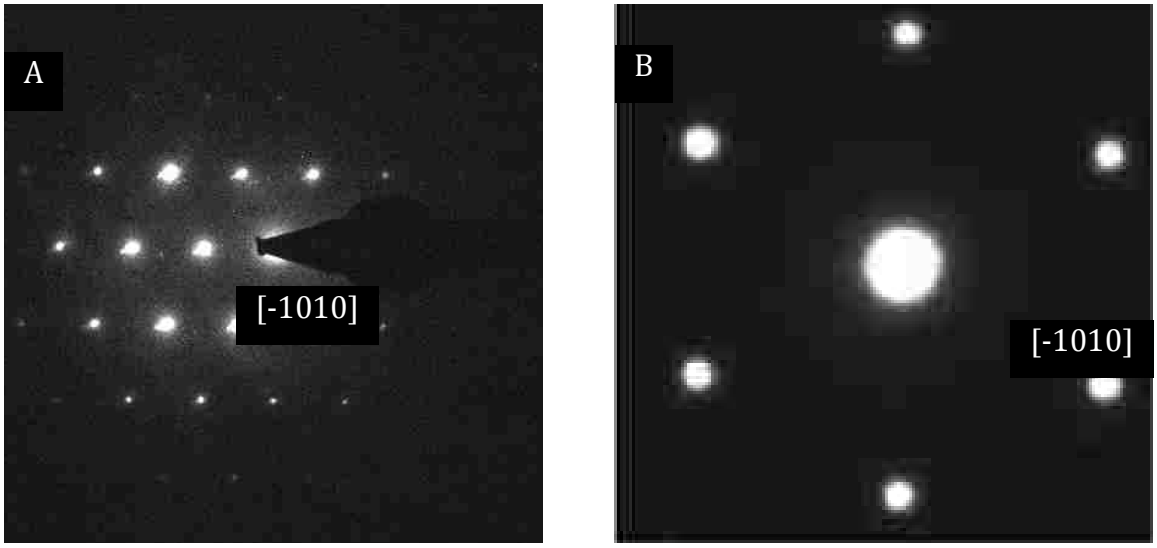

Figure 34: Analysis of gathered diffraction pattern of the ZnO nanoplatelets. In the above images, A is the diffraction pattern obtained from the ZnO nanowires corresponding to D in Image 22 and B is an obtained diffraction pattern from a ZnO nanobelt [56]

Due to the time constraints and attempting to obtain higher quality electrical data, diffraction pattern analysis was not performed on the doped nanoplatelets.

STEM

Scanning Transmission Electron Microscopy (STEM) combines the benefits that are obtained from implementing a scanning technique while retaining its benefits of imaging via transmission. Since a scanning technique is used, the dark field can be obtained while the bright field image is also obtained. Since the microscope is also employing a scanning technique, high contrast between two dissimilar materials. Higher contrast resolution between organic and inorganic materials because of the carbon content of the organic materials.

STEM was primarily employed when the coating of the organic porphyrin onto the inorganic nanowires was being investigated. As it was described in chapter one

and visualized via Figure 1 in chapter one, not only are ZnO nanowires going to be employed in a hybrid organic, inorganic thermoelectric solar cell as the 'hot' top contact, but BiTe nanowires are also going to be used as the 'cold' bottom contact. Therefore it needed to be confirmed that the porphyrin was coating not only the ZnO nanowires, but also the BiTe nanowires. In order to show that the nanowires would work within this thermoelectric cell, the porphyrin needed to coat the nanowires evenly and smoothly. With the following images, it was shown that the porphyrin coat the ZnO and the BiTe nanowires smoothly, and are certainly viable to be used in the thermoelectric device.

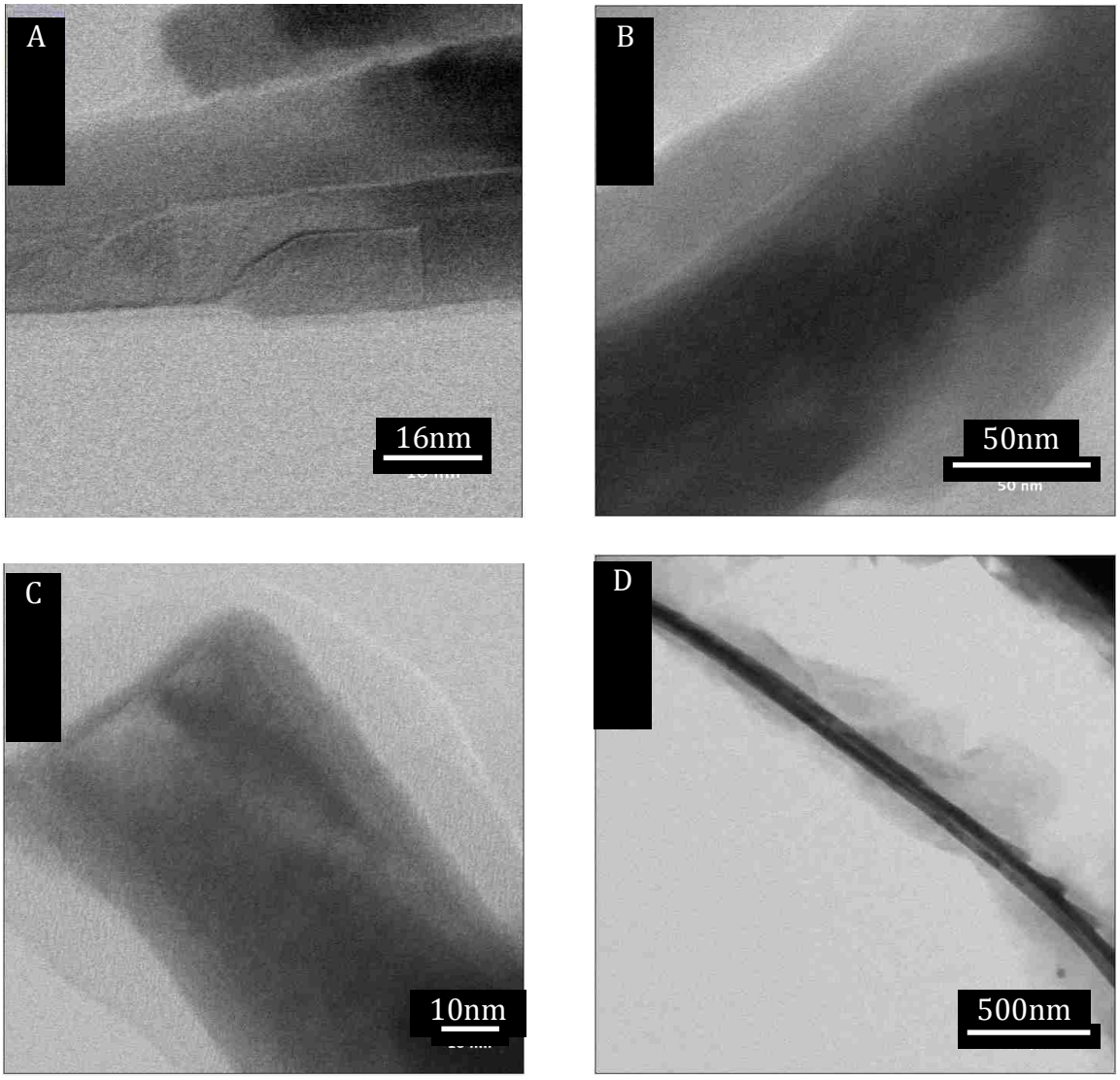

Figure 35. STEM images of porphyrin coated nanowires. Image A shows a ZnO nanowires coated by Sn-Zn porphyrin, B shows another Sn-Zn porphyrin coating a doped ZnO nanowire, C shows a BiTe coated with Sn-Zn porphyrin, and D shows a Zn-Sn porphyrin coated BiTe nanowire.

These images show that the correct porphyrin coatings will coat the nanowires very easily. It was also presented what the the porphyrin looks like when it does not coat the nanowires uniformly. This flaking of the porphyrin shows that the porphyrin structures are not forming in a uniform crystalline structure which will result in poor conduction within the structure due to larger surface areas.

EDS with TEM

It became common practice that when it was discernible to tell what material was being looked at in the TEM, Energy Dispersion X-Ray Spectroscopy (EDS) was used to gain more information on the chemical composition of the material. Since the machinery to make these measurements is very complimentary to TEM and STEM, this was method was employed commonly. Using the EDS equipment on the TEM, the nanoplatelets were confirmed to be ZnO, the porphyrin coatings were confirmed to being comprised of what they were expected to be comprised of, and confirmation of dopant was confirmed in the doped nanowires.

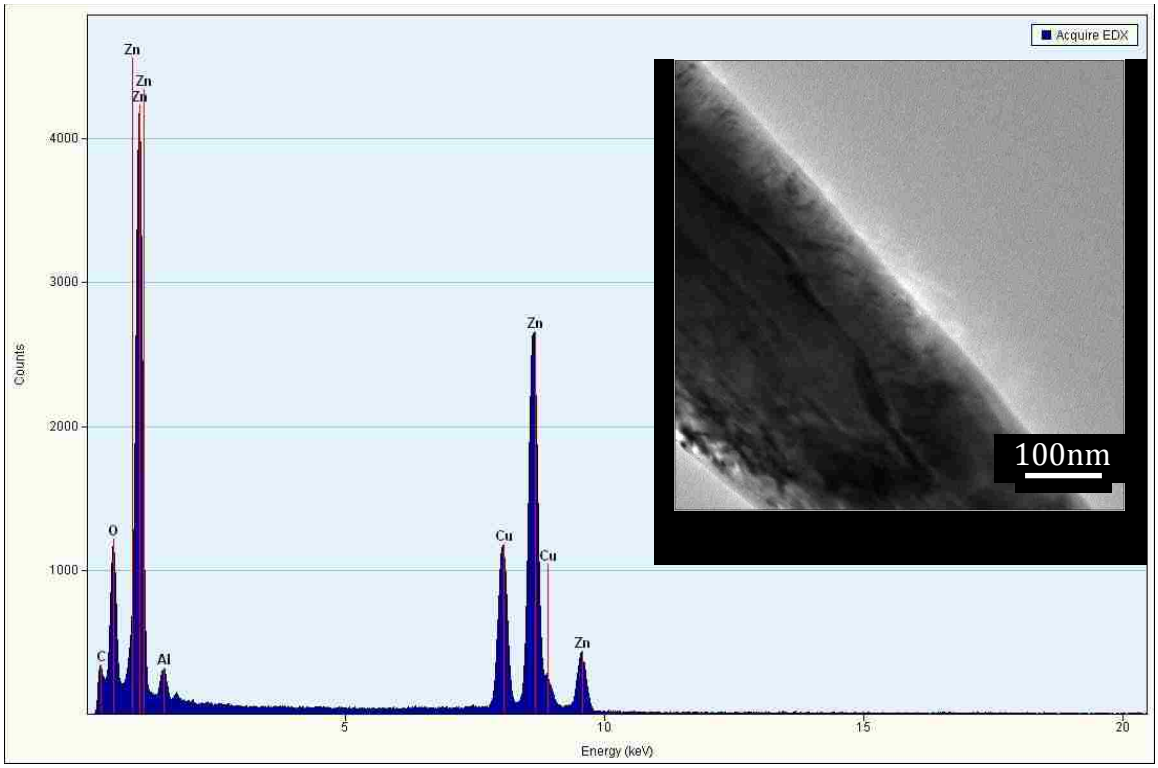

Figure 36: EDS of doped ZnO nanowire and corresponding TEM image.

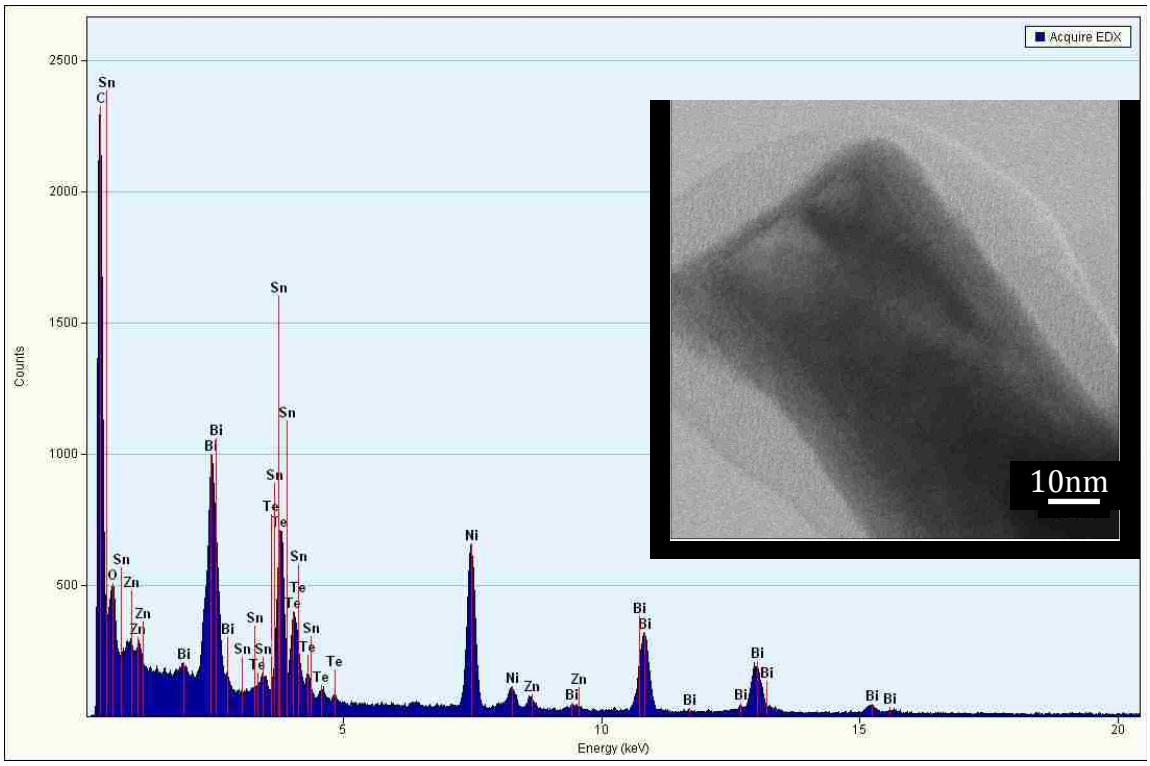

Figure 37: EDS of porphyrin coated BiTe nanowire.

These EDS findings were used to help support the conclusions of what was being expected. Using this the conclusion of using the Sn-Zn porphyrin layering processes would uniformly coat the ZnO nanowires as well as the BiTe nanowires. It was also shown that the Aluminum was being incorporated into the doped ZnO nanowires. Further study would need to be taken to determine the exact stoichiometric make up of the doped ZnO nanowires.

XRD

X-Ray Diffraction (XRD) analysis resulted in some conflicting data for the nanowires and nanoplatelets. The data clearly shows that there was a peak in the nanoplatelets when there was not in the nanowires. Due to the peaks received through the system, most of the peaks with the ZnO nanowires are hidden in the noise of the system. Even though it was further explored, it was never discovered

what the anomaly of the ZnO nanoplatelet peak corresponded to.

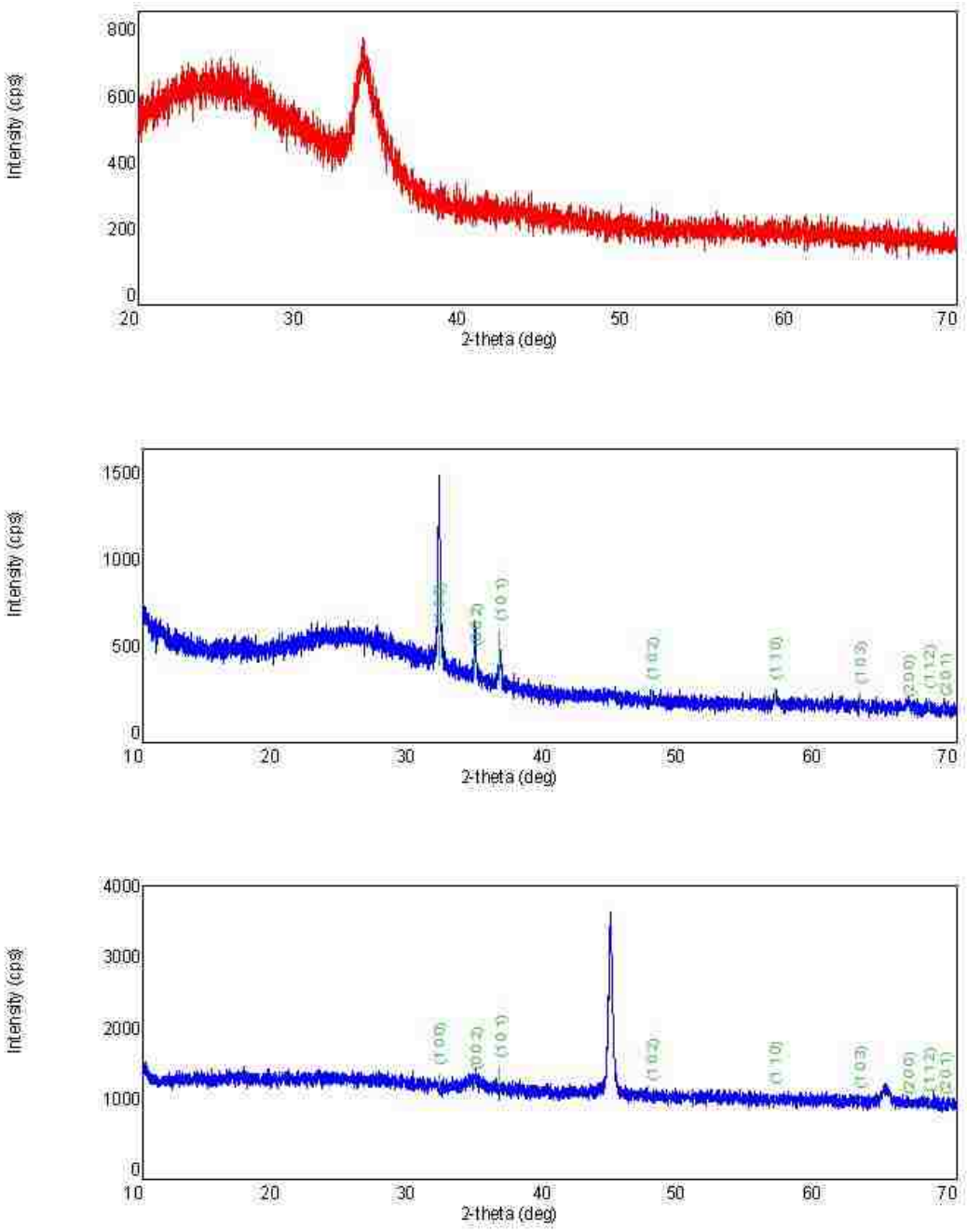

Figure 38: The above XRD data in order from top to bottom is from the grown Al doped ZnO thin film, ZnO nanowire, and ZnO nanoplatelets

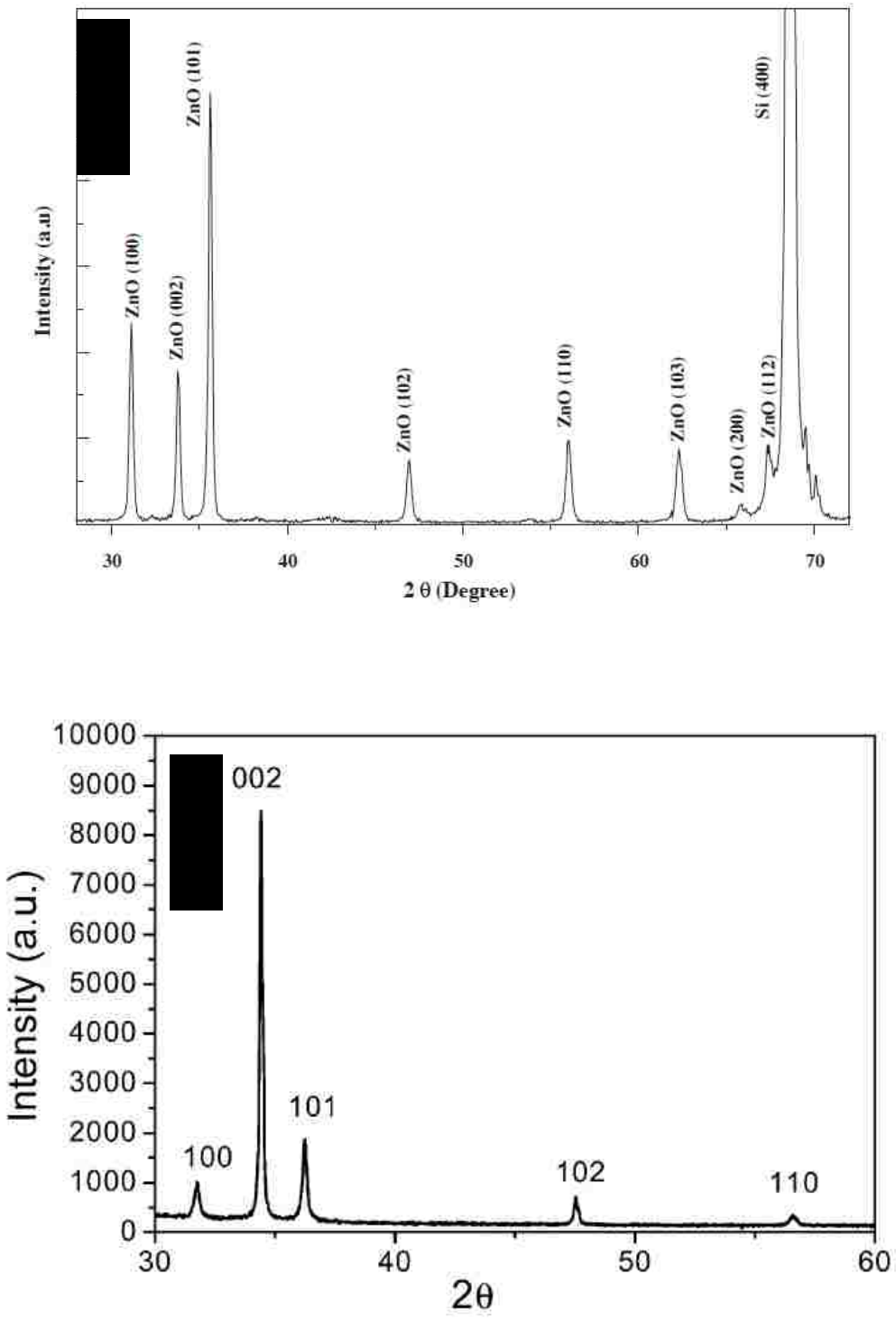

Figure 39: Acquired XRD from known ZnO nanostructures. A is an acquired XRD data from MOCVD grown ZnO nanowires [55] and B is an acquired XRD from solution growth ZnO nanoplatelets [38] .

Once the TEM diffraction pattern analysis and the EDS confirmed that the

nanoplatelets were ZnO Wurtzite crystalline stuctures, it was not further explored. This was decided since the main focus of the research was to gain more information on the ZnO nanowires. For future testing, the highly dense interwoven nanoplatelets could be tested to confirm that these highly dense structures eliminate the anomaly.

UV-VIS

Since the ZnO nanowires are being developed to be used as a top contact that will be covering the entirety of a solar device, they need to be highly, if not fully transparent to the light frequencies that the device will be using as its main source of electron hole pair generation in the active region. Since the porphyrin is photosensitive in the visible, the ZnO nanowires need to be highly, or fully transparent in the visible region of light. It is also important to have the ZnO nanowires be transparent in the infrared region so the device can absorb the infrared energy for heat absorption. The photospectrometer was able to accurately measure this characteristic of the nanowires.

Initially when measuring the transmissivity of the nanowires, the readings were not consistent and the machine was getting peaks above 100% transmissivity in regions that the machine is rated accurate. This is an impossible reading and the data was obviously not coinciding with the manufacture's claims of accuracy due to the fact if the machine was not acquiring correct information within its stated range of operation. To combat this, a different approach to collect the data was attempted. Originally, it was instructed to run the machine and calibrate the machine to a common substrate for the testing samples. Therefore it was instructed to calibrate the machine to subtract the glass sample from the collected data. This created

inconsistent and incorrect data since there were consistently values of over 100% transmissivity which is not possible since that would suggest light would need to be created from within the sample. It was considered that the machines internal optics were not correctly configured, or that the machine was making an incorrect calculation, but from the operator's manual and talking with the technician, this seemed highly improbable, therefore another approach was taken.

The second approach was to confirm that the machine and software was correctly taking the systems noise and responsively into account. Therefore instead of having the machine subtract a common sample, a test was ran to subtract all noise from the system initially. This was done by having the system run without any sample in it what so ever, and to subtract any signal it receives from this ideally zero signal. When this was done all of the sample readings become much smother and consistent. This also eliminated the anomalies of over 100% transmissivity. The signal from the glass was then later subtracted from each of the signals individually to correct the readings to only account for the seeding layer and the nanowires. This was easily done by measuring the glass, and using the value collected as the 'noise' introduced by the glass substrate.

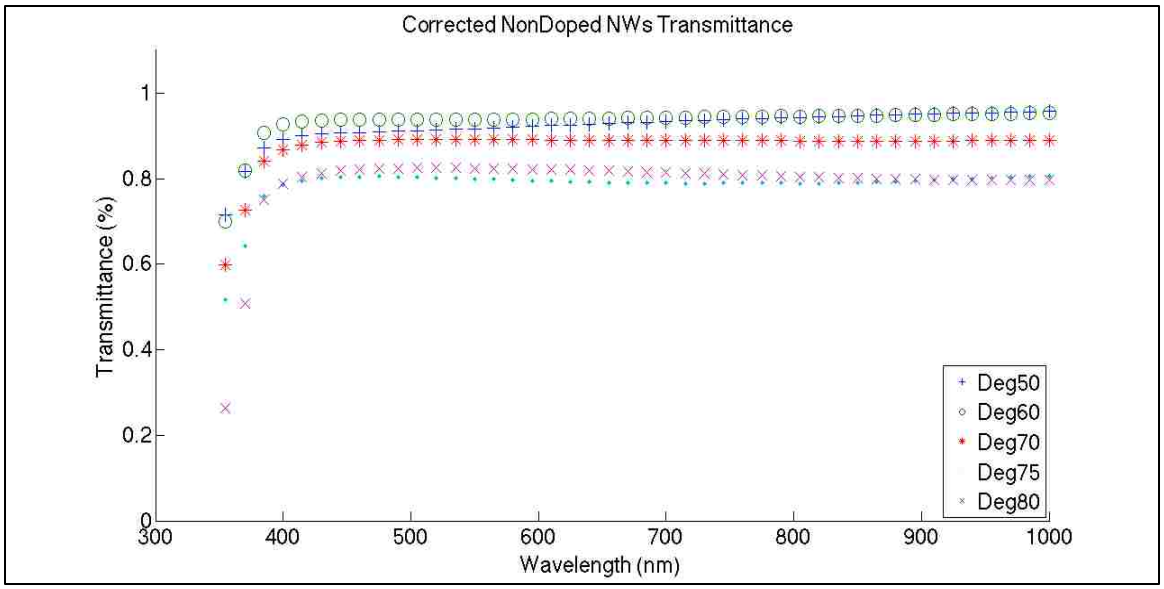

Figure 40: Corrected transmissivity of non-doped ZnO nanowires.

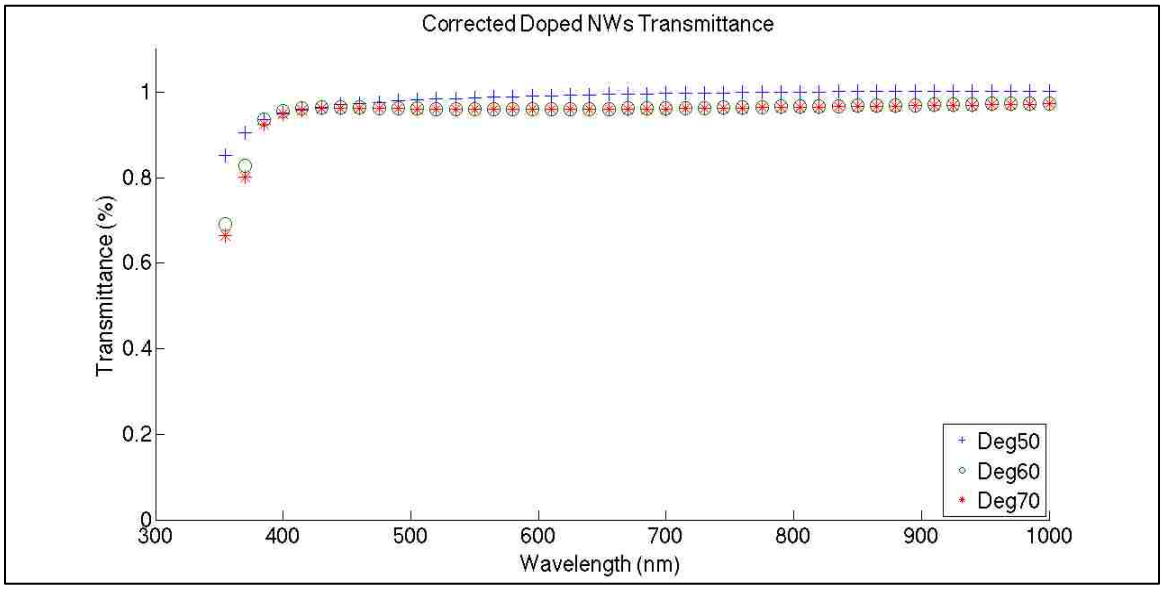

Figure 41: Corrected transmissivity of doped ZnO nanowires.

As it can be seen, data was collected for the doped and non-doped nanowires. There was an anomaly observed when looking at the transmittance data of the doped nanowires in that it was expected that the transmissivity of the doped nanowires would be the same as the non-doped nanowires. This was expected since doped nanowires are largely the same material as the non doped nanowires.

The increase in transmissivity of the doped nanowires is being suggested as being an affect of the doped nanowire bed not being as uniform as the non-doped nanowire bed with a combination of the average length of the doped nanowires being less than the non-doped nanowires. With the combination of these two factors, the transmissivity of the doped nanowires would be expected to increase since there is less material present than the non-doped nanowires.

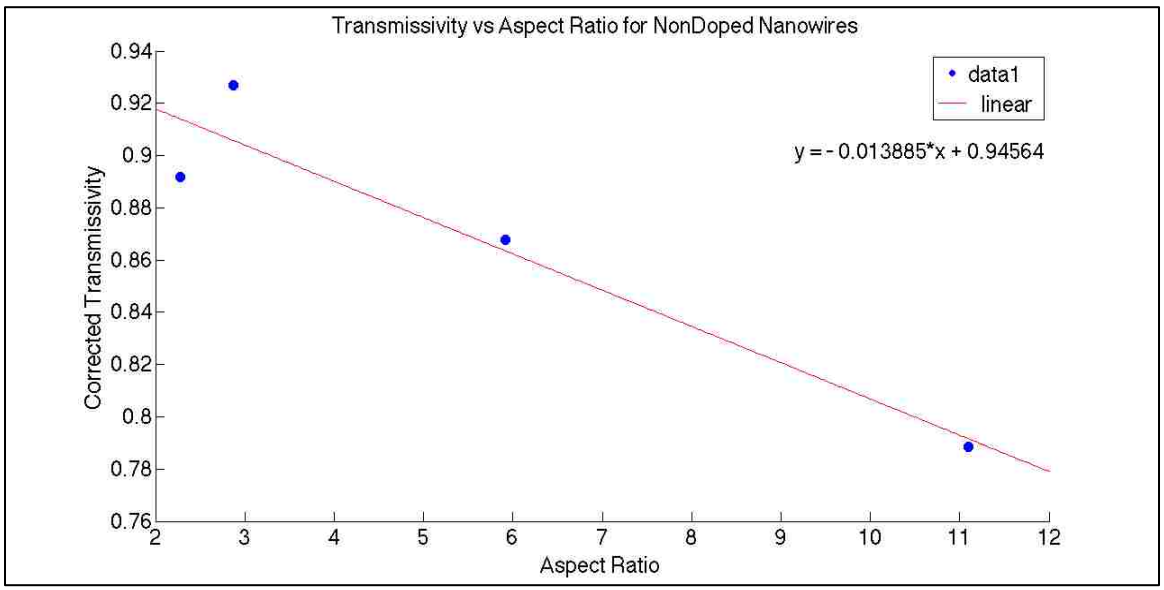

Figure 42: Transmissivity vs aspect ratio plot to show of nondoped nanowires.

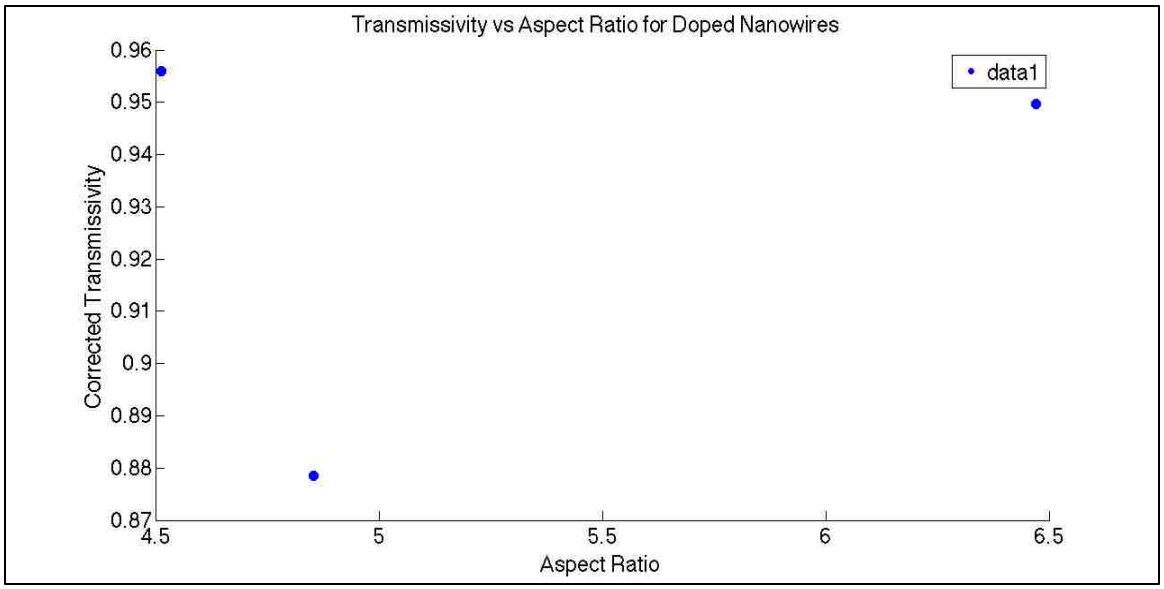

Figure 43: Transmissivity vs aspect ratio plot to show of nondoped nanowires.

Figures 42 and 43 show the dependence in the nanowire transmissivity to the aspect ratio, which can be viewed as the dependence of the transmissivity to the length. There is a clear linear decrease in the transmissivity as the length increased for the doped nanowires, but due to the limited data points, the doped nanowires data set is inconclusive.

CAFM

The Conductive Atomic Force Microscope was used due to its simplicity to acquire data, and time effectiveness. Another technique used to try and gain conductivity data for a single nanowires was to measure the conductivity with a nanoprobe set up with a TEM, SEM, or other specialize optics. The problem with these other set ups is the time to set up these experiments and learn the set up since in any of these nanoprobe set ups, specialized tools and skills were needed. In the case of the TEM nanoprobe, Dr. Jungjojann would needed to have been involved

with the experiment, and for the other specialized set up, a single nanowire would have to be mounted onto a conductive stage manually and then measured. This is extremely time intensive, and nearly impossible to collect a nanowire that made up the bed of nanowires directly attached to the seeding layer due to the small size high probability of the nanowires 'sticking' to each other due to atomic and electrical forces. The nanowire that would have been used would've had to be a nanowire that grew within the solution and deposited on the surface of the bed of nanowires. This is very problematic because these nanowires are considered defects and have a high probability of not being characteristic to the other nanowires since they did not grow on the seeding layer and tend to have more defects than the nanowires directly grown from the seeding layer. Even though it seems like the CAFM is an obvious solution to not having to use a nanoprobe set up, it came with its own challenges.

Originally when the CAFM was being used, it was not realized that the CAFM was not correctly calibrated. This meant that the data initially collected was incorrect and had to be recollected. Once the system was correctly calibrated by the CAFM technician at CINT, the data could be trusted.

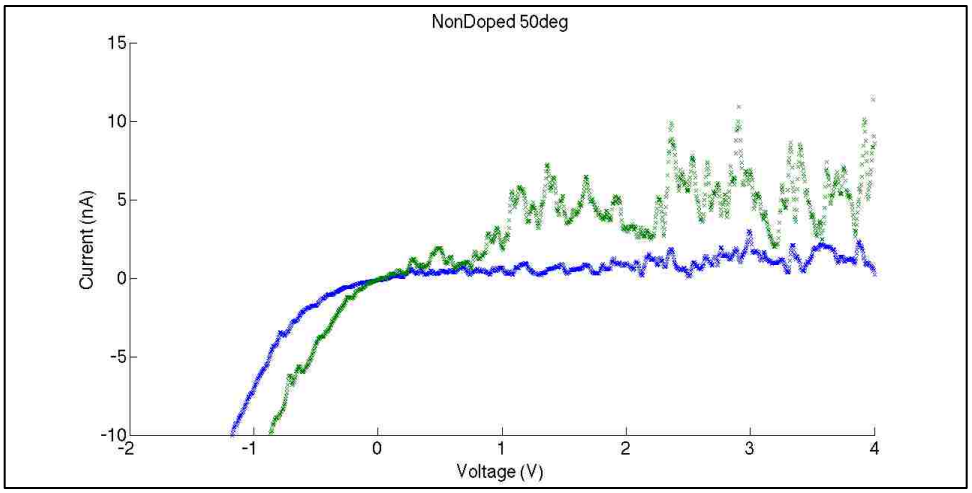

Figure 44: Conductivity data collected for nondoped ZnO nanowire grown within solution at 50°C. Each curve was a separate location and voltage sweep.

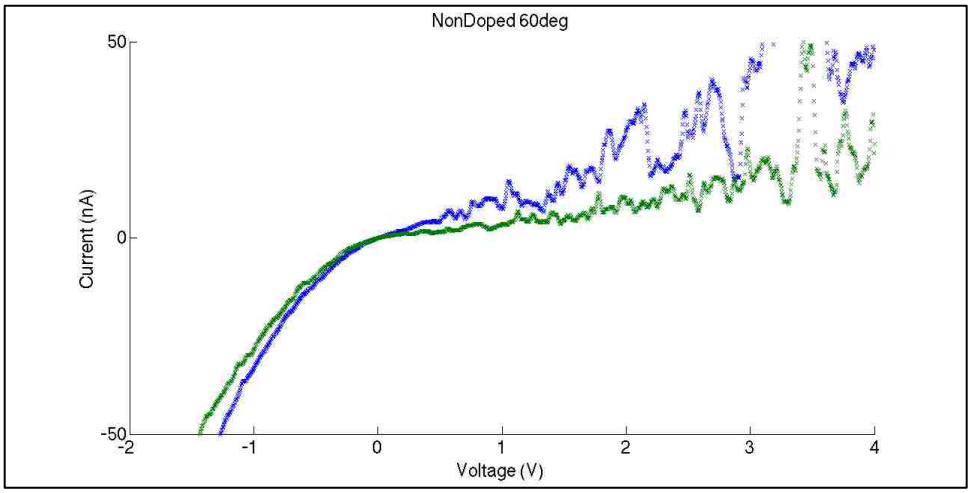

Figure 45: Conductivity data collected for nondoped ZnO nanowire grown within solution at 60°C. Each curve was a separate location and voltage sweep.

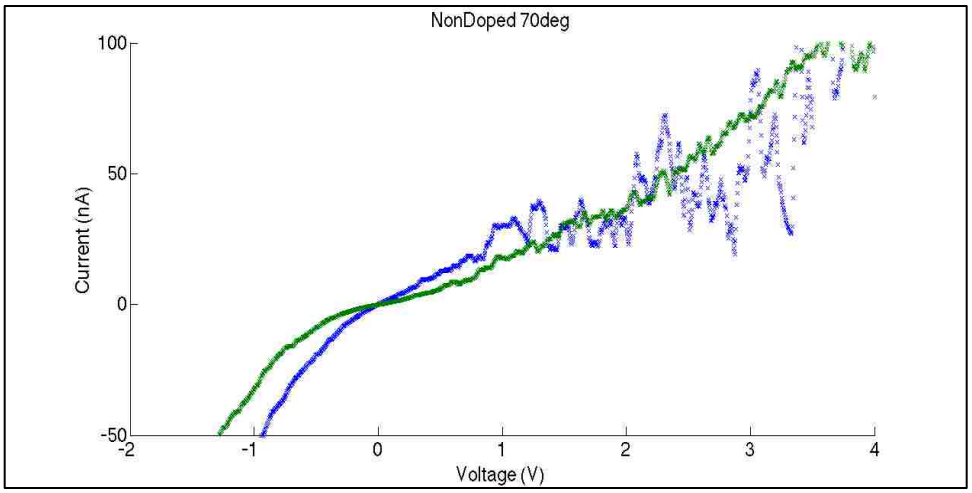

Figure 46: Conductivity data collected for nondoped ZnO nanowire grown within solution at 70°C. Each curve was a separate location and voltage sweep.

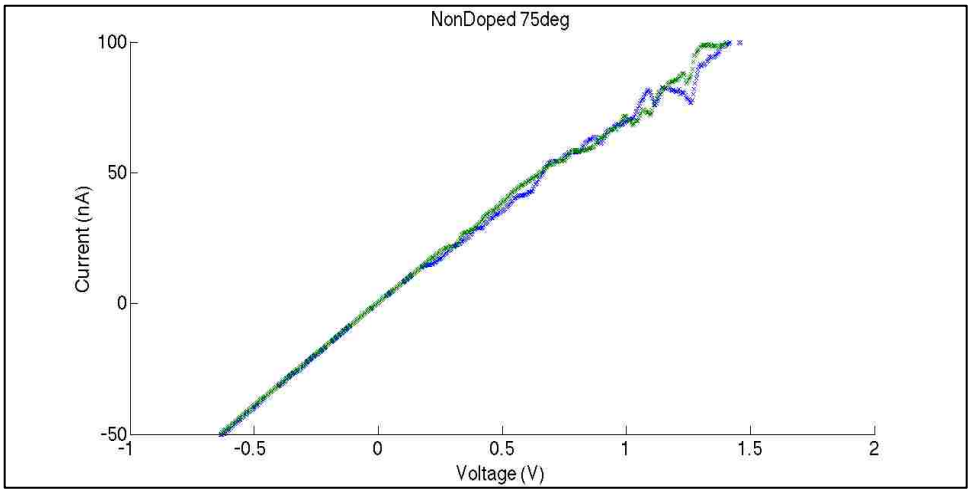

Figure 47: Conductivity data collected for nondoped ZnO nanowire grown within solution at 75°C. Each curve was a separate location and voltage sweep.

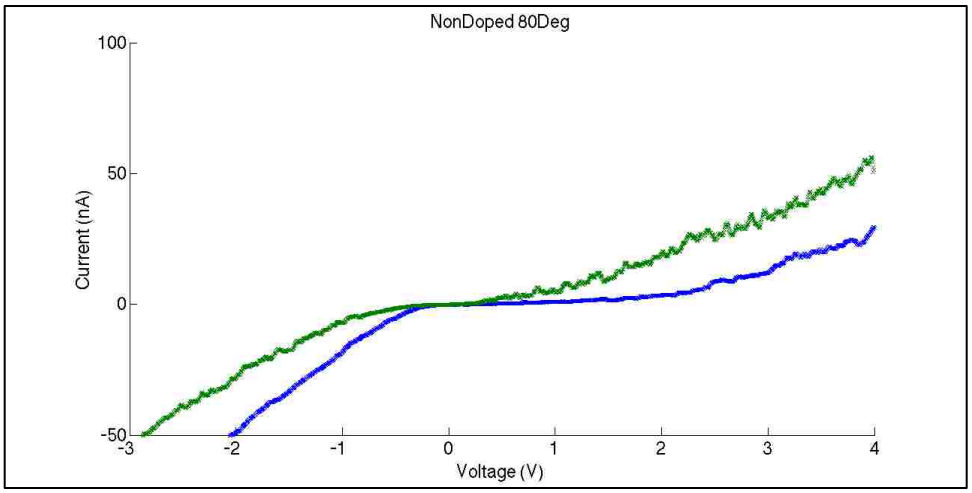

Figure 48: Conductivity data collected for nondoped ZnO nanowire grown within solution at 80°C. Each curve was a separate location and voltage sweep.

Following are the conductivity data sets for the doped nanowires.

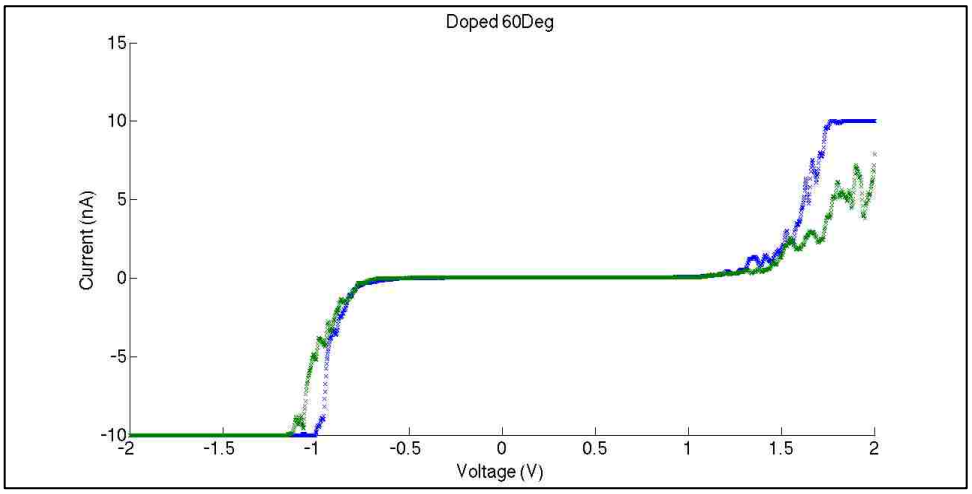

Figure 49: Conductivity data collected for doped ZnO nanowire grown within solution at 60°C. Each curve was a separate location and voltage sweep.

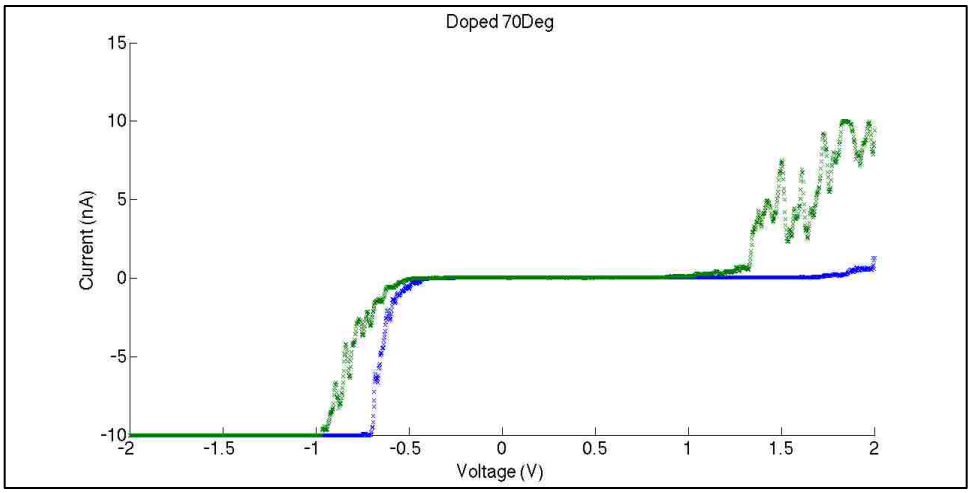

Figure 50: Conductivity data collected for doped ZnO nanowire grown within solution at 70°C. Each curve was a separate location and voltage sweep.

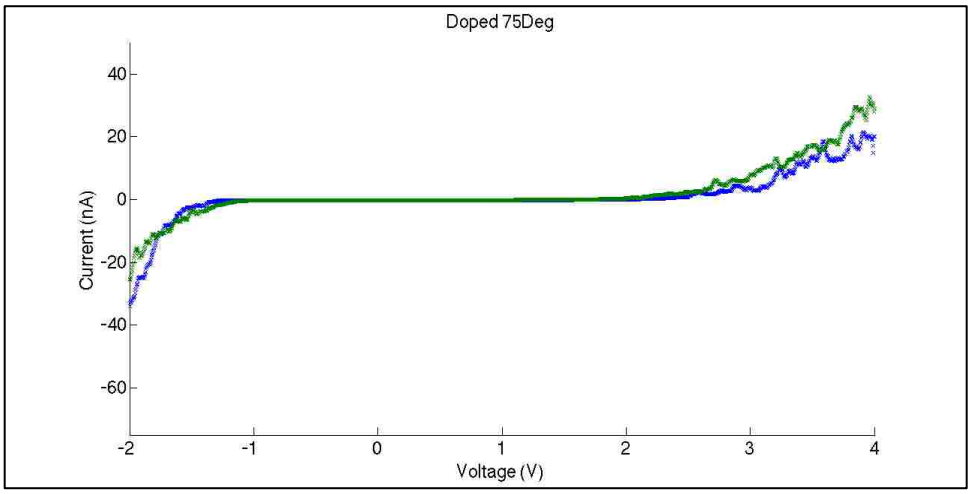

Figure 51: Conductivity data collected for doped ZnO nanowire grown within solution at 75°C. Each curve was a separate location and voltage sweep.

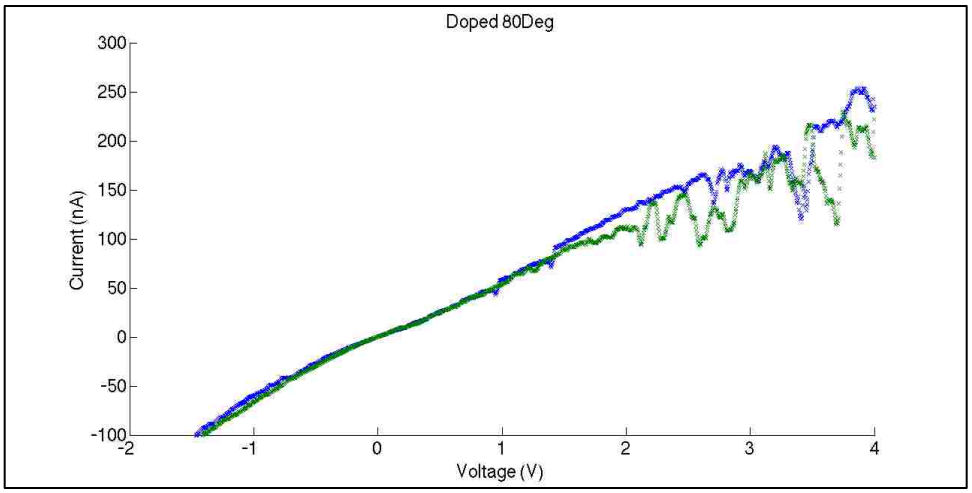

Figure 52: Conductivity data collected for doped ZnO nanowire grown within solution at 80°C. Each curve was a separate location and voltage sweep.

As it can be seen even though the data is accurate, the conductivity is not necessarily good for either the doped and non-doped nanowires. This was unfortunate since a large amount of time was used debating the collected data and it validity. With extra time to further test the doping concentrations and how it was implemented, there is a high likelihood that the conductivity can be increased.

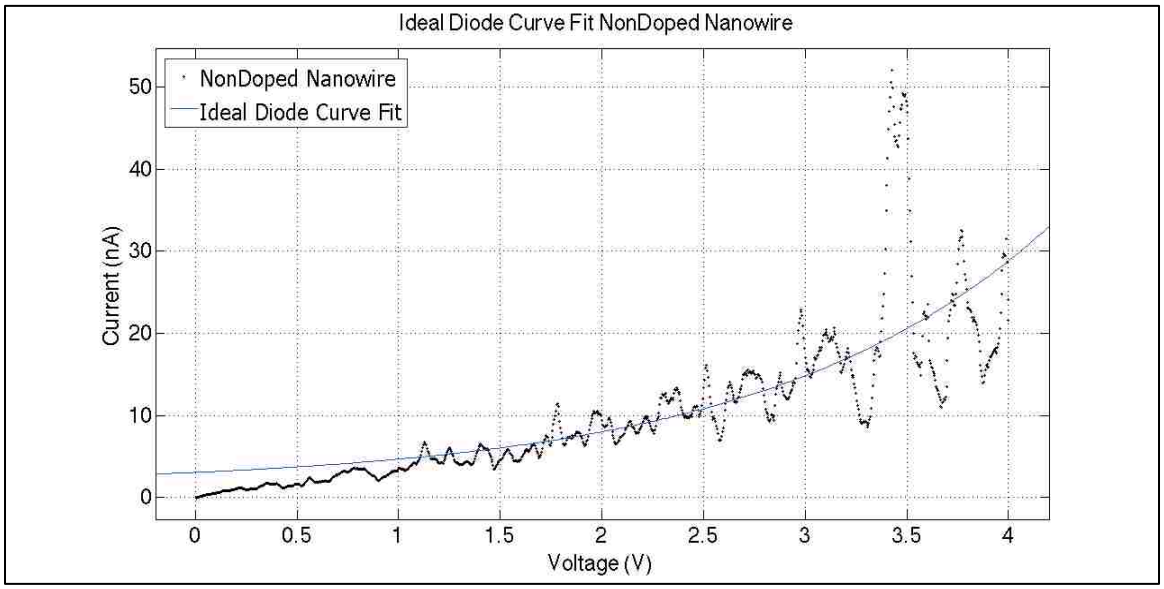

Figure 53: Curve fit of Ideal Diode equation for nondoped nanowires grown 60° C.

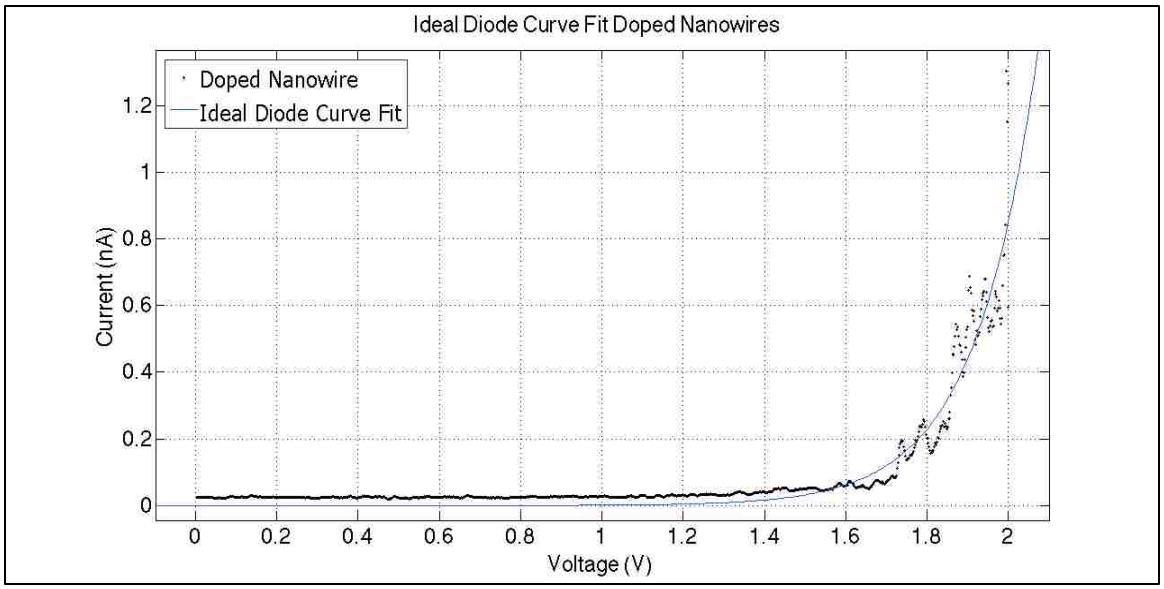

Figure 54: Curve fit of Ideal Diode equation for doped nanowires grown at 70° C.

Using the Ideal Diode equation as [57]

$$I = I_s\left(\exp\left(\frac{eV}{nkT}\right) - 1\right)$$

with I_s being the ideal reverse-bias saturation current, e being the elementary charge of an electron, V being the applied voltage, n as the diode factor that is ideally between 1 and 2, k being Boltzmann's constant, and T being the temperature during the test in Kelvin. Using room temperature as T it was found that the I_s for the nondoped nanowires was $8.76nA$ and I_s for the doped nanowires was $1.727x10^{-6}nA$. It was also found that n for the nondoped nanowire was over 1000 and for the doped nanowire was 5.89. Both values are unrealizable in the ideal diode equation implying there is more than basic recombination factors causing the nanowires to perform poorly. It was calculated that the conductivity of the doped nanowires grown at 70 degrees was $8.848x10^{-2}\,\frac{S}{m}$. Since the data for the nondoped nanowires was not as good as the conductivity data for the doped nanowires no

further steps were taken to calculate the conductivity

Conductivity data was also collected for the non-doped and doped nanoplatelets. This data was also unfortunate in that it showed little conductivity in the nanoplatelets. Since the nanoplatelet growth itself can be improved, the wisest action would be to improve the conductivity of the nanowires first, and attempt to implement the knowledge gained in that study and implement that for the nanoplatelets.

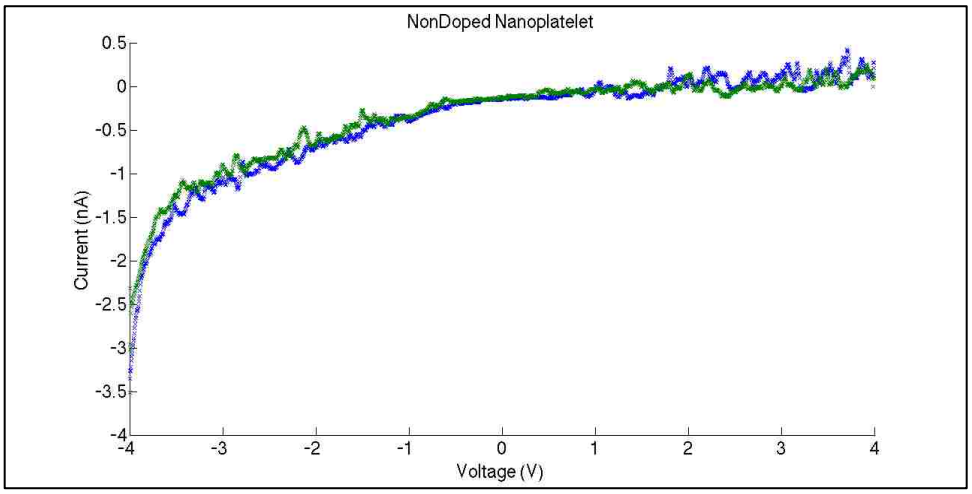

Figure 55: Conductivity data collected for nondoped ZnO nanoplatelet grown in the pseudo vapor. The blue and green curves represent a forward and reverse voltage sweep at the same location taken by the machine.

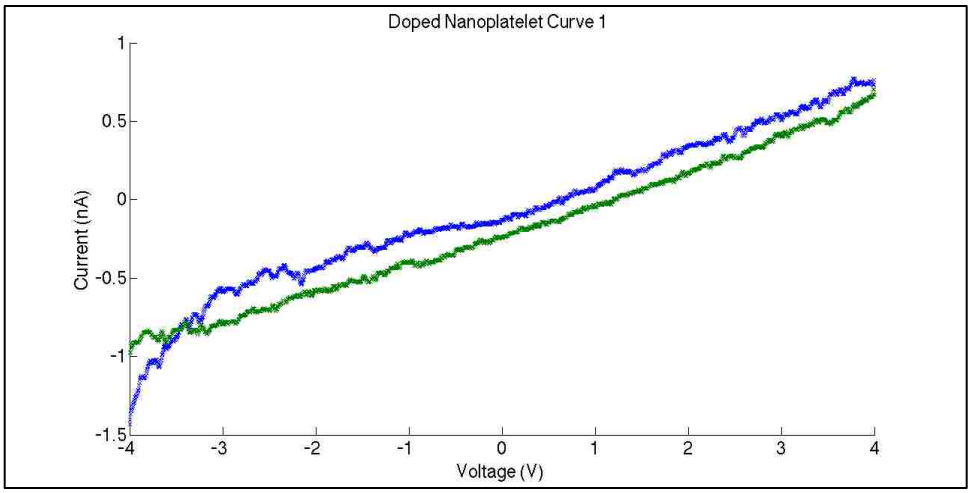

Figure 56: Conductivity data collected for doped ZnO nanoplatelet grown via the pseudo vapor method. The blue and green curves represent two separate curve traces at location, curve two in Figure 60.

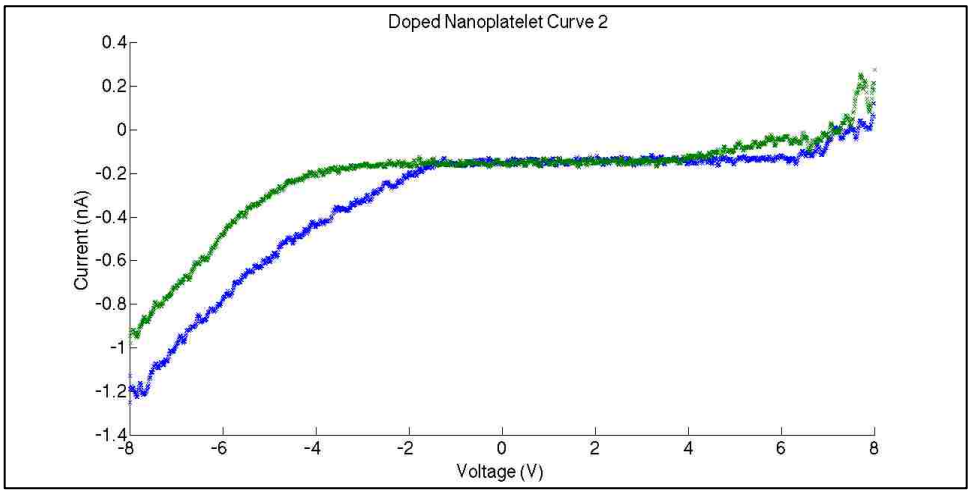

Figure 57: Conductivity data collected for doped ZnO nanoplatelet grown via the pseudo vapor method. The blue and green curves represent two separate curve traces at location curve two in Figure 58.

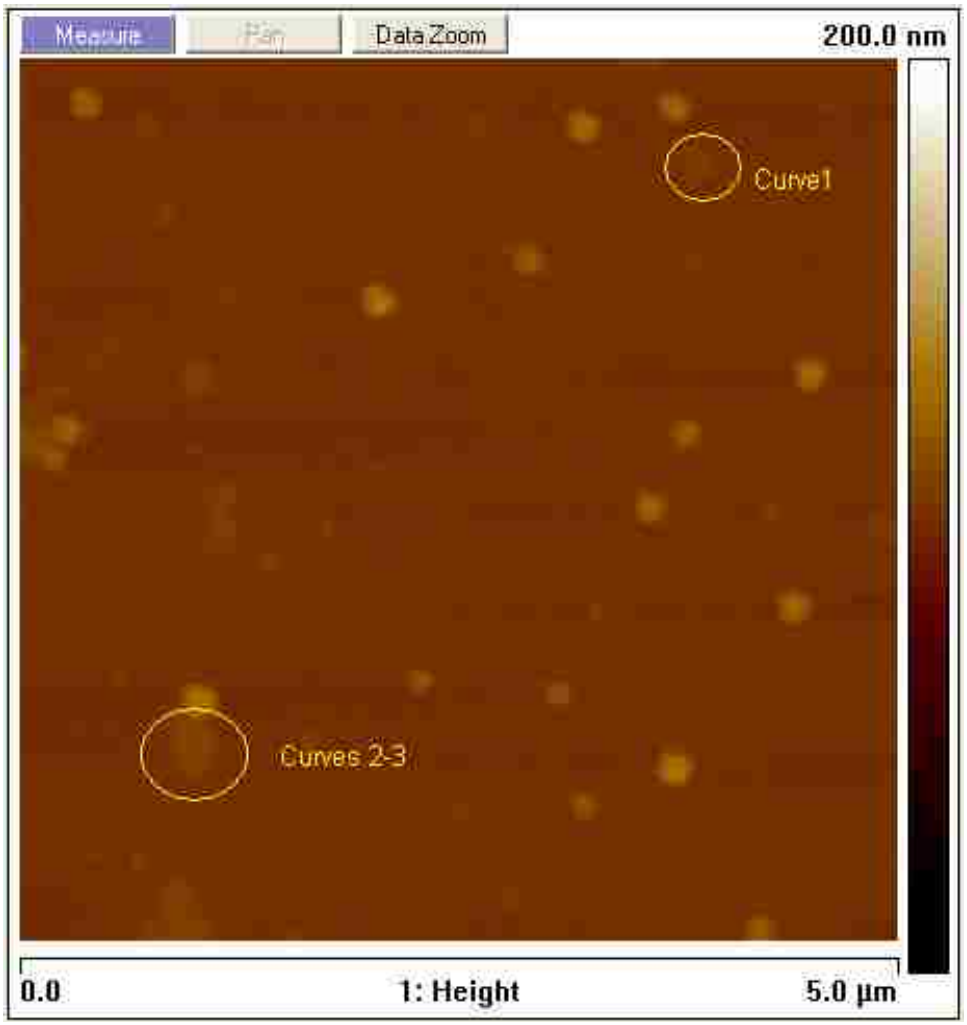

Figure 58: Nondoped nanoplatelet CAFM image collected during the collection of the conductivity data.

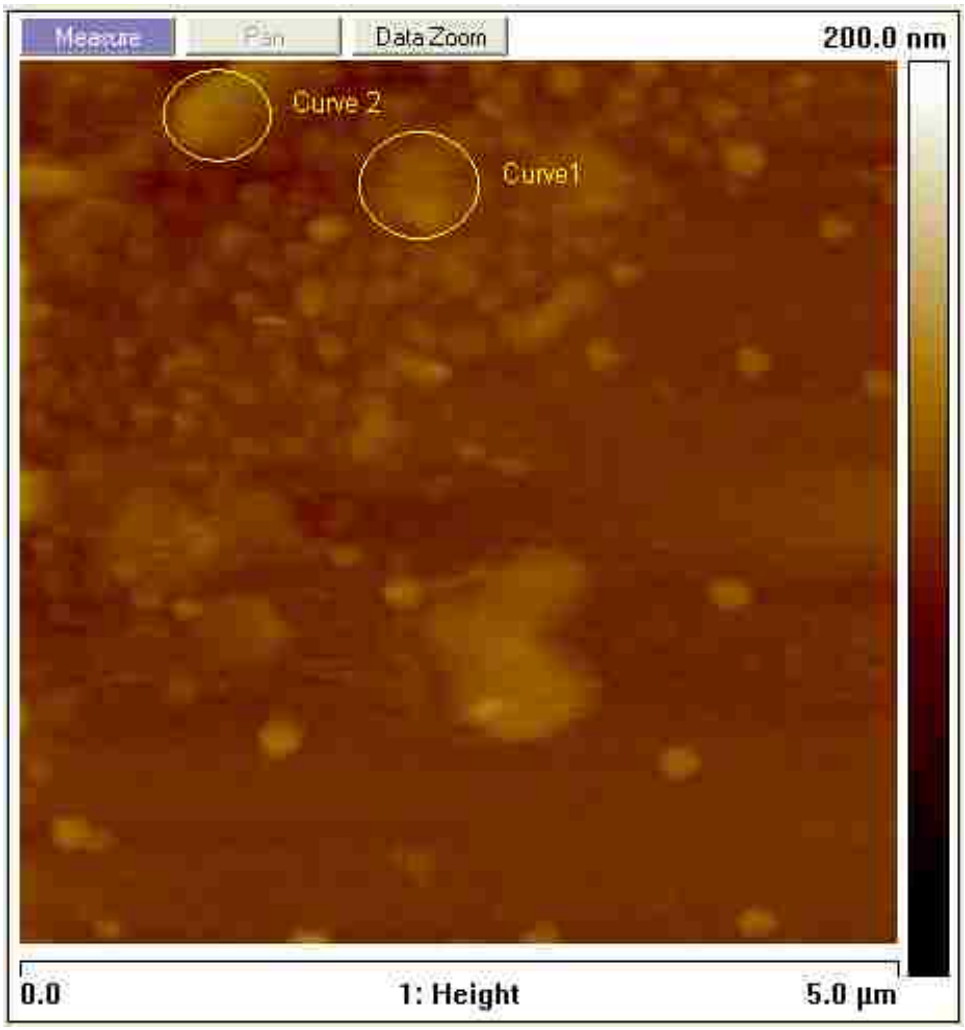

Figure 59: Doped nanoplatelet CAFM image collected during the collection of the conductivity data.

There was some indication that the doped nanoplatelets were showing slight conductivity, but due no further actions were taken since the data was showing the performance was still very poor.

Conclusion

ZnO nanowires show promising data to be further developed as a top contact for a hybrid organin-inorganic thermoelectric solar cell. There was clear uniform growth of the nanowires confirmed with imaging by SEM as well as having high crystalline structure confirmed through TEM diffraction pattern analysis. It was shown that the transmissivity of the nanowire beds higher than 80% for the most favorable growth outcomes when tested in the visable and near ultraviolet region. Conductivity data showed the nanowires are slightly conductive, but there still needs to be testing and optimaiztion performed to increase the conductivity of nanowires. This can be done by further testing the growth conditions of the nanowires while introducing Aluminum dopants during growth.

It was shown that another crystal structure can be grown instead of the nanowires when the reactants and temperature of the growth is lowered enough. By limiting the reactants and lowering the temperature of the growth solution, nanoplatelets, a two dimensional structure is grown instead of the one dimensional nanowire growth observed with a higher solution temperature and reactant concentration. This nanoplatelet structure showed a Wurtzite crystalline structure. This was. It was shown that the nanoplatelets do follow the same trend with increased conductivity with an introduction of aluminum as a dopant, but further testing will need to be done to obtain favorable results to implement the structure into any electrical or optoelectrical structure.

REFERENCES

1. Grätzel, Michael. "Dye-sensitized solar cells." *Journal of Photochemistry and Photobiology C: Photochemistry Reviews* 4.2 (2003): 145-153.
2. Martin, Kathleen et al. "Bio-hybrid integrated system for wide-spectrum solar energy harvesting." *SPIE OPTO* 7 Mar. 2014: 89831D-89831D-6.
3. Erdman, Matt et al. "New generation of biomorph integrated with TCO and thermoelectric to enhance efficiency in wide solar spectrum solar cell." *Photovoltaic Specialist Conference (PVSC), 2014 IEEE 40th* 8 Jun. 2014: 1762-1765.
4. Kim, Jin Young et al. "Efficient tandem polymer solar cells fabricated by all-solution processing." *Science* 317.5835 (2007): 222-225.
5. Tritt, Terry M, and MA Subramanian. "Thermoelectric materials, phenomena, and applications: a bird's eye view." *MRS bulletin* 31.03 (2006): 188-198.
6. Suh, D-I et al. "The fabrication and characterization of dye-sensitized solar cells with a branched structure of ZnO nanowires." *Chemical physics letters* 442.4 (2007): 348-353.
7. Subbaiyan, Navaneetha K, and Francis D'Souza. "Light-to-electron converting panchromatic supramolecular solar cells of phthalocyanine–porphyrin heterodimers adsorbed onto nanocrystalline SnO 2 electrodes." *Chemical Communications* 48.30 (2012): 3641-3643.

8. Martin, Kathleen E et al. "Donor– Acceptor Biomorphs from the Ionic Self-Assembly of Porphyrins." *Journal of the American Chemical Society* 132.23 (2010):8194-8201.

9. Medforth, Craig John et al. "Self-assembled porphyrin nanostructures." *Chemical Communications* 47 (2009): 7261-7277.

10. Reynolds, DC et al. "Valence-band ordering in ZnO." *Physical review B* 60.4 (1999): 2340.

11. Özgür, Ü et al. "A comprehensive review of ZnO materials and devices." *Journal of applied physics* 98.4 (2005): 041301.

12. Tian, Yongming et al. "Morphological families of self-assembled porphyrin structures and their photosensitization of hydrogen generation." *Chemical Communications* 47.21 (2011): 6069-6071.

13. Norton, David P et al. "ZnO: growth, doping & processing." *Materials today* 7.6 (2004): 34-40.

14. Wang, ZL. "Novel nanostructures of ZnO for nanoscale photonics, optoelectronics, piezoelectricity, and sensing." *Applied Physics A* 88.1 (2007): 7-15.

15. Musat, Viorica et al. "Multifunctional zinc oxide nanostructures for a new generation of devices." *Materials Chemistry and Physics* 132.2 (2012): 339-346.

16. Nakada, T.; Hirabayashi, Y.; Tokado, T.; Ohmori, D.; Mise, T.Novel device structure for Cu(In,Ga)Se-2 thin film solar cells using transparent conducting oxide back and front contacts, Sol Energy 2004, 77, (6), 739-747

17. Lee, Woong, Min-Chang Jeong, and Jae-Min Myoung. "Catalyst-free growth of ZnO nanowires by metal-organic chemical vapour deposition (MOCVD) and thermal evaporation." *Acta Materialia* 52.13 (2004): 3949-3957.

18. Wagh, M. S.; Patil, L. A.; Seth, T.; Amalnerkar, D. P.Surface cupricated SnO2-ZnO thick films as a H2S gas sensor, Mater Chem Phys 2004, 84, (2-3), 228-233.

19. Ushio, Y.; Miyayama, M.; Yanagida, H.Effects of Interface States on Gas-Sensing Properties of a Cuo/Zno Thin-Film Heterojunction, Sensor Actuat B-Chem 1994, 17, (3), 221-226.

20. Hasuike, N.; Fukumura, H.; Harima, H.; Kisoda, K.; Matsui, H.; Saeki, H.; Tabata, H.Raman scattering studies on ZnO doped with Ga and N (codoping), and magnetic impurities, J Phys-Condens Mat 2004, 16, (48),

21. Heo, Y. W.; Ivill, M. P.; Ip, K.; Norton, D. P.; Pearton, S. J.; Kelly, J. G.; Rairigh, R.; Hebard, A. F.; Steiner, T.Effects of high-dose Mn implantation into ZnO grown on sapphire, Appl Phys Lett 2004, 84, (13), 2292-2294.

22. Nishii, J.; Hossain, F. M.; Takagi, S.; Aita, T.; Saikusa, K.; Ohmaki, Y.; Ohkubo, I.; Kishimoto, S.; Ohtomo, A.; Fukumura, T.; Matsukura, F.; Ohno, Y.; Koinuma, H.; Ohno, H.; Kawasaki, M.High mobility thin film transistors with transparent ZnO channels, Jpn J Appl Phys 2 2003, 42, (4A), L347-L349.

23. Hossain, F. M.; Nishii, J.; Takagi, S.; Ohtomo, A.; Fukumura, T.; Fujioka, H.; Ohno, H.; Koinuma, H.; Kawasaki, M.Modeling and simulation of polycrystalline ZnO thin-film transistors, Journal of Applied Physics 2003, 94, (12), 7768-7777.

24. Norris, B. J.; Anderson, J.; Wager, J. F.; Keszler, D. A.Spin-coated zinc oxide transparent transistors, J Phys D Appl Phys 2003, 36, (20), L105-L107.

25. Ye, Changhui et al. "Zinc oxide nanostructures: morphology derivation and evolution." *The Journal of Physical Chemistry B* 109.42 (2005): 19758-19765.

26. Vayssieres, Lionel. "Growth of arrayed nanorods and nanowires of ZnO from aqueous solutions." *Advanced Materials* 15.5 (2003): 464-466.

27. Xu, Sheng, and Zhong Lin Wang. "One-dimensional ZnO nanostructures: solution growth and functional properties." *Nano Research* 4.11 (2011): 1013-1098.

28. Greene, Lori E et al. "Low-temperature wafer-scale production of ZnO nanowire arrays." *Angewandte Chemie International Edition* 42.26 (2003): 3031-3034.

29. Wang, Huihu, Changsheng Xie, and Dawen Zeng. "Controlled growth of ZnO by adding H 2 O." *Journal of crystal growth* 277.1 (2005): 372-377.

30. Willander, M.; Nur, O.; Zhao, Q. X.; Yang, L. L.; Lorenz, M.; Cao, B. Q.; Perez, J. Z.; Czekalla, C.; Zimmermann, G.; Grundmann, M.; Bakin, A.; Behrends, A.; Al-Suleiman, M.; El-Shaer, A.; Mofor, A. C.; Postels, B.; Waag, A.; Boukos, N.; Travlos, A.; Kwack, H. S.; Guinard, J.; Dang, D. L.Zinc oxide nanorod based photonic devices: recent progress in growth, light emitting diodes and lasers, Nanotechnology 2009, 20, (33).

31. Liu, Bin, and Hua Chun Zeng. "Hydrothermal synthesis of ZnO nanorods in the diameter regime of 50 nm." *Journal of the American Chemical Society* 125.15 (2003): 4430-4431.

32.García, Concepción Mejía et al. "Synthesis of Aluminum-doped Zinc Oxide Nanowires hydrothermally grown on plastic substrate." *Advances in Materials Physics and Chemistry* 2.04 (2013): 56.

33. Hsu, Cheng-Liang et al. "Well-Aligned, Vertically Al-Doped ZnO Nanowires Synthesized on ZnO: Ga/Glass Templates." *Journal of The Electrochemical Society* 152.5 (2005): G378-G381.

34. Wan, Qing et al. "Fabrication and ethanol sensing characteristics of ZnO nanowire gas sensors." *Applied Physics Letters* 84.18 (2004): 3654-3656.

35. Wang, JX et al. "Hydrothermally grown oriented ZnO nanorod arrays for gas sensing applications." *Nanotechnology* 17.19 (2006): 4995.

36. Mahmoud, Waleed E. "Synthesis and optical properties of Ce-doped ZnO hexagonal nanoplatelets." *Journal of Crystal Growth* 312.21 (2010): 3075-3079.

37. Hong, Jung-Il et al. "Magnetism in dopant-free ZnO nanoplates." *Nano letters* 12.2 (2012): 576-581.

38. Ye, Changhui et al. "Thickness-dependent photocatalytic performance of ZnO nanoplatelets." *The Journal of Physical Chemistry B* 110.31 (2006): 15146-15151.

39. He, Shan et al. "Enhancement of visible light photocatalysis by grafting ZnO nanoplatelets with exposed (0001) facets onto a hierarchical substrate." *Chem. Commun.* 47.38 (2011): 10797-10799.

40. Li, Zhengwei, and Wei Gao. "ZnO thin films with DC and RF reactive sputtering." *Materials Letters* 58.7 (2004): 1363-1370.

41. Fu, En-Gang et al. "Properties of transparent conductive ZnO: Al thin films prepared by magnetron sputtering." *Microelectronics Journal* 35.4 (2004): 383-387.

42. Jin, Z-C, I Hamberg, and CG Granqvist. "Optical properties of sputter-deposited ZnO: Al thin films." *Journal of applied physics* 64.10 (1988): 5117-5131.

43. Flickyngerova, S et al. "Structural and optical properties of sputtered ZnO thin films." *Applied Surface Science* 254.12 (2008): 3643-3647.

44. Chen, M et al. "X-ray photoelectron spectroscopy and auger electron spectroscopy studies of Al-doped ZnO films." *Applied Surface Science* 158.1 (2000): 134-140.

45. Martin Schmidt, Susan Ruff, and Robert O'Handley. *6.152J Micro/Nano Processing Technology, Fall 2005*. (Massachusetts Institute of Technology: MIT OpenCourseWare), http://ocw.mit.edu (Accessed 26 Mar, 2015). License: Creative Commons BY-NC-SA

46. Mook, WT et al. "Removal of total ammonia nitrogen (TAN), nitrate and total organic carbon (TOC) from aquaculture wastewater using electrochemical technology: A review." *Desalination* 285 (2012): 1-13.

47. Ding, Yong. "Fundamental Theory of Transmission Electronic Microscopy." Fundamental Theory of Transmission Electronic Microscopy. N.p., n.d. Web. 8 Jan. 2015. <http://www.nanoscience.gatech.edu/zlwang/research/tem.html>.

48. Jiang, Ying-Bing. "ELECTRON/ATOM INTERACTION & DIFFRACTION FROM A CRYSTAL." University of New Mexico. Apr. 2014. Lecture.

49. "Electron Beam/Specimen Interactions." Materials Science and Engineering. Iowa State University of Science and Technology, 2015. Web. 1 Mar. 2015. <http://www.mse.iastate.edu/research/laboratories/sem/microscopy/how-does-the-sem-work/college-electron-microscope/beam-interactions/>.

50. Hitzman, Chuck. "Auger Electron Spectroscopy." *Auger Electron Spectroscopy*. Stanford, n.d. Web. 2 Mar. 2015. <http://web.stanford.edu/group/snl/auger.html>.

51. Goodge, John. "Energy-dispersive Detector (EDS)." Geochemical Instrumentation and Analysis. Carleton College, 2014. Web. 27 Mar. 2015. <http://serc.carleton.edu/research_education/geochemsheets/eds.html>.

52. "Bragg Law, Crystals." Encyclopedia Britannica Online. Encyclopedia Britannica, 2015. Web. 1 Mar. 2015. <http://www.britannica.com/EBchecked/topic/76973/Bragg-law>.

53. Bragg Law. Digital image. Britannica. Britannica, 1998. Web. Feb. 2015. <http://www.britannica.com/EBchecked/topic/76973/Bragg-law>.

54. Mai, Wenjie. "Fundamental Theory of Atomic Force Microscopy." Fundamental Theory of Atomic Force Microscopy. N.p., n.d. Web. 27 Mar. 2015. <http://www.nanoscience.gatech.edu/zlwang/research/afm.html>.

55. Sekar, A et al. "Catalyst-free synthesis of ZnO nanowires on Si by oxidation of Zn powders." *Journal of Crystal Growth* 277.1 (2005): 471-478.

56. Wang 2, Zhong Lin. "ZnO nanowire and nanobelt platform for nanotechnology." *Materials Science and Engineering: R: Reports* 64.3 (2009): 33-71.

57. Neamen, Donald A. "8.3.2." Semiconductor Physics and Devices: Basic Principles. 3rd ed. Boston: McGraw-Hill, 2003. 303-04. Print.